Department of Precision and Microsystems Engineering

On-Chip Optothermal Actuation of an hBN Membrane for Photonic Optomechanical Sensing

Rayan ElFawal

Report no : 2026.062
Coach : Mohammadjavad Ebrahimpour
Professor : Dr. Gerard Verbiest
Specialisation : High Tech Engineering
Type of report : Master Thesis Project Report
Date : August 19, 2026
Student number : 6257836



Abstract

This thesis investigates the feasibility of on-chip optothermal actuation of a suspended hexagonal boron nitride (hBN) membrane integrated with a silicon photonic ring resonator operating near 1550 nm. A partially transferred multilayer graphene flake is used as the absorbing transducer. The same continuous-wave laser is intensity-modulated to generate a periodic thermal load while simultaneously providing cavity-enhanced optical readout of membrane motion.

Theoretical modelling of the graphene/hBN heterostructure predicts bimorph deflections in the range of 0.1–20 nm under idealised assumptions. Experimentally, coherent spectral features are observed when the laser intensity is modulated at frequencies between 12 and 30 MHz. The coherent response exhibits a clear maximum near 14 MHz, coinciding with the independently measured thermomechanical resonance of the membrane. The frequency-dependent coherent response, together with its enhancement near the mechanical resonance, provides evidence of optothermally driven mechanical motion of the membrane.

As an additional quantitative analysis, the measured coherent response is converted to an estimated driven displacement using the optical transduction range established on hBN thickness range. This gives a displacement on the order of a few picometres. The estimate is affected by uncertainties in the transduction calibration and by device-specific factors such as partial graphene–hBN contact, residual membrane tension, and thermal low-pass filtering.

The results demonstrate the feasibility of electrode-free optothermal actuation of an hBN membrane within an integrated silicon photonic platform. The observed resonance-centred coherent response establishes the primary proof of concept, while the quantitative displacement estimate provides a basis for identifying the parameters that should be improved in future device designs.

Acknowledgements

I would like to express my sincere gratitude to everyone who supported me during this Master thesis project.

First and foremost, I thank my supervisor, Prof. Dr. Gerard Verbiest, for his guidance, insightful feedback, and continuous support throughout the project. I am especially grateful to my daily supervisor, Mohammadjavad Ebrahimpour, whose dedication, experimental expertise, and constant availability were invaluable. His support in the laboratory and his constructive advice played a central role in the successful completion of this work.

I also wish to thank my family for their unwavering support. I am deeply grateful to my husband for his patience, understanding, and practical support throughout this demanding period, particularly while balancing the responsibilities of raising our three children. I thank my children for their encouragement and for the motivation they continuously gave me. Finally, I am thankful to my mother for her emotional support and for always being available to listen.

Artificial intelligence language models were used to assist with improving the clarity, structure, and linguistic quality of the manuscript. The scientific ideas, experimental work, data analysis, and interpretation presented in this thesis are entirely those of the author.

Contents

Acknowledgements **2**

1 INTRODUCTION **5**

2 LITERATURE REVIEW **7**
2.1 Silicon Photonic Optomechanical Sensors . . . 7
2.2 Suspended 2D Material Membranes in Nanomechanical Resonators . . . 10
2.3 Photonic Readout of Nanomechanical Motion at 1550 nm . . . 12
2.4 Actuation Methods for 2D Material Membranes . . . 15
2.4.1 Electrostatic Actuation . . . 16
2.4.2 Electrothermal Actuation . . . 17
2.4.3 Optothermal (Photothermal) Actuation . . . 17
2.5 Summary and Transition to Research Gap Analysis . . . 18

3 DISCUSSION **19**

4 EXPERIMENTAL STRATEGY AND HYPOTHESES **22**

5 THEORETICAL FRAMEWORK **24**
5.1 Mechanisms of Optothermal Actuation . . . 24
5.1.1 Effect of Direct Thermal Loading on a Homogeneous Multilayer hBN Drum . . . 24
5.1.2 Effect of Isolated Mechanical Stress Transfer from Graphene Flake to hBN Drum . . . 25
5.1.3 Coupled Bimorph Actuation in Graphene/hBN Heterostructure . . . 25
5.1.4 Derivation of the Bimorph Deflection Scaling Relation . . . 26
5.2 Theoretical Modelling of Optothermal Actuation . . . 29
5.2.1 Optical absorption and steady-state temperature rise . . . 29
5.2.2 Conversion of temperature rise into mechanical deflection . . . 29
5.2.3 Thermal low-pass filtering under intensity modulation . . . 29
5.2.4 Dynamic deflection amplitude at mechanical resonance . . . 30
5.3 Actuation Efficiency . . . 30
5.4 Predicted Parametric Trends . . . 31

6 EXPERIMENTAL METHODOLOGY **32**
6.1 Device Fabrication and Heterostructure Transfer . . . 32
6.2 Optical Characterization Setup for Silicon Photonic Ring Resonators . . . 33
6.2.1 Light Source and Polarization Control . . . 33
6.2.2 Photonic Chip and Fiber Alignment . . . 33
6.2.3 Imaging and Alignment System . . . 34
6.2.4 Detection and Readout . . . 34
6.2.5 Auxiliary Equipment . . . 34
6.2.6 Measurement Principle . . . 34
6.3 Measurement Procedures for Spectral Characterization . . . 34
6.4 Optothermal Actuation Measurement Configurations . . . 35
6.4.1 Single-Laser Intensity-Modulated Actuation (Setup 1) . . . 35
6.4.2 Dual-Laser Actuation Attempt (Setup 2) . . . 36
6.4.3 Rationale for Adoption of Setup 1 . . . 37

6.4.4 Signal Conversion in the Moku:Lab Spectrum Analyzer . . . 37

7 MEASUREMENT ANALYSIS **39**
7.1 Device and Measurement Overview . . . 39
7.2 Passive Optical Characterization . . . 40
7.2.1 Theoretical Background: Resonance Condition and Free Spectral Range . . . 40
7.2.2 Pre-Transfer Transmission Spectrum and Ring Identification . . . 40
7.2.3 Comparison of the Transmission Spectra Before and After Transfer . . . 43
7.2.4 Discussion of the Observed Resonance Shift Direction . . . 46
7.3 Optothermal Actuation and Driven Response . . . 48
7.3.1 Verification of basic functionality . . . 48
7.3.2 Multi-frequency spectra at 15 mVpp . . . 48
7.3.3 Extraction of absolute and excess spike heights . . . 48
7.3.4 Amplitude-domain interpretation of the coherent response . . . 50
7.3.5 Quantitative extraction of the coherent amplitude . . . 51
7.3.6 Estimated driven displacement – supplementary quantitative analysis . . . 52
7.3.7 Interpretation and limitations . . . 54

8 DISCUSSION **55**
8.1 Synthesis of Optical and Mechanical Results . . . 55
8.2 Relation to the Theoretical Framework . . . 55
8.3 Limitations . . . 55
8.4 Assessment of competing mechanisms . . . 56
8.5 Answer to the Research Question . . . 58

9 CONCLUSIONS **59**

Appendices **65**
A Supporting Calculations for Actuation Force Comparison . . . 65
B Thermal Low-Pass Filtering: DC versus AC Temperature Response . . . 66
C Experimental Methodology . . . 68
C.1 Photographic Documentation of Device Fabrication and Heterostructure Transfer . . . 68
D Detailed Photographs and Specifications of the Experimental Optical Setup . . . 71
E Numerical evaluation of $\int S_{VV}(f)\,\mathrm{d}f$ . . . 75

Chapter 1

INTRODUCTION

Nanomechanical resonators have emerged as one of the most powerful transducers for precision sensing due to their exceptional sensitivity to external perturbations. Mechanical quantities such as force, mass, pressure and acceleration can be converted into measurable changes in the resonator's vibration characteristics, including its resonance frequency, amplitude and quality factor. Owing to their small mass, high resonance frequencies and excellent mechanical properties, nanomechanical resonators have enabled measurements that are difficult or impossible to achieve using conventional microscale sensing technologies. Consequently, they have become an important platform for applications ranging from precision force and mass sensing to cavity optomechanics and fundamental studies of light–matter interactions [1, 2, 3].

Recent advances in nanofabrication and optical readout techniques have significantly improved the displacement sensitivity of nanomechanical systems, allowing thermally driven (Brownian) motion to be resolved with remarkable precision. Thermomechanical motion provides valuable information about the mechanical properties of a resonator, including its resonance frequency, quality factor and damping, and has therefore become a widely used tool for passive nanomechanical sensing and device characterization [2, 3]. However, passive detection alone does not provide deterministic control over the mechanical motion. Since Brownian motion originates from stochastic thermal fluctuations, both the oscillation amplitude and, more importantly, the oscillation phase evolve randomly with time. As a result, the resonator cannot be coherently driven or synchronized to an external reference signal.

Providing deterministic control over the mechanical motion represents an important step beyond passive observation. By actively driving the resonator, its oscillation can be excited with a well-defined frequency and phase, enabling coherent measurements that are inaccessible under purely thermal excitation. Such phase-controlled operation forms the basis of lock-in detection techniques, coherent mechanical characterization and phase-sensitive measurements, while simultaneously providing access to nonlinear dynamical regimes. Driven nanomechanical resonators have been shown to exhibit rich nonlinear phenomena, including Duffing nonlinearities, bistability and bifurcation behaviour, which have attracted considerable interest because of their potential for enhanced sensing and signal processing [4, 5, 6]. Consequently, the current research focus within nanomechanics is increasingly shifting from merely detecting mechanical motion towards achieving deterministic and controllable actuation of nanomechanical systems.

Realising such controllable actuation within a fully integrated platform remains a significant challenge. Many existing actuation approaches rely on bulky free-space optical setups, external piezoelectric shakers or electrostatic electrodes, which complicate system integration and reduce scalability. Integrated photonics offers an attractive alternative by combining high displacement sensitivity with compactness, CMOS compatibility and the potential for large-scale multiplexed sensing. Developing an integrated nanomechanical platform that not only detects but also actively controls mechanical motion would therefore represent an important step towards more versatile optomechanical systems capable of coherent operation.

Recent developments in silicon photonics have created new opportunities for integrating nanomechanical resonators within compact and scalable optical circuits. By confining light inside subwavelength waveguides and resonant photonic structures, silicon photonic devices enable highly sensitive optical transduction while maintaining the advantages of CMOS-compatible fabrication and wafer-scale integration [7, 8]. Unlike free-space optical detection schemes, integrated photonic architectures eliminate complex optical alignment and facilitate the realization of compact optomechanical systems suitable for large-scale deployment. These characteristics

have established integrated photonics as a promising platform for next-generation nanomechanical sensing.

Within this context, two-dimensional (2D) materials have attracted considerable interest as nanomechanical resonators owing to their exceptional mechanical and optical properties. Their atomic-scale thickness, low mass density and high Young's modulus enable large mechanical responsivity while minimizing optical losses when integrated with photonic circuits. Among these materials, hexagonal boron nitride (hBN) is particularly attractive due to its wide optical bandgap, excellent chemical stability and mechanical robustness, making it highly compatible with silicon-photonic devices operating at telecommunication wavelengths [10, 11, 12]. These properties make suspended hBN membranes promising candidates for integrated optomechanical systems capable of operating in both gaseous and liquid environments.

Recent work within our research group has demonstrated the successful integration of suspended hBN membranes with silicon-photonic rib waveguides, enabling optical detection of thermomechanical (Brownian) motion in both air and water. This represents an important milestone, as it demonstrates that the integrated photonic readout possesses sufficient displacement sensitivity to resolve the intrinsic thermal vibrations of the membrane without requiring external interferometric techniques. Furthermore, operation in liquid environments significantly expands the potential application space of the platform towards biological and chemical sensing, where conventional high-quality-factor nanomechanical resonators often suffer from strong viscous damping.

Despite these advances, the demonstrated platform remains fundamentally a passive nanomechanical system. The membrane motion is entirely driven by stochastic thermal fluctuations, while no integrated mechanism currently exists to excite the resonator in a deterministic and controllable manner. Consequently, although the platform is capable of passive mechanical characterization, it cannot yet exploit coherent excitation schemes that require precise control over the oscillation phase and amplitude. This limitation currently prevents investigation of nonlinear dynamical behaviour, phase-sensitive measurement techniques and other advanced operating regimes that rely on actively driven mechanical motion.

To address this limitation, this thesis investigates the integration of an optothermal actuator based on a partially transferred multilayer graphene flake. Because graphene has strong optical absorption at 1550 nm and excellent thermal conductivity, it provides a promising mechanism for locally generating thermoelastic stresses while remaining compatible with the existing silicon-photonic architecture. By transferring optical energy into controlled mechanical motion through optothermal coupling, graphene offers a pathway towards deterministic actuation without introducing metallic electrodes or compromising the compactness of the integrated platform. Achieving such controllable actuation would transform the current passive hBN optomechanical sensor into an actively driven nanomechanical system, providing the foundation for future studies involving coherent excitation, nonlinear dynamics and phase-sensitive sensing.

The objective of this thesis is therefore to establish the missing capability required for deterministic control of the integrated hBN nanomechanical platform. Rather than relying solely on stochastic thermomechanical motion, this work investigates whether optothermal actuation can provide controlled excitation of suspended hBN resonators while preserving the compact, electrode-free architecture of the silicon-photonic platform. Graphene is employed as the optothermal transducer due to its strong optical absorption and excellent thermal conductivity, enabling efficient conversion of optical power into localized thermoelastic actuation.

To realise this objective, an experimental approach is followed by introducing deterministic actuation into a platform that has thus far been limited to passive Brownian motion detection. The research presented in this thesis is guided by the following research question:

"How can controllable actuation of hBN nanomechanical resonators be achieved within an integrated photonic platform?"

This question is addressed by investigating whether intensity-modulated optical absorption in a partially transferred multilayer graphene flake can provide deterministic optothermal actuation of a suspended hBN membrane while the same laser is used for photonic readout.

Chapter 2

LITERATURE REVIEW

This chapter reviews the key technological and material developments that enable ultra-sensitive optomechanical sensing using integrated photonics. First, silicon photonic ultrasound sensors and their performance limits are discussed. Next, the mechanical and optical properties of two-dimensional materials suitable for nanomechanical resonators are examined. The chapter then reviews photonic readout mechanisms and actuation strategies before identifying the research gap addressed in this thesis.

2.1 Silicon Photonic Optomechanical Sensors

The integration of ultra-sensitive, compact mechanical sensors within photonic integrated circuits (PICs) addresses critical demands in high-resolution sensing applications, such as biomedical imaging and precision metrology. These sensors leverage optomechanical coupling to transduce acoustic or mechanical signals into optical-domain shifts. In this mechanism, a mechanical displacement δz of a suspended membrane modulates the effective refractive index n_{eff} of a guided optical mode (typically at 1550 nm), producing a measurable shift in the resonance wavelength of a photonic cavity or a phase change in an interferometer. This approach offers significant advantages in sensitivity, bandwidth, and scalability compared to traditional piezoelectric transducers, whose noise-equivalent pressure (NEP) scales inversely with sensor area. Key performance metrics include NEP, operational bandwidth, and spatial resolution, with CMOS compatibility enabling dense arrays and on-chip multiplexing for reduced interconnection complexity.

Early developments in photonic ultrasound sensors focused on polymer-based micro-ring resonators to achieve high-frequency detection. For instance, Chao et al. (2007) [20] demonstrated polymer microring resonators with apertures around 60 µm, attaining sensitivities suitable for photoacoustic imaging but limited by the low refractive index contrast (< 0.5), which constrained further miniaturization and optical confinement.

Subsequent advancements incorporated silicon photonics for enhanced performance. Hazan et al. (2019) [21] enhanced silicon-photonics-based ultrasound detection by applying a benzocyclobutene (BCB) coating to silicon waveguides, improving sensitivity through optimized photoelastic modulation of the effective refractive index. This approach yielded wavelength-shift sensitivities of $(21 \pm 3.2) \times 10^{-6}\,\text{MPa}^{-1}$ for the TM mode and $(2.7 \pm 0.41) \times 10^{-6}\,\text{MPa}^{-1}$ for the TE mode at a 15 MHz ultrasound frequency, representing a ten-fold improvement over bare silicon for TM polarization and demonstrating robustness against surface acoustic wave interference, thereby paving the way for practical biomedical applications.

Building on this, Shnaiderman et al. (2020) [22] introduced a submicrometre silicon-on-insulator resonator (SWED) for ultrasound detection, achieving a noise-equivalent pressure (NEP) of $9\,\text{mPa}\,\text{Hz}^{-1/2}$ over bandwidths reaching 230 MHz with a sub-micron aperture, providing per-area sensitivity 10^4-fold higher than polymer microrings and enabling extreme miniaturization.

The evolution toward smaller gaps and higher coupling continued with Westerveld et al. (2021), who developed a split-rib waveguide in silicon photonics with a 15 nm air gap, integrated into a ring resonator for optomechanical ultrasound sensing (OMUS). In this design (Figure 2.2), a fixed silicon rib (width 450 nm, height 170 nm) and a movable silicon slab (thickness 60 nm) are separated by the narrow air gap. The fundamental quasi-TE optical mode is strongly confined within this gap due to evanescent-field coupling, the evanescent tail of the mode extends across the low-index air region, producing an extremely high electric-field intensity inside the gap. This occurs because the optical mode extends beyond the waveguide boundary into the surrounding medium as an evanescent field, making the effective refractive index highly sensitive to changes in the gap geometry. A

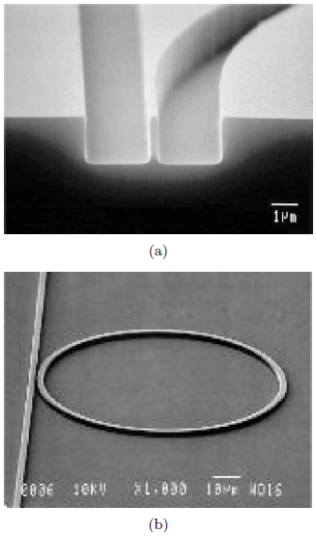


Figure 2.1: Scanning electron micrographs of the polymer microring resonator from Chao et al. (2007). (a) Top view showing the microring coupled to a bus waveguide (and drop port in this example), and (b) cross-sectional view of the polymer waveguide structure. These images illustrate the early implementation of microring-based ultrasound detection using low-index-contrast polymer materials. [20]

mechanical displacement δz of the suspended SiO_2 membrane modulates the gap height δg, inducing a large change in the effective refractive index ($\partial n_{\text{eff}}/\partial g \approx 10^{-2}$–$10^{-1}$ per nanometre at $g = 15\,\text{nm}$). The resulting optical resonance shift in the ring resonator is

$$\Delta\lambda = \lambda \cdot \frac{\Delta n_{\text{eff}}}{n_{\text{g}}}, \tag{2.1}$$

where n_{g} is the group index. This yields a wavelength-shift sensitivity of approximately $35\,\text{fm}\,\text{Pa}^{-1}$ at the acoustomechanical resonance [19].

Optical readout is performed by tuning a narrow-linewidth laser to the steep flank of the resonator transmission spectrum. Any resonance shift $\Delta\lambda$ is converted into an intensity modulation ΔI at the photodetector:

$$\Delta I \propto \left|\frac{\mathrm{d}T}{\mathrm{d}\lambda}\right| \cdot \Delta\lambda, \tag{2.2}$$

where $T(\lambda)$ is the transmission. This cavity-enhanced scheme enables broadband operation (dominated by acoustomechanical noise) with NEP $< 1.3\,\text{mPa}\,\text{Hz}^{-1/2}$ over 3–30 MHz, a 20 µm membrane diameter, and fine-pitch arrays ($< 50\,\mu\text{m}$) via photonic multiplexing—surpassing piezoelectric equivalents by two orders of magnitude. While these devices demonstrate impressive sensitivity, their reliance on silicon membranes introduces limitations in mechanical tunability and thermal-noise suppression, which restricts performance in ultra-low force sensing regimes.

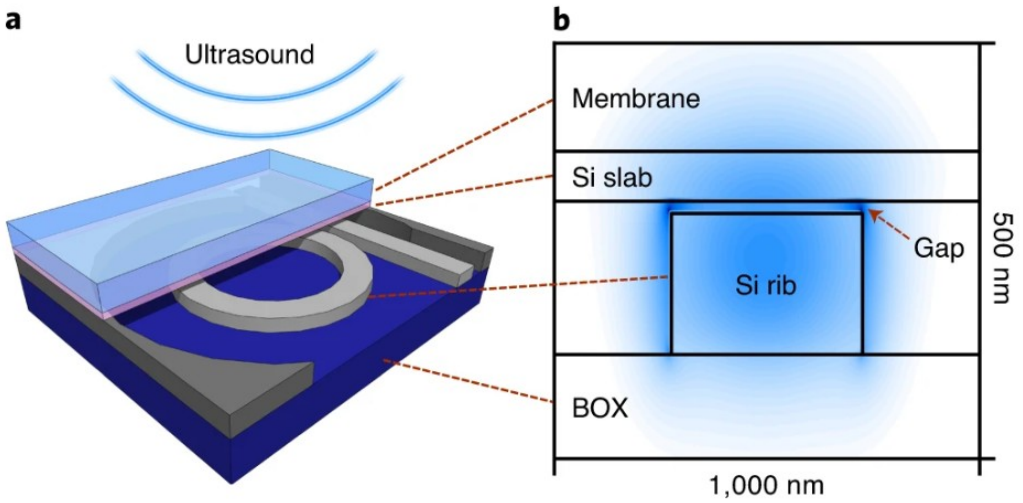


Figure 2.2: a,b, Schematic of the OMUS (a) and of the split-rib waveguide with a tiny gap (b) showing the silicon dioxide lower cladding (BOX) and upper cladding (membrane). Dimensions: silicon rib width, 450 nm; silicon rib height, 170 nm; air gap height, 15 nm; silicon slab height, 60 nm. Overlaid is a plot of the simulated electric field intensity of the waveguide mode, showing the high intensity in the gap. (adapted from Westerveld *et al.* [19]). The narrow air gap enables strong optomechanical coupling for broadband, high-sensitivity detection.

Further innovations extended photonic sensing to nanomechanical regimes. Rosłoń et al. (2022) employed suspended bilayer graphene drums (8 µm diameter) for detecting single-bacterium nanomotion. In this platform, mechanical displacement δz of the ultralow-mass graphene membrane directly modulates the reflected intensity of a probe laser via interferometric readout (Figure 2.3). The deflection at the drum centre is extracted from the intensity modulation, yielding motion amplitudes up to 20 nm and forces of ~ 6 nN. Although not strictly silicon-photonic, this work illustrates the potential of 2D materials in achieving femtometre-scale displacement sensitivity. The mechanical-to-optical coupling here relies on direct reflection rather than cavity enhancement, providing a useful contrast to the ring-resonator approach of Westerveld et al.

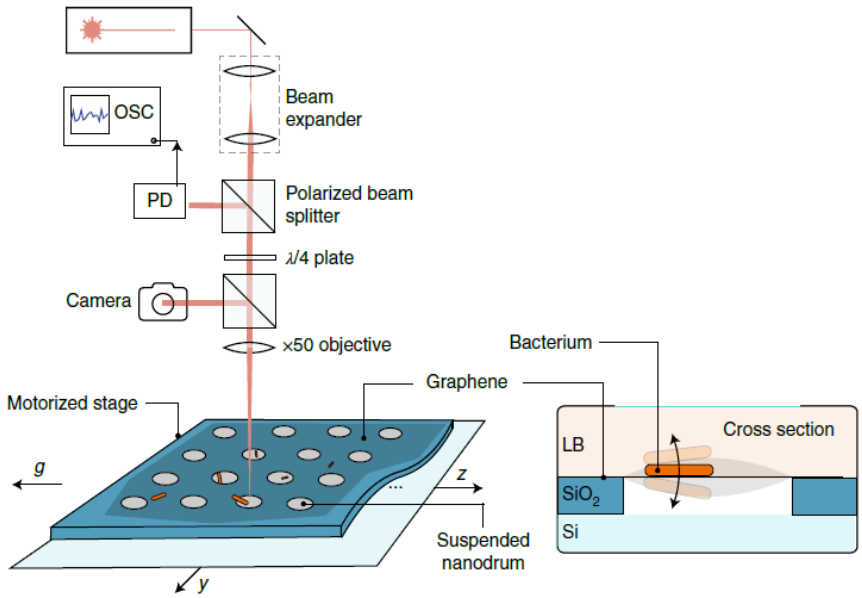


Figure 2.3: Ultrasensitive graphene drum resonator with interferometric readout (adapted from Rosłoń *et al.* [16]). Schematic of the interferometric measurement setup used to record the nanomotion. OSC and PD stand for oscilloscope and photodiode, respectively.

Both the graphene drum resonators demonstrated by Rosłoń et al. and the silicon-photonic optomechanical

ultrasound sensors reported by Westerveld et al. rely on photonic readout techniques, albeit implemented in different configurations. Optical detection, whether through direct interferometric modulation of reflected light or cavity-enhanced resonance-shift readout, offers the highest displacement sensitivity among available transduction methods, outperforming piezoresistive (strain-induced resistance changes) and capacitive (displacement-induced capacitance variations) approaches, particularly at the sub-nanometre and femtometre scales required for ultra-sensitive nanomechanical sensing[16]. This superiority stems from the low-noise characteristics of optical measurements at telecom wavelengths, the absence of direct electrical connections to the moving structure (reducing parasitic effects and enabling operation in liquid environments), and the intrinsic amplification provided by high-finesse optical resonators. Consequently, photonic readout is essential for resolving Brownian motion and biomolecular forces in challenging media, providing the common foundation upon which hybrid 2D-material integration strategies can be developed.

Integrating 2D materials into setups akin to Rosłoń's within silicon-photonic frameworks, such as Westerveld's split-rib waveguides, could combine the ultra-low mass and high Q-factors of 2D membranes with evanescent-field coupling, enabling femto-Newton force detection. This synergy represents the best of both worlds: the scalability and optical precision of silicon photonics with the mechanical superiority of 2D materials. To realise this, a deeper understanding of 2D material properties and photonic readout mechanisms is essential, as explored in Section 2.2 and Section 2.3 consecutively.

2.2 Suspended 2D Material Membranes in Nanomechanical Resonators

The integration of two-dimensional (2D) materials into nanomechanical resonators has revolutionized the field of optomechanical sensing due to their unique atomic-scale properties. These materials, characterized by their monolayer or few-layer thickness, exhibit exceptional mechanical strength, low mass density, and high elastic moduli, making them ideal for fabricating suspended membranes that can achieve ultra-high sensitivity in detecting minute forces and displacements [12]. Unlike bulk materials such as silicon or silicon dioxide, 2D materials enable resonators with reduced inertial mass, leading to higher resonant frequencies and quality factors (Q-factors), which are crucial for applications requiring femtometer-scale resolution [55]. Key properties influencing their performance include Young's modulus (E), mass density (ρ), pretension (σ_0), optical absorption, thermal conductivity, refractive index, and chemical stability. These attributes allow for tunable mechanical responses and compatibility with photonic readout schemes at telecom wavelengths (e.g., 1550 nm).

Graphene, the archetypal 2D material, possesses a Young's modulus of approximately 1 TPa, a density of 2200 $\mathrm{kg/m^3}$, and intrinsic pretension levels that can be engineered during fabrication [12]. Its high mechanical stiffness combined with atomic thickness results in resonators with fundamental frequencies in the MHz range and Q-factors exceeding 10^4 in vacuum [23]. Graphene's optical absorption of about 2.3 % per layer at visible and near-infrared wavelengths enables efficient photothermal actuation, but it also introduces challenges such as potential contamination and moderate chemical stability [16]. Seminal works, such as those by Bunch et al. [12], demonstrated the first suspended graphene resonators, highlighting their use in mass sensing with attogram resolution. More recently, Rosłoń et al. [16] utilized bilayer graphene drums (8 μm diameter) for detecting single-bacterium nanomotion, achieving deflection sensitivities up to 20 nm through interferometric readout, underscoring graphene's potential in biological sensing applications where low mass enhances responsiveness to biophysical forces.

Hexagonal boron nitride (hBN), often referred to as "white graphene," offers complementary properties with a Young's modulus of around 0.8–1 TPa, a lower density of approximately 2100 $\mathrm{kg/m^3}$, and near-zero optical absorption at 1550 nm, making it highly transparent and suitable for photonic integration without significant light loss [24]. hBN exhibits superior chemical inertness and thermal stability compared to graphene, with Q-factors in resonators reaching up to 10^5 in certain regimes due to reduced damping [25]. These characteristics make hBN ideal for applications requiring minimal optical interference, such as in hybrid optomechanical systems. Studies by Weber et al. [24] explored hBN resonators for quantum optomechanics, demonstrating high-frequency operation and low dissipation. Lee et al. [25] further showed hBN's utility in strain-engineered devices, achieving tunable resonances for force sensing in nanoscale environments.

Transition metal dichalcogenides (TMDs), such as molybdenum disulfide (MoS_2) and tungsten disulfide (WS_2), expand the repertoire of 2D materials for nanomechanical resonators. MoS_2 has a Young's modulus of 0.27–0.33 TPa, a density of about 5000 $\mathrm{kg/m^3}$, and bandgap-dependent optical properties that allow for tunable absorption in the visible to near-infrared range [26]. Its semiconducting nature enables electrical actuation and readout, complementing optical methods. Castellanos-Gomez et al. [26] fabricated suspended MoS_2 membranes, reporting Q-factors around 10^3–10^4 and applications in pressure sensing with sensitivities down to 10^{-6} bar. Similarly, WS_2 offers a higher Young's modulus (~ 0.3 TPa) and enhanced photoluminescence, making it suitable

for optomechanical cavities [15]. These TMDs are particularly relevant for multifunctional resonators that combine mechanical sensing with electronic or optoelectronic properties, such as in wearable sensors or integrated photonics for gas detection.

For comparison, conventional materials like silicon nitride (Si_3N_4) are widely used in photonic waveguides and membranes due to their low propagation loss ($\sim 2\,\mathrm{dB/cm}$ at 1550 nm) and compatibility with CMOS processes [19, 27]. However, Si_3N_4 membranes typically have higher mass compared to 2D materials when scaled to similar dimensions, limiting sensitivity in ultra-low force detection.

The refractive indices at 1550 nm further determine the strength of evanescent-field coupling in the split-rib waveguide ring resonators used for photonic readout. Graphene presents a complex refractive index $\tilde{n} \approx 2.6{+}1.3i$ [28], supporting efficient optothermal actuation through its absorption while contributing to the high electric-field intensity inside the 15 nm air gap. Hexagonal boron nitride maintains a real refractive index $n \approx 2.13$ (in-plane) with negligible imaginary part [29], ensuring low-loss transparency ideal for high-Q photonic interrogation. Molybdenum disulfide exhibits $n \approx 3.5$ (monolayer, in-plane) [30], while stoichiometric Si_3N_4 has $n \approx 2.00$ [19, 31], providing the benchmark for CMOS-compatible low-propagation-loss membranes. These optical constants, together with the mechanical properties summarised in Table 2.1, enable hybrid graphene/hBN membranes to combine photothermal actuation efficiency with minimal readout loss.

Hybrid stacks combining different 2D materials leverage synergistic properties; for instance, graphene/hBN heterostructures combine graphene's absorption for actuation with hBN's transparency for readout, potentially enhancing overall device performance [16]. Such hybrids have been explored for reducing damping and improving Q-factors, as demonstrated in van der Waals heterostructures for quantum sensing [25].

In summary, the choice of 2D material depends on the specific requirements of the resonator, such as optical transparency, actuation efficiency, and environmental stability. While graphene excels in applications demanding high absorption and conductivity, hBN and TMDs like MoS_2 offer advantages in transparency and tunability. These materials have enabled breakthroughs in ultra-sensitive sensing, from single-molecule detection to biological nanomotion analysis, paving the way for advanced hybrid optomechanical platforms.

Table 2.1 summarizes the most relevant material properties of graphene, hBN, MoS_2, and Si_3N_4 for nanomechanical resonator applications, highlighting why these two-dimensional materials are particularly suited for ultra-sensitive optomechanical sensing.

Table 2.1: Comparison of material properties relevant to nanomechanical resonator applications in silicon-photonic optomechanics (1550 nm operation). Refractive indices enable quantitative assessment of evanescent-field coupling strength and photonic loss in hybrid hBN/graphene membranes.

Property	**Graphene**	**hBN**	**MoS_2**	**Si_3N_4**
Thickness (nm)	0.34	0.33	0.65	100–500
Young's modulus (TPa)	1.0	0.87	0.27	0.25
Breaking strength (GPa)	130	∼100	23	∼10
Areal density (mg/m^2)	0.77	0.76	3.1	310 (for 100 nm)
Optical absorption at 1550 nm (%)	∼2.3	negligible	∼1-2	negligible (loss ∼2 dB/cm)
Bandgap (eV)	0 (semi-metal)	5.9 (insulator)	1.8 (direct)	∼5 (insulator)
Refractive index at 1550 nm	$2.6 + 1.3i$ (complex $\tilde{n}$)	≈ 2.13 (in-plane)	≈ 3.5 (monolayer, in-plane)	≈ 2.00 (stoichiometric)
Typical Q-factor range (vacuum)	10^3–10^5	10^4–10^5	10^3–10^4	10^5–10^7
Key advantage for optomechanics	Strong absorption for efficient photothermal actuation	High transparency and chemical stability for low-loss photonic readout	Tunable bandgap for electrical gating and multifunctional sensing	Low propagation loss and CMOS compatibility for waveguides and membranes

2.3 Photonic Readout of Nanomechanical Motion at 1550 nm

Photonic transduction of nanomechanical motion at telecom wavelengths (1550 nm) converts the displacement of a suspended membrane into a measurable optical signal through modulation of the guided-mode effective index. This section compares two readout schemes, the cavity-enhanced approach demonstrated by Westerveld et al. (2021) [19]and the direct interferometric readout demonstrated by Rosłoń et al. (2022)[16].

In the cavity-enhanced approach, the strip waveguide is closed into a photonic ring resonator. A tunable laser is locked to the linear flank of a resonance (typically at the point of maximum slope). When the suspended drum vibrates out-of-plane, the gap height g oscillates with amplitude $\Delta g = \Delta z$. This modulates the effective index of refraction $n_{\text{eff}}(t)$ and shifts the entire resonance wavelength by $\Delta\lambda(t)$. Because the laser wavelength is fixed, the resonance shift is directly converted into an intensity modulation at the photodetector output:

$$\Delta I(t) \propto \left|\frac{dT}{d\lambda}\right| \cdot \Delta\lambda(t), \tag{2.3}$$

where $T(\lambda)$ is the resonator transmission. This intensity signal is proportional to the membrane displacement $\Delta g = \Delta z$ and is recorded with a high-bandwidth photoreceiver. The method provides intrinsic wavelength-to-intensity conversion gain (typically 10–100 times higher than direct interferometry) and benefits from the high Q-factor of the ring resonator ($Q \sim 10^4$–10^5), enabling sub-femtometer displacement resolution when combined with the ultra-low mass of the 2D drum.

In comparison, direct interferometric readout (as used by Rosłoń et al. (2022) [16] for graphene drums) relies on a free-space or fiber-based Michelson or Fabry–Pérot interferometer to measure absolute membrane deflection via phase shift of reflected light (Figure 2.3). While conceptually simpler and capable of nanometre-scale sensitivity, interferometry lacks the on-chip multiplexing and high-finesse amplification of a photonic ring resonator. It also requires precise alignment of an external laser beam, which is incompatible with dense sensor arrays or fully integrated photonic circuits.

In the strip waveguide geometry employed in this work, the transduction is almost exclusively sensitive to the

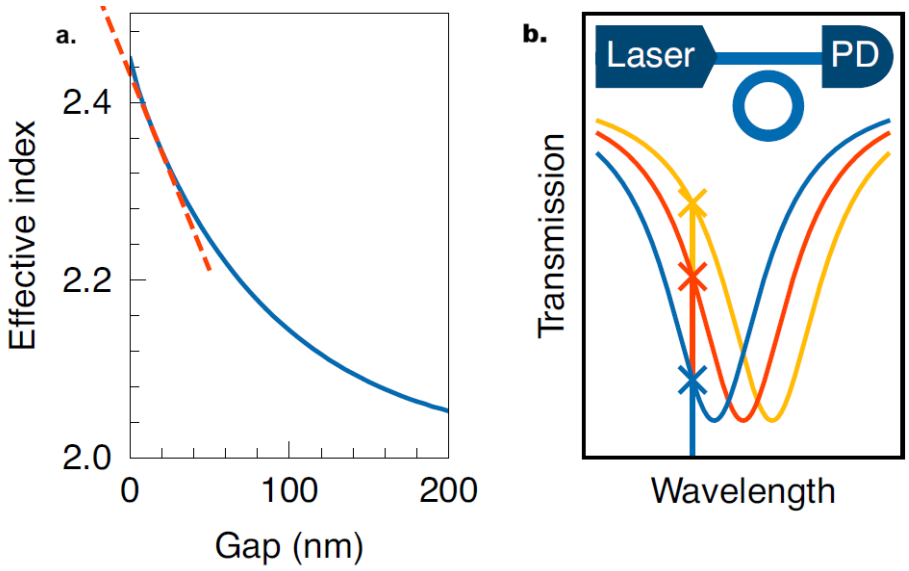


Figure 2.4: a. Simulated waveguide effective refractive index as a function of the gap height. The sensitivity of this sensor scales with the tangent of this curve (plotted at a 15 nm gap). b. Resonance wavelength shift with gap modulation in a split-rib ring resonator (adapted from Westerveld et al. [19])

out-of-plane component of membrane motion. The reason is geometric: the optical mode is strongly confined within the narrow vertical air gap between the fixed silicon strip and the suspended 2D drum. Any vertical displacement Δz of the 2D drum (see Figure 2.5) directly modulates the gap height g ($\Delta g = \Delta z$), producing a large change in the effective index of refraction n_{eff} according to

$$\Delta\lambda \approx \frac{\lambda}{n_g}\frac{\partial n_{\text{eff}}}{\partial g}\Delta g, \tag{2.4}$$

where $\partial n_{\text{eff}}/\partial g \approx -0.02$ nm^{-1}. Consequently, the photonic resonance shift observed in this platform can be attributed entirely to out-of-plane membrane vibration. In contrast, in-plane displacements couple to the optical mode substantially more weakly (typically by 1–2 orders of magnitude in similar evanescently coupled structures), as expected from the strong vertical field confinement in the 15 nm air gap and confirmed by the waveguide mode simulations [19]. Therefore, in-plane motion can be neglected for readout purposes.

The resonance-wavelength shift per unit pressure in the original OMUS device reached 35 fm Pa^{-1} at the acoustomechanical resonance (see Figure 2.4), with the displacement sensitivity scaling directly with the optomechanical coupling coefficient $\partial n_{\text{eff}}/\partial g$. In the present 2D drum implementation the same geometric coupling mechanism applies, so the expected photonic signal remains directly proportional to the out-of-plane displacement Δz induced by optothermal graphene actuation. This well-characterised readout chain forms the foundation for all experimental validation in this thesis.

While the photonic readout platform provides exceptional displacement sensitivity, resolving Brownian motion alone is insufficient for quantitative force or mass sensing. To fully exploit the ultra-low effective mass and high responsivity of the 2D membrane, the following section (Section 2.4) examines the principal actuation mechanisms suitable for these membranes integrated in silicon-photonic circuits.

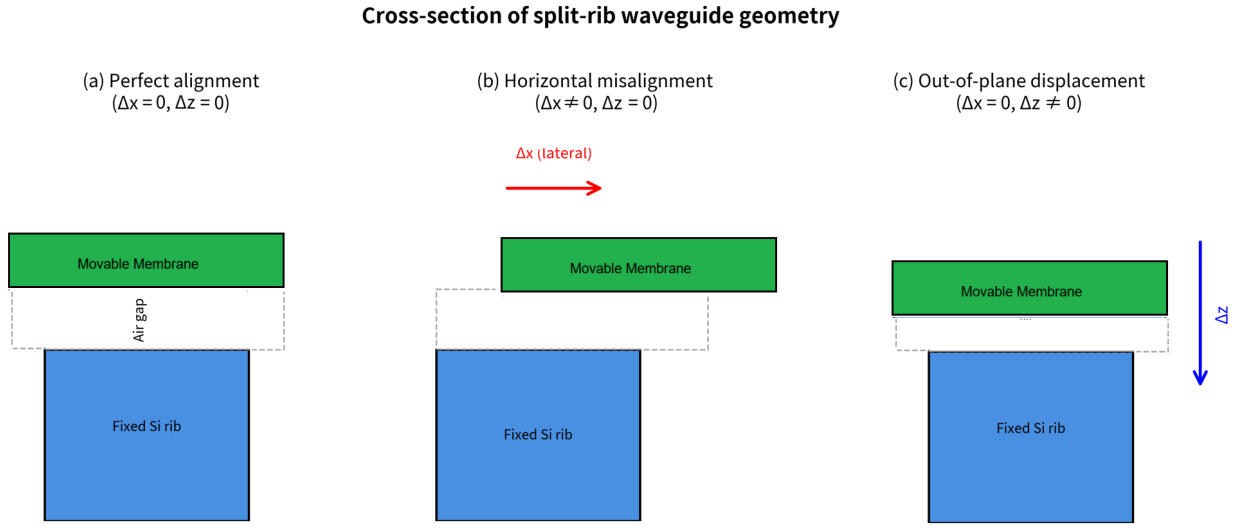


Figure 2.5: Cross-sectional schematic of the strip waveguide geometry used for photonic readout. (a) Perfect alignment ($\Delta x = 0$, $\Delta z = 0$). (b) Horizontal (lateral) misalignment Δx between the fixed Si strip and the suspended 2D membrane — this reduces mode overlap but produces only a weak change in n_{eff}. (c) Out-of-plane displacement Δz of the 2D drum membrane — this directly modulates the air-gap height and dominates the optomechanical coupling (50–200× stronger than the lateral effect).

2.4 Actuation Methods for 2D Material Membranes

Controlled actuation of suspended 2D material membranes is essential for dynamic characterisation, calibration of optomechanical sensitivity, and exploration of nonlinear regimes in nanomechanical resonators. For insulating materials such as multilayer hBN, which lack intrinsic conductivity, external actuation strategies are required to induce measurable out-of-plane vibrations without compromising the ultralow mass or optical transparency critical for high-sensitivity photonic readout.

Several actuation mechanisms have been demonstrated for 2D material resonators, primarily developed in graphene systems and adaptable to hBN or hybrid stacks. These methods can be broadly categorised as electrostatic, electrothermal (resistive/Joule heating), and optothermal (photothermal). A systematic comparison is presented in Table 2.2, highlighting their principles, advantages, limitations, and suitability for integration with silicon photonic strip waveguides.

For the comparative force and displacement calculations that follow, a standardized geometry is adopted: a circular membrane of radius $r = 10\,\mu$m suspended above a silicon strip waveguide with an air gap of $d = 60\,$nm. This gap is deliberately larger than the 15 nm gap of the original Westerveld device [19] as to reflect the fabricated actual fabricated device. Where optical sensitivity values are required, the $d\lambda/dg$ reported by Westerveld et al. is scaled to the 60 nm gap.

Table 2.2: Comparison of actuation methods for suspended 2D material membranes in optomechanical sensors.

Method	**Principle**	**Advantages**	**Limitations**
Electrostatic	Capacitive force Graphene electrode–substrate coupling	High force density Fast response (μs) Precise voltage control	Fabrication complexity (electrical contacts, isolation on dielectric hBN) Pull-in instability Parasitic capacitance
Electrothermal	Joule heating Current-driven thermal expansion	Localised heating Broadband actuation	Electrical contacts required Thermal hotspots Interface stress at high ΔT
Optothermal	Optical absorption Thermoelastic strain	electrode-free optothermal actuation Uses existing 1550 nm laser Low parasitics Compatible with aqueous environments	Slower thermal response (ms) Requires strong absorber (multilayer graphene)

Figure 2.6 illustrates the three actuation principles discussed in this section. Panel (a) shows electrostatic actuation via capacitive coupling between the suspended membrane (or a conductive layer on it) and a back-gate electrode. Panel (b) illustrates both optothermal actuation (local laser-induced heating followed by thermoelastic strain) and thermal actuation by resistive (Joule) heating. These schematics clarify the fundamental physical differences between the methods and highlight why material properties (conductivity and optical absorption) play a decisive role in the quantitative force comparison that follows.

To enable a direct, apples-to-apples comparison of actuation performance, we consider a standardized test structure matched to the target photonic platform: a circular suspended membrane of diameter 20 μm integrated into a silicon-photonic strip waveguide (silicon strip 450 nm × 170 nm, air gap 60 nm, slab thickness 60 nm, operating wavelength $\lambda = 1550\,$nm [19]). The fundamental resonance frequency is standardized to $f_0 \approx 5$–15 MHz in air, and all calculations employ the same clamped-plate mechanical model. Identical electrical and optical input limits are assumed across all actuation schemes, constrained to on-chip-compatible operating conditions ($< 5\,$V or $< 10\,$mW) to avoid thermal crosstalk with the sensing laser.

The drum material is varied across four candidates (multilayer graphene 5–70 nm, multilayer hBN, multilayer MoS_2, and 50 nm Si_3N_4 reference), with material-specific parameters (Young's modulus E, mass density ρ,

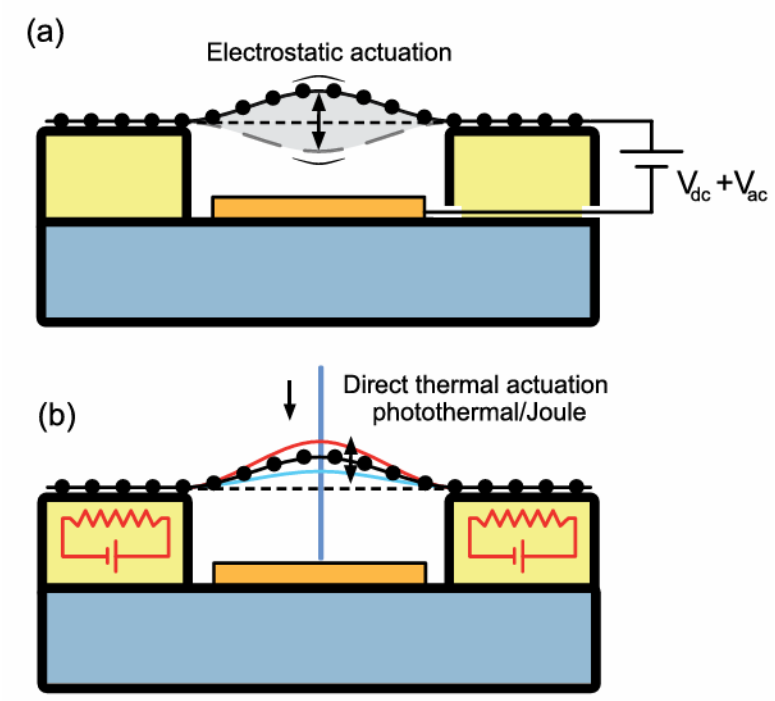


Figure 2.6: Actuation mechanisms for 2D material membranes. (a) Electrostatic actuation. (b) Optothermal actuation and thermal actuation by resistive heating. Adapted from Fig. 3 of Steeneken et. al[32].

residual tensile stress σ_0, and thickness h) taken from the literature values reported in Section 2.2 and standard references for each material. The optomechanical readout sensitivity $\mathrm{d}\lambda/\mathrm{d}g$ is scaled from the results of Westerveld *et al.* (2021) [19] to account for the larger 60 nm waveguide–membrane gap, yielding $\mathrm{d}\lambda/\mathrm{d}g \approx 0.8$–$1.2\,\mathrm{pm\,nm^{-1}}$ depending on the exact optical mode profile. This scaling remains valid across the four candidate drum materials because the evanescent-field intensity in the strip waveguide is overwhelmingly concentrated inside the air gap ($n = 1$); the ultra-thin membrane (5–70 nm) contributes only a second-order perturbation to $\mathrm{d}n_{\mathrm{eff}}/\mathrm{d}g$ irrespective of its refractive index. Consequently, material-specific corrections to $\mathrm{d}\lambda/\mathrm{d}g$ are typically below 20 % and do not alter the relative ranking of actuation forces shown in the subsequent tables. The mechanical response is described by a material-dependent effective spring constant k_{eff} that is calculated for each drum from its Young's modulus, thickness, pretension and the standardized geometry (see Eq. (A.1) in Appendix A or the clamped-membrane model in Section 2.2).

While the geometric and drive parameters are fixed for the standardized test structure, the actuation forces themselves depend strongly on the material properties of the drum (conductivity, optical absorption, coefficient of thermal expansion). To quantify this material dependence, we compare the delivered force for four candidate drum materials (multilayer graphene, multilayer hBN, multilayer MoS_2, and a 50 nm Si_3N_4 reference) under the standardized geometry and drive levels.

2.4.1 Electrostatic Actuation

Electrostatic actuation is one of the most widely adopted methods for driving suspended 2D material membranes in nanomechanical resonators. In the standardized photonic platform considered throughout this thesis, the suspended drum itself serves as the movable electrode while the fixed silicon slab of the strip waveguide (2.5) acts as the counter-electrode. No additional metallization or electrodes are deposited on the 2D membrane, thereby preserving full CMOS compatibility, optical transparency at 1550 nm, and consistency with the optothermal actuation scheme developed later in this work. A DC or AC voltage V applied between the membrane and the Si slab generates an attractive force arising from the capacitive energy stored in the air gap. This mechanism requires the membrane material to be sufficiently electrically conductive to enable uniform charge distribution and biasing.

The electrostatic pressure is approximated as [21]

$$p_{\mathrm{es}} = \frac{1}{2}\varepsilon_0 \frac{V^2}{d^2}, \tag{2.5}$$

where ε_0 is the vacuum permittivity and d is the nominal air gap. The total force on a circular drum of radius r is then $F_{\mathrm{es}} = p_{\mathrm{es}} \cdot \pi r^2$. Because the Si-slab counter-electrode is shared across all designs, F_{es} is identical for all *conductive* membranes under the same geometry and voltage. For electrically insulating materials (e.g., multilayer hBN or the Si_3N_4 reference), charge cannot be induced on the drum; hence $F_{\mathrm{es}} = 0$ and electrostatic actuation is not possible in this standardized, electrode-free configuration.

The forces obtained for conductive membranes are large. When these forces are inserted into the linear small-signal relation $\delta = F_{\mathrm{es}}/k_{\mathrm{eff}}$, the formal displacements reach hundreds of nanometres. Such values lie far outside the validity range of the linear model ($w \ll h$ and $w \ll d$). In reality the membrane would either contact the underlying waveguide or enter a strongly nonlinear regime long before these amplitudes are reached. Only the forces themselves are therefore retained for comparison; the linear displacements are not reported as physical predictions.

Table 2.3: Standardized electrostatic actuation (drum as movable electrode, fixed Si slab as counter-electrode; force is zero for non-conductive materials) at $V = 5\,\mathrm{V}$, $r = 10\,\mu\mathrm{m}$, $d = 60\,\mathrm{nm}$. The linear displacement $\delta = F_{\mathrm{es}}/k_{\mathrm{eff}}$ exceeds the validity range of the small-signal model and is therefore not listed.

Material	Actuation Force F_{es} (nN)	Effective k_{eff} (N/m)
Graphene (multilayer, 5−70 nm)	9660	≈ 10−20
hBN (multilayer)	0	≈ 20−50
MoS_2 (multilayer)	9660	≈ 12−30
Si_3N_4 (50 nm thick reference membrane)	0	≈ 200−500

Electrostatic actuation offers high force density and is readily demonstrated on graphene drums. It is also compatible with semiconducting 2D materials such as multilayer MoS_2 (provided appropriate biasing), but it is fundamentally incompatible with insulating membranes such as hBN in the present electrode-free photonic architecture. This limitation motivates the exploration of contact-free alternatives (optothermal actuation) for hBN-based devices.

2.4.2 Electrothermal Actuation

Electrothermal actuation exploits Joule heating (resistive) or the inverse piezoelectric effect. In resistive heating, an electrical current through a conductive membrane raises its temperature ΔT, inducing thermal expansion or contraction that generates in-plane stress. This stress couples to out-of-plane motion via the membrane's geometry. The effective thermal force can be approximated as [38]

$$F_{\mathrm{th}} \approx E\alpha\Delta T \cdot h \cdot 2\pi r \tag{2.6}$$

where α is the coefficient of thermal expansion and h is the membrane thickness. For non-centrosymmetric 2D materials such as odd-layer or multilayer MoS_2, the inverse piezoelectric effect provides an additional, voltage-controlled strain mechanism: an applied electric field E_{field} across the membrane thickness induces an in-plane strain $\varepsilon_{\mathrm{piezo}} = d_{31}E_{\mathrm{field}}$, where d_{31} is the transverse piezoelectric coefficient (typically 2−4 pm/V for multilayer MoS_2) [33]. Because this piezoelectric strain adds directly to the thermal strain, the combined effective actuation force becomes

$$F_{\mathrm{th+piezo}} \approx E(\alpha\Delta T + d_{31}E_{\mathrm{field}}) \cdot h \cdot 2\pi r. \tag{2.7}$$

The piezoelectric contribution is therefore included only for MoS_2 in the standardized force values of Table 2.4 (it is zero for graphene, hBN and Si_3N_4).

Standardized comparison assumes a DC power dissipation of 1 mW (realistic for on-chip resistive heaters) and the same 20 µm drum geometry. As in the electrostatic case, the linear relation $\delta = F/k_{\mathrm{eff}}$ yields formal displacements that greatly exceed the membrane thickness and the air gap. These values lie outside the validity range of the small-signal model and are not reported as physical predictions; only the actuation forces are retained for comparison. ffective stiffness values keff are those listed in Table 2.3

2.4.3 Optothermal (Photothermal) Actuation

Optothermal actuation uses a focused laser beam to induce local heating without electrical contacts. The absorbed optical power raises the membrane temperature, producing thermal stress via the coefficient of thermal expansion. The temperature rise is $\Delta T \approx \alpha_{\mathrm{opt}}P_{\mathrm{laser}}/G_{\mathrm{th}}$, where α_{opt} is the optical absorptance at the laser wavelength, P_{laser} is the incident laser power, and G_{th} is the thermal conductance from the heated membrane

Table 2.4: Standardized electrothermal actuation force (resistive heating at 1 mW) for different drum materials. Piezoelectric contribution is included for MoS_2. Linear displacements exceed the validity range of the small-signal model and are therefore omitted.

Material	Actuation Force F_{th} (nN)
Graphene (multilayer)	120–250
hBN (multilayer)	≈ 0
MoS_2 (multilayer)	60–150
Si_3N_4 (50 nm)	≈ 0

to the substrate. The resulting in-plane thermal stress $\sigma_{\mathrm{th}} \approx E\alpha_{\mathrm{th}}\Delta T$ couples to out-of-plane motion. The effective optothermal force therefore scales as

$$F_{\mathrm{opto}} \propto \alpha_{\mathrm{opt}} P_{\mathrm{laser}} \cdot E\alpha_{\mathrm{th}}/G_{\mathrm{th}}. \tag{2.8}$$

This scaling relation is derived in the dynamics review of Steeneken et al. (2021) [32]. Standardized comparison uses an incident laser power of 1 mW and the same 20 μm drum geometry. Absorption at 1550 nm is taken from literature values. As with the other two schemes, insertion of the calculated forces into the linear relation $\delta = F/k_{\mathrm{eff}}$ produces formal displacements far larger than the membrane thickness or the air gap. These values are outside the validity range of the small-signal model and are omitted from the table; only the forces are retained for comparison. The corresponding effective spring constants k_{eff} refer to the values reported in Table 2.3.

Table 2.5: Standardized optothermal actuation force at 1 mW laser power (telecom wavelength) for different drum materials. Linear displacements exceed the validity range of the small-signal model and are therefore omitted. Effective stiffness values k_{eff} are those listed in Table 2.3.

Material	Actuation Force F_{opt} (nN)
Graphene (multilayer, 5–70 nm)	150–400
hBN (multilayer)	Not Applicable
MoS_2 (multilayer)	80–200
Si_3N_4 (50 nm)	Not Applicable

The quantitative comparison in Tables 2.3–2.5 (combined with the qualitative overview in Table 2.2) reveals clear material-dependent strengths and limitations. Electrostatic actuation provides uniform force across materials but requires electrodes. Electrothermal methods favour conductive layers, while optothermal actuation at 1550 nm is dominated by optical absorption, rendering hBN and Si_3N_4 membranes practically unresponsive without an absorbing transducer.

2.5 Summary and Transition to Research Gap Analysis

The preceding sections have systematically examined the state-of-the-art in silicon-photonic optomechanical ultrasound sensors based on split-rib waveguides (Section 2.1), the mechanical and optical properties of suspended 2D material membranes (Section 2.2), photonic readout mechanisms at 1550 nm (Section 2.3), and the qualitative and quantitative performance of the three principal actuation strategies for 2D drums (Section 2.4). While these developments demonstrate impressive sensitivities and CMOS compatibility, they also reveal persistent material and integration constraints—most notably the trade-off between optical transparency, photothermal absorption, and electrode-free optothermal actuation in hybrid graphene/hBN systems integrated with electrode-less strip geometries.

Building on this synthesis, the following chapter (3) consolidates the identified shortcomings into a precise research gap and articulates the specific scientific and technological contributions of the present thesis. In particular, it quantifies the actuation-efficiency deficit for optothermally driven hBN membranes and delineates the experimental parameter space that must be addressed to realise controlled on-chip optomechanical sensing.

Chapter 3

DISCUSSION

The preceding chapter 2 has established two mature but disjoint technological platforms for ultra-sensitive optomechanical sensing. On the photonic side, silicon-based split-rib waveguide sensors (Westerveld et al., 2021) [19] achieve noise-equivalent pressures below $1.3\,\mathrm{mPa\,Hz^{-1/2}}$ over a broadband 3–30 MHz range by exploiting a 15 nm air-gap optomechanical coupling to a suspended SiO_2 membrane of 20 μm diameter. The resulting resonance-wavelength shift at 1550 nm is read out through a photonic ring resonator with CMOS-compatible multiplexing, overcoming the area-scaling limitations of piezoelectric transducers. On the nanomechanical side, suspended graphene drums (Rosłoń et al., 2022) [16] have demonstrated single-bacterium force detection ($\sim$ 6 nN) by leveraging the atomic thickness, high stiffness, and low mass of 2D materials, with interferometric readout yielding motion amplitudes up to 20 nm.

To realise the full potential of both platforms, it would be highly advantageous to integrate the CMOS-compatible photonic architecture and on-chip multiplexing of the Westerveld OMUS with the ultra-low mass and exceptional mechanical Q-factor of a suspended 2D-material membrane as demonstrated by Rosłoń et al. Such a hybrid device could deliver force sensitivities equal to, or even surpassing, those of the graphene-drum platform while preserving the practical scalability, broadband operation, and fibre-optic readout of the silicon-photonic sensor. In order to explore this possibility, a systematic qualitative and quantitative comparison of candidate 2D materials and compatible actuation methods was conducted.

A quantitative comparison of actuation mechanisms for membranes of identical geometry reveals a fundamental material incompatibility that neither platform has yet resolved (Tables 2.3–2.5). Electrostatic actuation delivers identical forces ($\approx 9.66\,\mu$N at 5 V) across all candidates but introduces electrode fabrication complexity and pull-in instability. Resistive thermal actuation is viable only for conductors such as multilayer graphene, albeit with added fabrication complexity. Optothermal (photothermal) actuation at the telecom wavelength of 1550 nm is selected in this work for its reduced setup complexity, full CMOS compatibility, electrode-free operation, direct use of the existing 1550 nm probe laser, low parasitic effects, and compatibility with aqueous environments; it is governed by optical absorption: multilayer graphene (5–70 nm) generates approximated actuation forces of 150–400 nN per milliwatt (owing to $\sim 2.3\,\%$ absorption per layer and a negative coefficient of thermal expansion $\alpha \approx -8 \times 10^{-6}\,\mathrm{K^{-1}}$), whereas hBN, MoS_2 (in the NIR), and Si_3N_4 produce essentially zero force because they are transparent at 1550 nm. Qualitatively, hBN emerges as the ideal membrane material for photonic readout—offering near-zero optical loss, ultra-low mass, high mechanical Q-factor, and chemical inertness—but it cannot be directly actuated optothermally. Conversely, graphene is an outstanding actuator yet cannot serve as the membrane because it would absorb and attenuate the 1550 nm probe light, degrading the evanescent-field coupling in the strip waveguide. Consequently, hybrid integration of a partially contacted multilayer graphene flake onto a suspended hBN membrane combines (see Figure 3.1) the best of both worlds: graphene's efficient optothermal actuation with hBN's near-perfect transparency, ultralow mass, and superior mechanical quality factor, thereby resolving the fundamental material incompatibility identified above.

With regard to the photonic readout of the nanomechanical motion in the chosen hybrid graphene/hBN platform, two principal schemes exist in the literature. The cavity-enhanced approach of Westerveld et al. (2021), based on a rib waveguide closed into a high-Q ring resonator, provides intrinsic wavelength-to-intensity conversion gain (typically 10–100×) by locking a narrow-linewidth laser to the steep flank of the resonance. This yields sub-femtometre displacement resolution when combined with the low-mass 2D membrane and is fully compatible with on-chip photonic multiplexing and CMOS fabrication. In contrast, the direct interferometric readout

employed by Rosłoń et al. (2022) relies on free-space or fibre-based Michelson/Fabry–Pérot detection of reflected intensity; while conceptually simple, it lacks on-chip integration, requires precise external alignment, and is incompatible with dense sensor arrays or the electrode-free strip geometry. For the hybrid graphene/hBN device integrated with the strip waveguide platform and optothermal actuation, the cavity-enhanced readout scheme is therefore adopted: it guarantees seamless compatibility with the silicon-photonic architecture, full CMOS compatibility, on-chip multiplexing, and maximum sensitivity without compromising the electrode free, electrode-free operation demanded by the actuation method.

Hybrid integration of a partially contacted multilayer graphene flake onto a suspended hBN membrane has been proposed in the broader 2D-materials literature for combining absorption-driven actuation with transparent readout [32], yet no experimental demonstration exists within a silicon-photonic strip waveguide architecture. In particular, the efficiency of force transfer across the van-der-Waals interface remains unquantified when the graphene contact area, flake thickness, and air-gap height are varied—parameters that are inherently uncontrolled in ex-situ transfer processes and directly modulate both the mechanical displacement amplitude and the resulting photonic resonance shift $\Delta\lambda \propto \Delta g$.

This literature review therefore identifies a clear research gap: the absence of a hybrid optomechanical platform that simultaneously exploits (i) the ultra-low-mass, transparent hBN membrane for high-Q photonic readout at 1550 nm and (ii) optothermal actuation via a partially contacted multilayer graphene flake.

The present thesis addresses this gap by experimentally validating the proposed hybrid actuation scheme on a silicon-photonic strip waveguide sensor. The work will measure the induced out-of-plane displacement of the hBN membrane and the corresponding shift in the photonic resonance. In doing so, it establishes the first on-chip demonstration of electrode-free, optothermally driven 2D-hybrid membranes for sensing.

THESIS QUESTION Can optothermal actuation via a partially contacted multilayer graphene flake induce detectable out-of-plane vibrations in a suspended hBN membrane integrated in a silicon-photonic strip waveguide at 1550 nm?

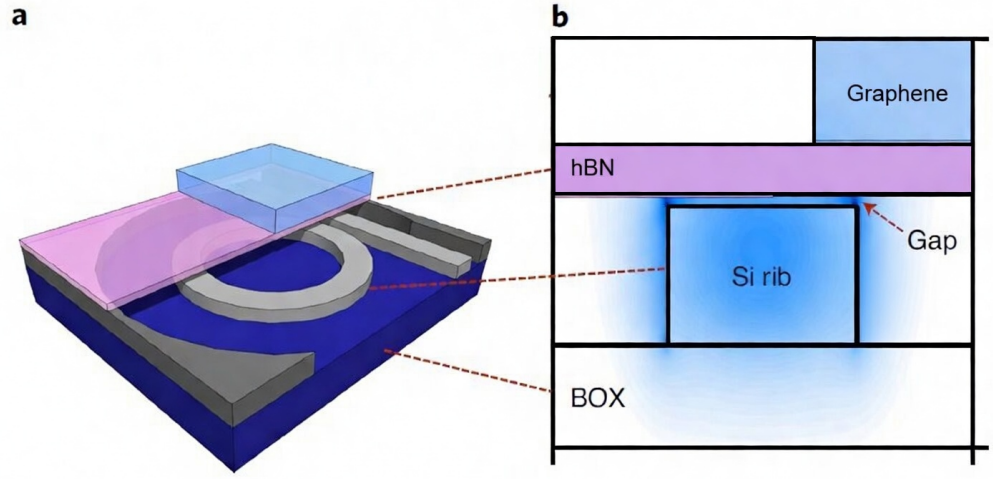


Figure 3.1: Schematic illustration of the hybrid hBN–graphene nano-optoelectromechanical system integrated on a silicon strip waveguide. (a) 3D representation showing the suspended hBN drum with a partially contacted graphene flake for optothermal actuation. (b) Cross-sectional view highlighting the graphene/hBN heterostructure positioned above the silicon strip waveguide with a nanoscale gap for enhanced optical–mechanical coupling. (adapted from Westerveld *et al.* [19]).

To mitigate potential risks associated with the primary optothermal actuation scheme, particularly those arising from variable van der Waals contact areas between the multilayer graphene flake and the hBN membrane, thermal interface resistances, or insufficient heat dissipation under constrained on-chip optical power at 1550 nm, a contingency Plan B has been incorporated. Should optothermal excitation fail to induce detectable out-of-plane vibrations with the required femto-Newton force sensitivity or nanometer-scale displacements, electrostatic actuation of the identical hybrid graphene/hBN membrane platform will be pursued as a reliable alternative. This well-established transduction method, extensively validated in suspended 2D nanomechanical resonators, leverages capacitive coupling via integrated electrodes to generate high force densities with precise voltage

control, independent of optical absorption or thermal-expansion properties. The device architecture can be readily adapted during CMOS-compatible fabrication while preserving the silicon-photonic strip waveguide geometry for evanescent-field readout, thereby maintaining full compatibility with the photonic interrogation scheme. This dual-pathway methodology safeguards timely achievement of the thesis objectives and also enables a rigorous comparative evaluation of thermal versus electrostatic actuation mechanisms, thereby strengthening the scientific contributions to ultra-sensitive on-chip hybrid 2D-material optomechanical sensors.

To systematically address the identified research question, Chapter 4 presents the experimental strategy and the guiding hypotheses that structured the work. The strategy centres on electrode-free optothermal actuation of a hybrid graphene/hBN membrane integrated with the silicon-photonic strip platform, cavity-enhanced readout near 1550 nm, and quantitative comparison of the observed mechanical response against the theoretical models developed later in the thesis.

Chapter 4

EXPERIMENTAL STRATEGY AND HYPOTHESES

The central research question addressed in this thesis is whether optothermal actuation, realised by a partially contacted multilayer graphene flake, can induce detectable out-of-plane vibrations in a suspended hexagonal boron nitride (hBN) membrane that is integrated with a silicon-photonic strip waveguide operating near 1550 nm. The associated sub-questions concern the quantitative influence of geometric and material parameters on the resulting actuation efficiency.

To answer these questions an experimental strategy was formulated that prioritises the electrode-free, CMOS-compatible optothermal pathway and exploits the existing high-tech silicon-photonic platform available at TU Delft. The strategy rests on three complementary pillars:

1. Fabrication of hybrid graphene/hBN membranes on the strip photonic platform by van-der-Waals dry transfer. This approach preserves the cavity-enhanced optical readout while introducing a localised optothermal actuator whose thickness, lateral extent and contact quality can, in principle, be varied.
2. Intensity-modulated laser excitation performed with an external acousto-optic modulator, at a wavelength locked to the flank of a photonic ring resonator. The same optical beam simultaneously provides photothermal drive (via absorption in the graphene) and interferometric readout of membrane displacement through the transmitted optical signal.
3. Quantitative extraction of the driven mechanical response by spectral analysis of the photoreceiver output, followed by comparison with the theoretical bimorph and membrane models developed in Chapter 5.

The principal hypotheses that guided device design, measurement protocols and data interpretation are the following:

- A partial multilayer graphene contact is sufficient to generate measurable thermoelastic forces and coherent out-of-plane displacement when the absorbed optical power is modulated near the membrane resonance frequency.
- Actuation efficiency η (expressed, for example, as excess spectral height above the Brownian background or as equivalent displacement per milliwatt) increases with graphene thickness up to the optical penetration depth at 1550 nm, and depends non-monotonically on hBN thickness through the competing effects of bending stiffness, thermal mass and thermal time constant.
- Larger graphene–hBN contact area improves both thermal and mechanical coupling, thereby raising the coherent drive amplitude relative to the thermomechanical noise floor.
- Residual air-gap height influences the optical intensity distribution at the membrane and the effective stiffness; once the membrane is fully released its effect is secondary compared with the contact and thickness parameters.

In practice, fabrication yield limited the experimental campaign to a small number of successfully transferred and optically functional devices. Systematic multi-parameter sweeps of graphene thickness, hBN thickness, contact area and air-gap height were therefore not realised. Instead, the work concentrated on demonstrating

and quantifying the optothermal response on the best-performing devices under controlled intensity-modulation conditions . The resulting data set, although restricted, is sufficient to test the primary hypothesis that a partial graphene contact can produce a detectable coherent mechanical signal and to identify the dominant physical limitations (partial contact, thermal filtering at megahertz frequencies, and modest absorbed power) that govern actuation efficiency in the present geometry.

Electrostatic actuation of the same hybrid membrane platform was considered at the planning stage as a contingency route. Because coherent optothermal signals were already obtained, this secondary pathway was not activated. The experimental campaign therefore remained fully electrode-free and retained the compactness and CMOS compatibility that constitute the principal technological motivation of the work.

The strategy outlined above isolates the essential physics of graphene-mediated optothermal actuation within an integrated photonic environment while remaining fully compatible with the Precision and Microsystems Engineering experimental infrastructure. The concrete fabrication sequences, optical-bench configurations and signal-processing procedures that implement this strategy are detailed in the following chapters.

Chapter 5

THEORETICAL FRAMEWORK

To enable controlled on-chip excitation of the suspended hBN membrane in our optomechanical ultrasound sensor, we propose employing a partially transferred multilayer graphene flake as an optothermal actuator. In-plane laser illumination at 1550 nm primarily heats the graphene patch (due to its substantial absorption at this wavelength), while hBN remains largely transparent. The resulting temperature rise induces out-of-plane displacement of the hBN drum via two interrelated mechanisms: (i) direct heat dissipation from the graphene contact area into the hBN, and (ii) mechanical stress transfer through strong van der Waals (vdW) adhesion, manifesting as bimorph-like actuation driven by differential thermal strains. These processes are tightly coupled owing to rapid interlayer thermal diffusion in vdW heterostructures. Even for the multilayer thicknesses targeted in this work (graphene and hBN each 5–70 nm), interlayer thermal equilibration remains fast (picosecond scale) [42, 62].

The analytical model is primarily employed to interpret the experimental observations and identify the dominant physical mechanisms governing optothermal actuation. Experimental results of and proof of concept constitute the goal of this thesis. On the other hand, understanding the quantitative modelling of the excitation and prediction of vibration amplitudes is important for interpreting the measurements. Consequently, to do so, it is instructive to first analyse each physical contribution in isolation: the direct thermal loading of the hBN drum and the mechanical stress transfer via van der Waals adhesion. This is a standard approach performed in thermomechanical analysis of multilayer systems before synthesising the fully coupled response. The following sections examine these mechanisms based on established theory for ultrathin 2D materials and suspended membranes.

5.1 Mechanisms of Optothermal Actuation

5.1.1 Effect of Direct Thermal Loading on a Homogeneous Multilayer hBN Drum

Hexagonal boron nitride (hBN) exhibits a negative in-plane coefficient of thermal expansion (CTE) at room temperature, with values typically ranging from $\alpha_{\mathrm{hBN}} \approx -2 \times 10^{-6}$ to -5×10^{-6} K^{-1} for multilayer flakes [35]. Under uniform temperature rise $\Delta T > 0$ in a clamped circular drum, this induces isotropic in-plane contraction. Fixed boundary conditions constrain the strain, generating additional uniform tensile stress per unit width [60]

$$N_{\mathrm{thermal}} = -\frac{Eh\alpha_{\mathrm{hBN}}\Delta T}{1-\nu}, \tag{5.1}$$

where $E \approx 870$ GPa [13], h is the membrane thickness (5–70 nm), and $\nu \approx 0.2$ is the Poisson's ratio. This augments the total in-plane tension per unit width $N_{\mathrm{total}} = N_0 + N_{\mathrm{thermal}}$, where N_0 is the initial (built-in) tension per unit width before heating. The increase in tension raises the effective mechanical stiffness and resonance frequency of the drum.

In classical plate and membrane theory, uniform heating of a homogeneous multilayer drum yields no first-order out-of-plane deflection for an initially flat geometry. The thermal moment through the thickness vanishes due to symmetry, and the static equilibrium equations provide no transverse driving term. Higher-order nonlinear effects (e.g., von Kármán coupling between in-plane strain and out-of-plane bending) are negligible at the femtometer-to-picometer out-of-plane displacements ($w \sim 10^{-15}$–10^{-12} m) relevant to the displacement sensitivity of the strip optomechanical readout [32]. Experimental investigations of suspended graphene and hBN membranes consistently demonstrate that uniform heating primarily tunes tension without inducing de novo

out-of-plane displacement [12, 16]. This parametric stiffness modulation via thermal-tension tuning has been quantitatively exploited in optomechanical characterization of suspended 2D membranes. Thus, direct thermal loading of the hBN drum alone contributes negligibly to directed actuation, resulting only in parametric stiffness modulation.

5.1.2 Effect of Isolated Mechanical Stress Transfer from Graphene Flake to hBN Drum

To isolate the purely mechanical contribution, we consider an idealised case in which the hBN drum is thermally inert ($\alpha_{\mathrm{hBN}} \approx 0$, $\Delta T_{\mathrm{hBN}} \approx 0$). Heating the multilayer graphene flake induces in-plane contraction governed by its negative coefficient of thermal expansion ($\alpha_g \approx -8 \times 10^{-6}$ to -3×10^{-6} K^{-1}, thickness-dependent [34]). Strong van der Waals adhesion efficiently transfers this compressive stress to the underlying hBN in the contact region, as demonstrated in analogous graphene-based bimorph systems [37, 38]. Because the drum edges remain clamped, the localised compression produces out-of-plane bulging of the central area for partial graphene coverage. While this limiting case clearly illustrates the mechanical stress-transfer mechanism, it overestimates the deflection by neglecting the counteracting thermal contraction of the hBN layer itself.

5.1.3 Coupled Bimorph Actuation in Graphene/hBN Heterostructure

In practice, rapid interlayer heat transfer (picosecond timescale) equilibrates temperature across the contacted stack, such that $\Delta T_g \approx \Delta T_{\mathrm{hBN}} \approx \Delta T$ [42, 62]. The resulting differential thermal strain $\epsilon_{\mathrm{diff}} = (\alpha_g - \alpha_{\mathrm{hBN}})\Delta T = \Delta\alpha\,\Delta T$ (typically -4×10^{-6} to -1×10^{-6} K^{-1}) drives bimorph-like curvature in the heterostructure region. Because the graphene layer (on top) contracts more than the underlying hBN, the contacted region bends downward (toward the substrate).

Analytical thin-plate bimorph models (based on the classic Timoshenko derivation [39]) predict that the deflection when the graphene patch is placed centrally on the drum takes the quantitative form

$$w_{\max} \approx \frac{3}{2} \frac{|\Delta\alpha|\,\Delta T\, h_{\mathrm{g}} h_{\mathrm{hBN}}}{(h_{\mathrm{g}} + h_{\mathrm{hBN}})^3} \cdot \frac{a_{\mathrm{patch}}^4}{a^2} \cdot f(\text{geometry}, N_0). \tag{5.2}$$

where a is the drum radius (10 μm for the reference device) and a_{patch} is the effective radius of the partially contacted graphene patch. The factor $h_g h_{\mathrm{hBN}}$ in the numerator arises from the thermal moment generated between the two layers in the classic Timoshenko bimorph derivation [39], while the cubic denominator accounts for the total thickness cubed (bending stiffness) and the global membrane tension over the full drum radius. The numerical prefactor 3/2 is a purely geometric coefficient that appears when the thermally induced curvature is integrated over a circular patch subject to clamped outer boundary conditions; its origin is derived in full in the following subsection. The correction function $f(\text{geometry}, N_0) \leq 1$ accounts for residual membrane tension and for the off-centre placement used in the actual devices.

The complete derivation of this scaling relation, together with a thorough discussion of every assumption, its physical justification, validity range and experimental implications, is presented in the following dedicated derivation subsection. In our device, however, the graphene flake is deliberately transferred off-center, near the drum edge and away from the strip waveguide. This placement is chosen to minimise optical absorption losses in the sensing region, but it alters the actuation mechanics.

For an eccentric (edge-located) patch the deflection amplitude is smaller than the central-patch prediction because:

- part of the graphene flake lies close to the clamped boundary, reducing the effective lever arm;
- the restoring force from the global membrane tension becomes asymmetric;
- the deflection profile is no longer radially symmetric, with the maximum displacement occurring near the inner edge of the flake rather than at the drum centre.

Consequently, the a_{patch}^4 dependence is no longer strictly valid; the actual dependence on patch size is weaker (closer to linear or quadratic). Nevertheless, the qualitative trends remain unchanged: larger contact area, thicker graphene, and higher laser power still increase the out-of-plane displacement, while the coupled bimorph mechanism dominates over pure thermal loading or pure mechanical stress transfer. Analogous bimorph actuation has been reported in graphene-based and vdW heterostructures [37, 38].

5.1.4 Derivation of the Bimorph Deflection Scaling Relation

The central-deflection scaling relation used in Eq.5.2 (and its quantitative version in Eq. (5.3) is an adaptation of the classic Timoshenko bimorph theory [39] to the specific geometry of a clamped circular drum with a partially overlapping central graphene patch. The derivation combines the thermal moment generated by the bilayer region with the bending stiffness of the heterostructure and the global membrane tension (or plate stiffness) of the full drum.

The geometry consists of a clamped circular drum of radius a (typically $a \approx 10\,\mu$m for the reference device). The graphene patch is modelled as a central circular region of effective radius a_{patch}. In polar coordinates centred at the drum centre, the radial coordinate r runs from $r = 0$ (geometric centre) to $r = a$ (clamped edge). The patch therefore occupies the inner disk $0 \le r \le a_{\text{patch}}$, while the outer region is the annulus $a_{\text{patch}} < r \le a$ consisting of pure hBN (no graphene on top). The out-of-plane deflection is written as a function $w(r)$. The final scaling expressions are evaluated at the centre ($r = 0$).

Starting Point: Timoshenko Bimorph Theory for a Cantilever Beam (1925) We consider first a simple bilayer cantilever beam of total thickness $h = h_g + h_{\text{hBN}}$, width b, and equal Young's moduli E (the scaling remains identical for modest modulus mismatch). A uniform temperature change ΔT produces a differential thermal strain $\varepsilon_{\text{diff}} = |\Delta\alpha|\,\Delta T$, where $\Delta\alpha = \alpha_g - \alpha_{\text{hBN}}$. Because the layers are bonded by strong van der Waals adhesion, this mismatch cannot be accommodated by free expansion; instead, it generates equal-and-opposite axial forces that form a couple (thermal moment per unit width)

$$M_T \propto E\, h_g h_{\text{hBN}}\, |\Delta\alpha|\, \Delta T.$$

The exact prefactor contains a rational function of the thickness and modulus ratios; only the scaling $M_T \sim E h_g h_{\text{hBN}} |\Delta\alpha| \Delta T$ is required here. Physically, the two layers want to expand differently upon heating but are bonded, so internal stresses create a couple.

The beam resists this moment through its bending stiffness per unit width

$$D \propto E(h_g + h_{\text{hBN}})^3.$$

In the Euler–Bernoulli limit the resulting curvature is therefore

$$\kappa = \frac{M_T}{D} \propto \frac{|\Delta\alpha|\,\Delta T\, h_g h_{\text{hBN}}}{(h_g + h_{\text{hBN}})^3}.$$

For a cantilever of length L with built-in end, integration of the curvature (small-slope approximation) yields a tip deflection

$$\delta \propto \kappa L^2 \propto \frac{|\Delta\alpha|\,\Delta T\, h_g h_{\text{hBN}}}{(h_g + h_{\text{hBN}})^3} L^2.$$

This is the classic Timoshenko bimetal result. The $h_g h_{\text{hBN}}$ numerator reflects the lever arm of the thermal force couple; the cubic denominator reflects the rapid stiffening with total thickness.

Adaptation to a Clamped Circular Drum with Central Graphene Patch The actual device is a clamped circular plate/membrane rather than a cantilever. Three geometric adaptations are required:

1. The thermal moment M_T is generated only inside the graphene-covered patch ($r \le a_{\text{patch}}$).
2. The local bending stiffness of the heterostructure patch is $D \propto (h_g + h_{\text{hBN}})^3$.
3. For small deflections the central deflection behaves approximately like a plate subjected to a localised moment, while the outer annular region and clamped boundary provide a global restoring force dominated by membrane tension, scaling as $1/a^2$.

Combining local plate-like deflection with global membrane restoring yields the scaling of Eq. 5.2.

Quantitative Form and Origin of the Geometric Prefactor 3/2 To obtain a quantitative expression, the local thermal curvature must be integrated over the circular patch while satisfying the clamped boundary conditions at the drum edge.

Inside the graphene-covered region the thermal moment produces a uniform particular curvature

$$\kappa_T = \frac{M_T}{D(1+\nu)}.$$

Outside the patch the thermal moment vanishes. The deflection therefore satisfies the homogeneous biharmonic equation $\nabla^4 w = 0$ in both the inner disk and the outer annulus, with a particular solution added only in the inner region.

The general axisymmetric solutions are [39]

$$w_{\text{in}}(r) = A_1 + B_1 r^2 + C_1 r^2 \ln r + D_1 \ln r + w_{\text{particular}}(r),$$
$$w_{\text{out}}(r) = A_2 + B_2 r^2 + C_2 r^2 \ln r + D_2 \ln r.$$

Regularity at the origin eliminates the singular terms ($C_1 = D_1 = 0$). The remaining six constants are fixed by the clamped conditions at $r = a$ ($w = dw/dr = 0$) together with continuity of deflection, slope, radial moment M_r and transverse shear at the interface $r = a_{\text{patch}}$.

When the resulting central deflection is evaluated in the tension-free limit and higher-order terms in $(a_{\text{patch}}/a)^2$ are neglected (valid for the moderate patch sizes used in the reference devices), under these idealised assumptions, the leading-order solution gives

$$w(0) = \frac{3}{2} \frac{M_T \, a_{\text{patch}}^4}{D \, a^2}.$$

The numerical prefactor 3/2 is therefore a pure geometric coefficient that arises from integrating a centrally localised thermal moment under clamped outer boundary conditions. Substituting the scaling $M_T \propto E h_g h_{\text{hBN}} |\Delta\alpha| \Delta T$ and $D \propto E(h_g + h_{\text{hBN}})^3$ recovers the quantitative bimorph expression

$$w_{\max} \approx \frac{3}{2} \frac{|\Delta\alpha| \, \Delta T \, h_{\text{g}} h_{\text{hBN}}}{(h_{\text{g}} + h_{\text{hBN}})^3} \cdot \frac{a_{\text{patch}}^4}{a^2} \cdot f(\text{geometry}, N_0). \tag{5.3}$$

The factor 3/2 derived above is exact only for the idealised case of a perfectly central circular patch on a tension-free clamped plate. In the real devices two important deviations from this idealisation are present:

- **Residual membrane tension** N_0. The suspended hBN membranes fabricated in this work carry a built-in tensile stress. The corresponding membrane restoring force $-N_0 \nabla^2 w$ increases the effective stiffness of the drum and therefore reduces the out-of-plane deflection relative to the pure bending (tension-free) solution.
- **Off-centre placement of the graphene flake**. In the experimental devices the graphene patch is deliberately transferred near the edge of the drum (away from the strip waveguide) in order to minimise optical absorption losses. Because the thermal moment is no longer applied symmetrically with respect to the geometric centre, the effective lever arm is reduced and the deflection profile becomes asymmetric. Both effects lower the centre deflection compared with the ideal central-patch prediction.

These two non-idealities are collected into a single dimensionless correction function $f(\text{geometry}, N_0) \leq 1$ that multiplies the ideal central-patch result. In the present analytic model f is left as a phenomenological factor; its precise value for a given device geometry and residual tension can be obtained by finite-element simulation or by direct experimental calibration.

Assumptions, Physical Justifications, and Experimental Implications The scaling form and the quantitative form rest on the following assumptions. Each assumption is stated, physically justified with the relevant mathematics, its validity range is given quantitatively, and direct experimental implications for future work are listed. These assumptions are deliberately written so that targeted parameter sweeps can be designed to test their limits or relax them in more advanced models.

1. **Small deflections** ($w_{\max} \ll h_{\text{hBN}}$). The entire derivation uses the linear Kirchhoff–Love plate equation. When deflections become comparable to the membrane thickness, von Kármán nonlinear stretching terms appear.

   Validity: For the expected range $w_{\max} \sim 0.1$–20 nm and $h_{\text{hBN}} = 5$–70 nm this is comfortably satisfied. **Experimental test / future work**: Devices with deliberately higher absorbed power until $w_{\max}$ approaches h_{hBN} are fabricated. Measured resonance shifts with the linear prediction should be compared; deviations signal the onset of geometric nonlinearity.

2. **Uniform temperature across the contacted stack** ($\Delta T_g \approx \Delta T_{\text{hBN}}$). Interlayer thermal diffusion in vdW heterostructures occurs on the picosecond timescale.

   Validity: Excellent for all multilayer thicknesses used here.

Experimental implication: Remains valid even if thicknesses are increased; for stacks >200 nm a 1-D through-thickness heat diffusion model may be needed. This will not be the case in the fabricated sample.

3. **Strong and uniform van der Waals adhesion**. Stress is fully transferred; no slippage.

   Validity: Standard for clean dry-transferred heterostructures.

   Experimental test: Raman mapping or AFM force-volume across the overlap. Controlled contamination experiments can quantify the effect of reduced adhesion on effective M_T.

4. **Negligible bending rigidity of the outer pure-hBN annulus** (the region $a_{\text{patch}} < r \leq a$). The flexural rigidity of the annulus scales as

   $$D_{\text{annulus}} \propto E\, h_{\text{hBN}}^3,$$

   while inside the patch it becomes

   $$D_{\text{patch}} \propto E(h_g + h_{\text{hBN}})^3.$$

   When $h_g \gtrsim 0.5\, h_{\text{hBN}}$, we have $D_{\text{patch}} \gtrsim 8\, D_{\text{annulus}}$. The outer region is therefore mechanically much more compliant. Because the driving thermal moment M_T exists only inside the patch, the curvature is generated locally by the stiff bimorph; the floppy outer annulus simply follows. Its own bending energy contribution is negligible.

   Validity range: Holds well for $h_g/h_{\text{hBN}} \gtrsim 0.5$. Questionable only when $h_g \ll h_{\text{hBN}}$.

   Experimental implications: Fabricated samples should be done such as $h_g/h_{\text{hBN}} \gtrsim 0.5$.

5. **Restoring force dominated by membrane tension or global plate stiffness rather than local bending of the thin annulus**. Three possible restoring mechanisms exist: local bending stiffness ($D\nabla^4 w$), global plate bending stiffness (clamped edge at $r = a$), and membrane tension N_0 ($-N_0\nabla^2 w$). Mechanism (1) localised to the outer annulus is negligible because D_{annulus} is small. The thermal moment M_T is balanced primarily by work against global tension N_0 (producing the $1/a^2$ factor) or by overall curvature satisfying the clamped boundary. The "lever arm" is the global drum radius a.

   Validity: Excellent whenever tension N_0 is appreciable.

   Experimental implications: N_0 should be independently measured and varied; $w_{\max}$ is to be checked whether it scales as $1/N_0$. For low-tension devices test by fabricating different radii a while keeping a_{patch}/a constant. Future models can solve $D\nabla^4 w - N_0\nabla^2 w = q_{\text{eff}}(M_T)$ numerically.

6. **The patch is treated as central for the analytical solution (off-centre placement absorbed in $f(\textbf{geometry}, N_0)$)**. The exact 3/2 was derived for a perfectly central patch. Real devices use off-centre placement, reducing the effective lever arm.

   Validity: The correction $f < 1$ is expected.

   Experimental / modelling implication: For quantitative prediction of a specific device FEM with the exact measured flake position is eventually needed. The analytic scaling remains excellent for trend prediction.

All assumptions are consistent with the device parameters targeted in this thesis and are standard in the 2D-material NEMS literature.

Relation to the Dynamic Resonant Response When the actuation laser is modulated at the mechanical resonance frequency f_0, only the AC component of the temperature oscillation contributes to periodic driving. The static bimorph deflection derived above is therefore multiplied by the mechanical quality factor Q_m while being attenuated by the first-order thermal low-pass filter of time constant $\tau = C/G_{\text{eff}}$:

$$w_{\text{dynamic}} \approx w_{\text{static,eff}} \cdot Q_m \cdot \frac{1}{\sqrt{1 + (2\pi f_0 \tau)^2}}. \tag{5.4}$$

For the relevant parameters ($\tau \approx 0.8$–$3\,\mu$s, $f_0 = 5$–15 MHz) the thermal attenuation lies between 0.3 % and 4 %. Resonant amplitudes nevertheless remain detectable given the strip displacement sensitivity (0.8–1.2 pm nm^{-1}) and typical $Q_m \sim 100$–1000 in fluid. The static model therefore supplies a conservative upper bound; actual resonant performance is quantified experimentally through systematic parameter sweeps.

5.2 Theoretical Modelling of Optothermal Actuation

Building upon the preceding analysis of the static bimorph mechanisms (Section 5.1), we now assemble a complete theoretical framework for optothermal actuation in the *reference device* (20 μm diameter circular hBN membrane, $k_{\text{eff}} \approx 10$–$50$ N m^{-1}, $f_0 \approx 5$–15 MHz). The model follows the physical chain from optical absorption to the final dynamic deflection that is detected by the photonic readout.

5.2.1 Optical absorption and steady-state temperature rise

Multilayer graphene exhibits absorptivity $A \approx 10$–50% at 1550 nm, scaling with thickness before saturation. Absorption increases nearly linearly with the number of layers up to approximately 20–30 layers; beyond a thickness of roughly 70 nm, further increases in thickness yield diminishing returns because the optical penetration depth at 1550 nm is limited (light is strongly attenuated before reaching the deeper layers) [36]. Consequently, going significantly above 70 nm does not meaningfully increase the absorbed power, while it increases the bending stiffness of the graphene/hBN bimorph and adds unnecessary mass. Both effects reduce the out-of-plane deflection for a given temperature change and are therefore undesirable for maximising actuation efficiency.

The steady-state temperature rise under continuous illumination is

$$\Delta T \approx \frac{P_{\text{abs}}}{G_{\text{eff}}}, \tag{5.5}$$

where G_{eff} is the effective thermal conductance (in W K^{-1}) from the heated graphene patch to the surrounding heat sinks (substrate, waveguide edges, and air). For the reference device geometry, G_{eff} is dominated by the interfacial (graphene–hBN van der Waals contact) and radial (in-plane conduction within the graphene and hBN to the clamped drum edge) contributions. These contributions can be quantified experimentally using optomechanical methods demonstrated on suspended 2D heterostructures.

5.2.2 Conversion of temperature rise into mechanical deflection

The out-of-plane deflection is driven by the bimorph effect arising from the mismatch in thermal expansion coefficients between graphene and hBN ($\Delta\alpha = \alpha_g - \alpha_{\text{hBN}}$, typically -4×10^{-6} to -1×10^{-6} K^{-1}). Using the quantitative relation derived in Section 5.1, the approximate central deflection for a circular drum is

$$w_{\max} \approx \frac{3}{2} \frac{|\Delta\alpha|\, \Delta T\, h_{\text{g}} h_{\text{hBN}}}{(h_{\text{g}} + h_{\text{hBN}})^3} \cdot \frac{a_{\text{patch}}^4}{a^2} \cdot f(\text{geometry}, N_0), \tag{5.6}$$

where $a = 10$ μm is the drum radius and a_{patch} is the effective radius of the graphene patch. The factor $3/2$ originates from integrating the thermally induced curvature over the patch area under clamped boundary conditions. The correction function $f(\text{geometry}, N_0) \leq 1$ accounts for residual membrane tension and for the off-centre placement of the graphene flake.

Because $w_{\max} \propto a_{\text{patch}}^4 \propto A_{\text{overlap}}^2$, the deflection depends strongly on the graphene–hBN contact area. For realistic temperature rises of $\Delta T = 20$–100 K (corresponding to $P_{\text{inc}} < 10$ mW) and typical contact-area fractions of 10–50% ($a_{\text{patch}} \approx 3$–$7$ μm), the model predicts static deflections in the range $w_{\max} \approx 0.1$–20 nm (upper bound, central-patch case).

Using the reference optomechanical sensitivity $\mathrm{d}\lambda/\mathrm{d}g \approx 0.8$–$1.2$ pm nm^{-1}, the corresponding photonic resonance shift is

$$\Delta\lambda \approx (\mathrm{d}\lambda/\mathrm{d}g) \times w_{\max} \approx 0.8\text{–}60 \text{ pm}. \tag{5.7}$$

It should be noted that because the graphene patch is eccentric and the residual membrane tension is not independently measured, Eq. (5.6) should be interpreted as a scaling relation rather than a device-specific quantitative prediction.

5.2.3 Thermal low-pass filtering under intensity modulation

When the actuation laser is modulated at a frequency f, the absorbed power in the graphene patch takes the form

$$P_{\text{abs}}(t) = P_{\text{DC}}\big(1 + m\cos(2\pi f t)\big), \tag{5.8}$$

where m is the modulation depth. Only the oscillating (AC) component can produce a periodic thermal moment and therefore a coherent mechanical drive.

The temperature response of the graphene/hBN patch is governed by the lumped thermal energy balance

$$C\frac{dT}{dt} + G_{\text{eff}}(T - T_0) = P_{\text{abs}}(t), \tag{5.9}$$

where C is the heat capacity of the patch and G_{eff} is the effective thermal conductance to the substrate and anchors. This first-order lumped-element model is the standard approach used to describe photothermal and electrothermal actuation in suspended 2D material resonators [32].

Defining the thermal time constant $\tau = C/G_{\text{eff}}$, the oscillating temperature amplitude in the frequency domain is

$$\Delta T_{\text{AC}}(f) = \Delta T_{\text{DC}} \times \frac{1}{\sqrt{1 + (2\pi f \tau)^2}}, \tag{5.10}$$

where $\Delta T_{\text{DC}} = P_{\text{DC}}/G_{\text{eff}}$. At the mechanical resonance frequencies used in the experiment ($f_0 = 5$–15 MHz) and with the expected thermal time constants for the device thicknesses ($\tau \approx 0.8$–$3\,\mu$s), the attenuation factor lies between 0.3% and 4% (see Table 5.1).

Table 5.1: Thermal attenuation of the oscillating temperature component at the mechanical resonance frequencies of the hybrid graphene/hBN drums (5–70 nm thickness range).

Drive frequency	$\tau = 0.8\ \mu$**s**	$\tau = 1.5\ \mu$**s**	$\tau = 3\ \mu$**s**
5 MHz	4.0%	2.1%	1.1%
15 MHz	1.3%	0.71%	0.35%

Consequently, even if a DC temperature rise of several tens of kelvin would produce a static bimorph deflection of several nanometres, the actual oscillating temperature ΔT_{AC} (and therefore the coherent mechanical drive) is reduced by more than two orders of magnitude.

5.2.4 Dynamic deflection amplitude at mechanical resonance

When the laser is modulated at the mechanical resonance frequency, only the attenuated AC temperature component drives the resonator. The resulting dynamic deflection amplitude is

$$w_{\text{dynamic}} \approx w_{\text{static,eff}} \cdot Q_{\text{m}} \cdot \frac{1}{\sqrt{1 + (2\pi f_0 \tau)^2}}, \tag{5.11}$$

where Q_m is the mechanical quality factor of the resonator (typically of order 10^1–10^2 in air for the devices studied here) and $w_{\text{static,eff}}$ is the static deflection that would be produced by ΔT_{AC}.

The resulting vibration amplitudes are expected to lie in the picometre to low-nanometre range. Given the high displacement sensitivity of the strip photonic readout (0.8–1.2 pm nm^{-1}) and typical mechanical quality factors, these amplitudes remain within the detection limit of the high-precision optical setup available in the TU Delft laboratories. The static bimorph model therefore serves as an upper bound; the actual resonant performance is quantified experimentally through systematic parameter sweeps.

The complete step-by-step derivation of the frequency-domain temperature response from the lumped thermal ODE is given in Appendix B.

5.3 Actuation Efficiency

To enable a direct quantitative comparison with the electrostatic and electrothermal methods presented earlier, we define the actuation efficiency as the ratio of the achieved central displacement to the incident optical power:

$$\eta = \frac{w_{\text{max}}}{P_{\text{inc}}} \quad (\text{nm/mW}). \tag{5.12}$$

Using the reference-device parameters and the predicted deflection range $w_{\text{max}} \approx 0.1$–$20$ nm (upper bound), the actuation efficiency evaluates to

$$\eta \approx 0.01\text{–}2\ \text{nm/mW} \tag{5.13}$$

(recognising that the real resonant efficiency will be lower by the thermal attenuation factor in Table 5.1). This figure of merit will be extracted directly from the planned experimental parameter sweeps of contact area, graphene thickness, and air-gap height.

5.4 Predicted Parametric Trends

The refined theoretical framework presented above yields several clear, testable predictions for the optothermal actuation performance of the graphene/hBN heterostructure. These trends will be directly probed through systematic experimental parameter sweeps (laser power, graphene thickness, hBN thickness, contact area, and air-gap height) and serve as benchmarks for validating the model against measured displacement amplitudes and resonance shifts.

The expected relationships are as follows:

- **Laser power:** Increasing the incident laser power P_{inc} leads to higher absorbed power and thus a larger steady-state temperature rise ΔT. Consequently, both the bimorph deflection $w_{\max}$ and the resulting photonic resonance shift $\Delta\lambda$ increase linearly with P_{inc} in the low-power regime ($P_{\text{inc}} < 10$ mW).
- **Graphene thickness:** Thicker multilayer graphene flakes increase the optical absorptivity A at 1550 nm (up to saturation around 50–70 nm), yielding a higher photothermal heating efficiency for a given P_{inc}. Beyond this thickness, further increases provide diminishing returns due to absorption saturation. Additionally, thicker graphene enhances the thermal moment in the bimorph, further increasing $w_{\max}$.
- **hBN thickness:** Increasing the hBN membrane thickness raises the overall bending stiffness of the heterostructure (scaling as $(h_g + h_{\text{hBN}})^3$), which tends to reduce the central deflection $w_{\max}$ for a given temperature rise. This creates a trade-off between mechanical robustness and actuation amplitude.
- **Contact area:** A larger graphene–hBN overlap area improves both interfacial heat transfer (larger effective G_{eff}) and mechanical stress transfer through vdW adhesion. Since $w_{\max} \propto a_{\text{patch}}^4$, the central deflection is expected to exhibit a strong (approximately quadratic) dependence on the contact area fraction.
- **Air-gap height:** Reducing the air gap between the hBN membrane and the strip waveguide increases the optomechanical sensitivity $\mathrm{d}\lambda/\mathrm{d}g$. This directly amplifies the measurable resonance shift $\Delta\lambda$ for any given out-of-plane displacement, thereby improving the overall detection limit of the actuation.
- **Residual pre-tension:** Higher built-in pre-tension N_0 (or tension induced by other means) increases the effective membrane stiffness, providing a negative feedback that reduces $w_{\max}$ for a given ΔT.

These predicted trends will guide the experimental design and enable quantitative comparison of optothermal actuation efficiency against the electrostatic and electrothermal schemes discussed earlier. The following chapter presents the experimental methodology developed to realise the graphene/hBN devices and to perform the systematic measurements that will test the validity of these predictions.

Chapter 6

EXPERIMENTAL METHODOLOGY

6.1 Device Fabrication and Heterostructure Transfer

The hybrid graphene/hBN optomechanical devices were fabricated by sequential dry transfer of mechanically exfoliated hexagonal boron nitride (hBN) and graphene flakes onto pre-fabricated silicon photonic chips containing strip ring resonators. Detailed photographs of the custom microscope-based transfer apparatus and procedure are provided in Annex C.

Square stamps of polydimethylsiloxane (PDMS) (see Appendix C.1 Figure 4), with lateral dimensions of approximately 3×3 to 5×5 mm^2, were prepared on glass slides and thoroughly cleaned using adhesive tape to remove surface contaminants. hBN flakes were exfoliated onto a commercial tape. A cleaned square PDMS stamp was then pressed firmly onto the hBN tape and rapidly released, resulting in the transfer of hBN flakes onto the PDMS surface. The flakes were inspected under an optical microscope, and their approximate thickness was assessed based on optical contrast, with thicker flakes appearing brighter due to higher reflectivity.

Suitable hBN flakes were subsequently picked up using a dome-shaped PDMS stamp (see Appendix C.1 Figure 4) that had also been cleaned with adhesive tape. Under the microscope, the dome stamp was manually lowered until it made contact with the target hBN flake on the square PDMS stamp. The stamp was then retracted, and this pick-up procedure was repeated until the desired flake adhered to the dome.

For transfer onto the photonic chip, the square PDMS stamp was removed from the setup. The pre-fabricated silicon photonic chip containing the ring resonators was positioned under the microscope (see Appendix C.1 Figure 1). The dome stamp carrying the hBN flake was aligned above the target location on the ring resonator. The stamp was then manually lowered by hand until contact was established between the hBN flake and the chip surface. To improve adhesion and transfer yield, the chip was heated to approximately 70 °C during the contact step. After successful transfer of the hBN flake directly onto the ring resonator region, the dome stamp was retracted.

Graphene flakes were transferred using a similar dry-transfer process. Two device configurations were fabricated:

- **Partial graphene coverage:** The graphene flake was positioned to overlap the bus waveguide and part of the hBN membrane while deliberately avoiding coverage directly above the ring resonator. This configuration was selected to minimise optical absorption losses within the photonic cavity.
- **Full graphene coverage:** The graphene flake was transferred such that it completely covered the hBN membrane, including the region directly above the ring resonator.

An alternative approach was also explored in which graphene was first transferred onto the dome-shaped PDMS stamp, after which the same stamp was used to pick up an hBN flake, thereby forming the complete graphene/hBN heterostructure on the stamp prior to transfer onto the chip. While this method enables the formation of the heterostructure in a single transfer step, it presented several practical limitations. In some cases, the graphene flake adhered strongly to the hBN source and could not be reliably picked up together with the hBN. In other instances, the graphene layer was damaged during pick-up, with the overlapping region remaining attached to the source PDMS, resulting in an incomplete or defective heterostructure. Furthermore, this approach offered limited flexibility in controlling the final relative position and orientation of the graphene flake with respect to the hBN and the ring resonator, as the geometry was fixed once the graphene was placed on the hBN.

In contrast, the sequential transfer method (hBN followed by graphene) provided greater control over the final placement. After the hBN flake was positioned on the ring resonator, the chip could be rotated to optimise the orientation before transferring the graphene flake, allowing more precise alignment of the graphene with respect to both the hBN membrane and the photonic waveguide.

6.2 Optical Characterization Setup for Silicon Photonic Ring Resonators

The experimental setup is a fiber-coupled, wavelength-swept transmission measurement station designed for spectral characterization of integrated ring resonators fabricated on a silicon photonic chip. It enables precise extraction of key resonator parameters, including resonance wavelengths, free spectral range (FSR), quality factor (Q), and extinction ratio through controlled wavelength scanning in the C-band telecom window.

A schematic of the setup is shown in Figure 6.1. Detailed photographs of the apparatus are provided in Annex D.

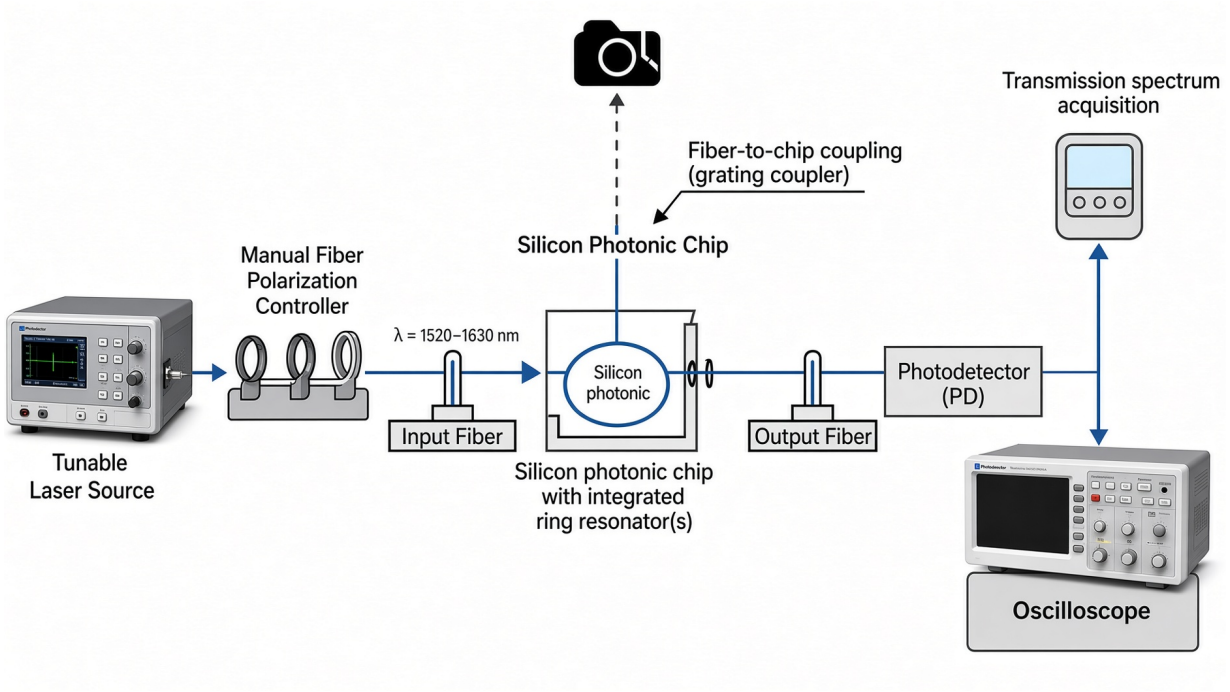


Figure 6.1: Simplified schematic of the fiber-coupled, wavelength-swept transmission measurement station for spectral characterization of silicon photonic ring resonators. Light from the tunable laser source passes through a manual polarization controller and is coupled into the silicon photonic chip via a lensed input fiber mounted on a nanopositioning stage. The output fiber is connected to the high-speed oscilloscope during spectrum acquisition. The optical power meter is used only temporarily during fiber alignment and is disconnected before measurements. A top-down CMOS camera assists real-time fiber-to-chip alignment.

6.2.1 Light Source and Polarization Control

A Keysight 81940A compact tunable laser source serves as the primary optical source. The laser provides mode-hop-free continuous tuning across 1520–1630 nm with picometre resolution, output powers up to +13 dBm, and wavelength accuracy of ±20 pm. The laser output is delivered via single-mode or polarization-maintaining fiber.

To ensure optimal coupling to the fundamental TE mode of the on-chip waveguides, the light passes through a manual fiber polarization controller (paddle-based design with multiple fiber loops) before reaching the input fiber. This controller enables precise adjustment of the input state of polarization by inducing controlled birefringence. Proper polarization alignment is essential for maximizing coupling efficiency and achieving high extinction ratios in the resonance spectra.

6.2.2 Photonic Chip and Fiber Alignment

The silicon photonic chip, fabricated on a silicon-on-insulator platform, contains input and output bus waveguides that are evanescently coupled to one or more ring resonators. Light is coupled into and out of the chip

using either separate lensed single-mode fibers or a 2-channel lensed fiber array, both mounted on high-precision multi-axis nanopositioning stages.

In the case of separate lensed fibers, the input fiber (post-polarization controller) is aligned to the input grating coupler or edge coupler, while the output fiber collects the transmitted light. When using a fiber array, both input and output coupling are achieved through a single mechanical connection, with one fiber of the array serving as the input and the second fiber serving as the output.

Fiber alignment is performed in two stages. First, the output path is temporarily connected to a Thorlabs PM100-series optical power meter to monitor and maximize the coupled optical power. Once sufficient coupling efficiency is achieved, the output is disconnected from the power meter and connected to the high-speed oscilloscope for spectrum acquisition. Throughout the alignment process, real-time visual feedback from the top-down CMOS camera is used to assist precise positioning of the fibers or fiber array relative to the chip.

6.2.3 Imaging and Alignment System

A Thorlabs Zelux CS165MU 1.6 MP monochrome CMOS camera, controlled via ThorCam software, provides top-down imaging of the fiber-to-chip interface. The live image assists fine alignment by visualizing scattered light at the coupling regions.

6.2.4 Detection and Readout

The detection configuration follows the practical measurement workflow:

- **Temporary output power monitoring (alignment only):** During fiber alignment, the output fiber is connected to a Thorlabs PM100-series digital optical power meter equipped with an S122C germanium photodiode sensor (700–1800 nm wavelength range) to monitor and optimize coupling efficiency.
- **High-speed acquisition (measurement phase):** For transmission spectrum measurements, the output fiber is connected exclusively to a Rohde & Schwarz RTA4004 4-channel digital oscilloscope (5 GSa/s sampling rate, 1 GHz bandwidth). The oscilloscope captures the transmitted optical signal while the laser wavelength is swept.

6.2.5 Auxiliary Equipment

A Newport 0901 ±15 V current-limited power supply powers active components on the chip. The complete setup is mounted on a vibration-isolated optical table (Newport Nexus) using Thorlabs mechanical components to ensure maximum mechanical stability.

6.2.6 Measurement Principle

Custom Python software controls the tunable laser and synchronously acquires the transmission spectrum. After fiber alignment is completed and the output fiber is connected to the oscilloscope, the software performs a continuous wavelength sweep across the resonance while recording the transmitted optical power from the oscilloscope. Resonances appear as Lorentzian-shaped dips (all-pass configuration) or peaks (add-drop configuration) in the transmission spectrum. This procedure enables automated extraction of critical device metrics such as resonance wavelength, quality factor, extinction ratio, and free spectral range.

6.3 Measurement Procedures for Spectral Characterization

The spectral characterization of the hybrid graphene/hBN optomechanical devices was performed using the fiber-coupled, wavelength-swept transmission measurement station described in Section 6.2. The procedure ensures reproducible fiber-to-chip coupling via the on-chip grating couplers while preserving laser safety, mechanical stability, and the integrity of the suspended membranes. All measurements were conducted at room temperature on a vibration-isolated optical table (Newport Nexus) under ambient laboratory conditions. Detailed photographs of the apparatus are provided in Annex D.

Prior to each measurement session, the input lensed fiber (mounted on a high-precision multi-axis nanopositioning stage) was confirmed to be securely connected to the output of the Keysight 81940A compact tunable laser source. The silicon photonic chip containing the strip ring resonators and suspended hybrid membranes was mounted on the sample stage.

A top-down imaging system consisting of a Thorlabs Zelux CS165MU 1.6 MP monochrome CMOS camera controlled by ThorCam software was activated. The camera position, focus, and illumination were adjusted to provide a clear, high-contrast view of the target grating couplers and the suspended membrane regions. Exposure time and gain were optimized to avoid saturation while enabling real-time visualization of the lensed fiber tips relative to the chip surface.

The tunable laser was enabled only after verification that the green interlock indicator confirmed all safety interlocks were satisfied. Throughout the measurement campaign the laser remained in the enabled state to maintain thermal stability of the source and fiber delivery system; deactivation was performed exclusively after all fibers had been safely retracted from the chip.

Fiber end-face quality was inspected using an optical fiber inspection scope. The output facet of the input lensed fiber was examined to confirm that the emerging optical mode appeared circular, well-defined, and free of significant scattering or irregularities.

Coarse fiber positioning was performed under continuous real-time camera observation. The input and output lensed fibers (or 2-channel lensed fiber array) were first translated laterally until both tips were visible in the camera field of view, while ensuring that their tips remained safely above the chip surface and did not contact any structures. The fibers were then positioned over regions free of critical devices. The vertical (z) axis of each nanopositioning stage was lowered until gentle contact with the chip surface was detected (observed via a slight change in the camera image or mechanical resistance). The fibers were subsequently retracted to establish a safe hover height above the chip surface. Lateral (x–y) translation was then used to align each fiber core precisely above the center of the respective input and output grating couplers.

Fine active alignment was achieved by temporarily connecting the output lensed fiber to a Thorlabs PM100-series digital optical power meter equipped with an S122C germanium photodiode sensor (wavelength range 700–1800 nm). With the Keysight 81940A laser operating at the design wavelength near 1550 nm (after passage through the manual paddle-based fiber polarization controller), the x- and y-positions of both the input and output fibers were iteratively adjusted on their nanopositioning stages while monitoring the transmitted optical power. Alignment was considered successful when the detected power reached the order of 20 µW, providing sufficient signal strength and signal-to-noise ratio for high-sensitivity resonance spectroscopy. This power level corresponds to adequate grating-coupler coupling efficiency for the ring-resonator circuit under test.

Once stable coupling was verified, the output fiber was disconnected from the power meter and reconnected exclusively to the Rohde & Schwarz RTA4004 4-channel digital oscilloscope. The oscilloscope was configured to the appropriate input channel with a time base of 100 ms and a zero-offset baseline. With the transmitted signal clearly visible, spectral acquisition was initiated by executing the custom Python software described in Section 6.2 . The software performed a continuous, mode-hop-free wavelength sweep of the Keysight 81940A laser across the resonance while synchronously recording the transmitted intensity from the oscilloscope. Resonances appeared as Lorentzian-shaped dips in the transmission spectrum. The resulting spectrum enabled automated extraction of resonance wavelength, quality factor, extinction ratio, and free spectral range, providing the calibrated photonic readout baseline for subsequent optothermal actuation experiments.

This standardized procedure, executed on the vibration-isolated setup of Section 6.2, guaranteed reproducible coupling conditions across multiple devices and measurement sessions while maintaining full compatibility with the electrode-free, electrode-free optothermal actuation scheme developed in this thesis.

While the wavelength-swept measurements provide the static optical baseline of the hybrid devices, the investigation of optothermal actuation requires a different experimental configuration. In this configuration the laser is locked to the flank of a resonance and intensity modulation is used to drive the membrane while the resulting motion is recorded in the frequency domain. The two configurations that were evaluated for this purpose are described in the following section.

6.4 Optothermal Actuation Measurement Configurations

Two complementary optical configurations were evaluated for simultaneous cavity-enhanced readout and optothermal actuation of the hybrid graphene/hBN membrane. Both exploit the same narrow-linewidth probe laser locked to the steep flank of a selected ring-resonator resonance, thereby converting membrane displacement into an intensity modulation that is recorded by a high-speed photodetector and analysed on a Moku:Lab spectrum analyser. The essential difference lies in the method used to impose the intensity modulation that drives the optothermal force.

6.4.1 Single-Laser Intensity-Modulated Actuation (Setup 1)

In the single-laser configuration the same optical beam serves both as the readout probe and as the intensity-modulated actuation source (Fig. 6.2).

Light from Laser 1 is first sent through an acousto-optic modulator (AOM). The AOM is driven by a radio-frequency (RF) carrier whose amplitude is modulated by an arbitrary waveform generator (AWG) at the target mechanical resonance frequency (typically 12–30 MHz). After the AOM the beam is fibre-coupled into the silicon

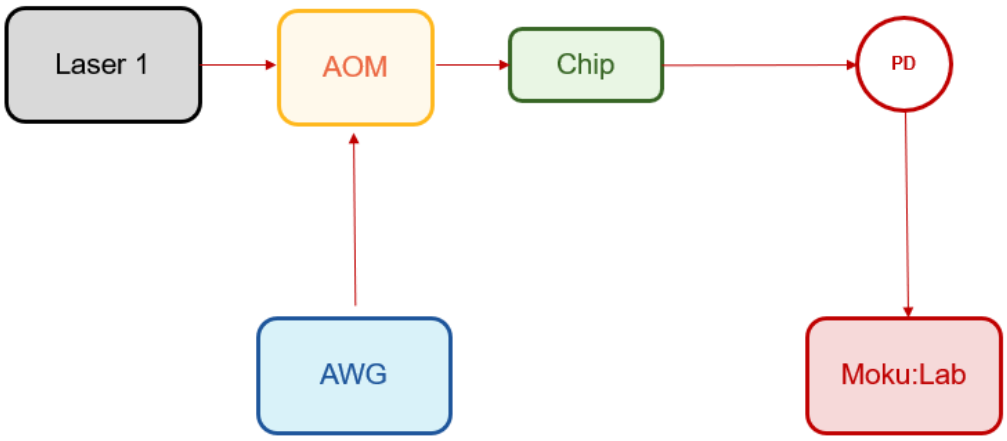


Figure 6.2: Single-laser intensity-modulated actuation and readout configuration (Setup 1). The continuous-wave laser is intensity-modulated by an acousto-optic modulator (AOM) driven by an arbitrary waveform generator (AWG) at the mechanical resonance frequency. The modulated light is coupled into the photonic chip; the transmitted signal is detected by a photodiode (PD) and analysed on the Moku:Lab spectrum analyser.

photonic chip. The laser wavelength is locked to the linear flank of a selected optical resonance so that any change in the membrane gap produces a proportional intensity variation at the photodetector. The photodetector output is digitised and spectrum-analysed by the Moku:Lab instrument, yielding both the Brownian noise floor and the coherent driven response.

Because a single optical path is used, alignment is simplified and the relative intensity noise of the laser appears identically on the drive and the readout, facilitating common-mode rejection. All quantitative results reported in Chapter 7 were acquired with this configuration.

6.4.2 Dual-Laser Actuation Attempt (Setup 2)

A dual-laser architecture was also implemented in an attempt to decouple the actuation and readout powers (Fig. 6.3).

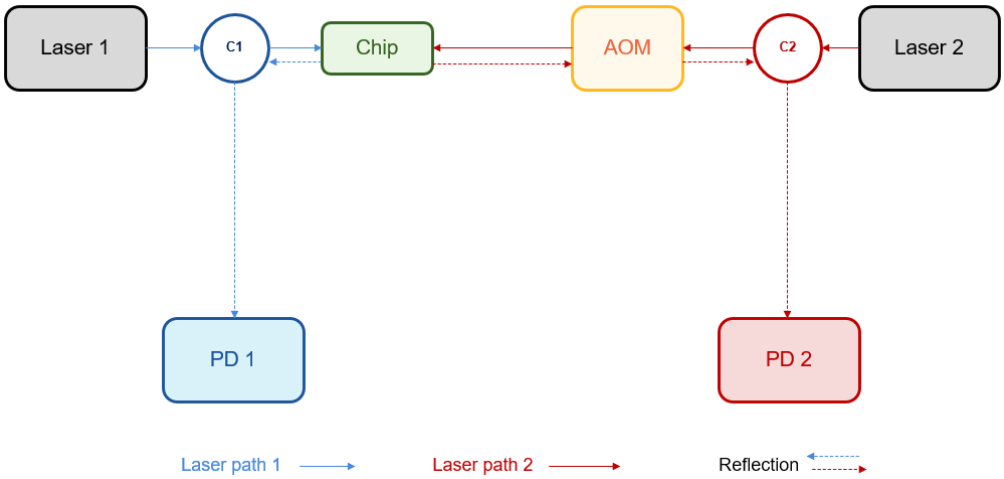


Figure 6.3: Dual-laser configuration (Setup 2). Laser 1 provides the cavity-enhanced readout while Laser 2, intensity-modulated by an independent AOM, supplies the optothermal drive. Optical circulators (C1, C2) separate forward and backward propagating light. In practice the second photodiode channel saturated under the combined optical power, rendering the configuration unusable for quantitative measurements.

Laser 1 was again locked to the resonance flank and routed through circulator C1 to the chip; the returning

light was detected on PD1. Laser 2 was intensity-modulated by a second AOM and coupled into the chip via circulator C2, providing an independent optothermal drive. In principle this arrangement allows the actuation power to be increased without saturating the readout photodiode.

In practice the dual-beam geometry produced optical powers at the photodetector that exceeded the linear range of the available photodiode, resulting in persistent saturation. Despite several attempts to attenuate the actuation arm and to improve isolation, a stable, unsaturated signal could not be obtained. Consequently the dual-laser configuration was abandoned and all subsequent measurements were performed exclusively with the single-laser Setup 1 described above.

6.4.3 Rationale for Adoption of Setup 1

The single-laser architecture offers three decisive practical advantages for the present devices:

1. simplified fibre-to-chip alignment (only one optical path),
2. inherent common-mode rejection of laser intensity noise,
3. absence of photodiode saturation under the optical powers required for detectable optothermal drive.

All spectra, driven-response curves and excess-noise measurements presented in Chapter 7 were therefore acquired with Setup 1.

6.4.4 Signal Conversion in the Moku:Lab Spectrum Analyzer

All spectral data presented in this thesis were acquired with the Moku:Lab Spectrum Analyzer. The instrument reports power spectral density in units of dBm. A clear understanding of the conversion from the measured voltage waveform to the reported dBm value is required for the quantitative analysis performed in Chapter 7.

The dBm scale is defined with respect to a reference power of 1 mW [69]:

$$P_{\mathrm{dBm}} = 10 \log_{10} \left(\frac{P}{1\,\mathrm{mW}} \right), \tag{6.1}$$

where P is the signal power expressed in watts.

The Moku:Lab converts the detected voltage to power using the selected input impedance R:

$$P = \frac{V_{\mathrm{rms}}^2}{R}. \tag{6.2}$$

In every measurement reported here the analog frontend was configured for a 50 Ω input impedance and a 1 Vpp full-scale range. Consequently $R = 50\,\Omega$.

For a pure sinusoidal tone the relationship between peak-to-peak voltage and root-mean-square voltage is

$$V_{\mathrm{rms}} = \frac{V_{\mathrm{pp}}}{2\sqrt{2}}. \tag{6.3}$$

Substitution yields the practical conversion formula used by the instrument [69]:

$$P = \frac{V_{\mathrm{pp}}^2}{8R} \qquad \Rightarrow \qquad P_{\mathrm{dBm}} = 10 \log_{10} \left(\frac{V_{\mathrm{pp}}^2}{8R \times 10^{-3}} \right). \tag{6.4}$$

As a reference check, a 1 Vpp sine wave terminated into 50 Ω produces

$$10 \log_{10} \left(\frac{1^2}{8 \times 50 \times 10^{-3}} \right) \approx 3.98\,\mathrm{dBm}, \tag{6.5}$$

which is reported as 4.0 dBm in the manufacturer documentation. This value is recovered experimentally when an instrument output is looped directly back to an input, confirming correct frontend calibration.

The inverse transformation, required when absolute voltage amplitudes are needed for later displacement calibration, is

$$V_{\mathrm{rms}} = \sqrt{R \cdot 10^{(P_{\mathrm{dBm}}/10)-3}}, \qquad V_{\mathrm{pp}} = 2\sqrt{2}\, V_{\mathrm{rms}}, \tag{6.6}$$

again with $R = 50\,\Omega$.

Relevance to the present experiment

Because the conversion of Equation (6.4) is frequency-independent for a pure sinusoid, any purely electrical feed-through of the 15 mVpp drive tone should appear as a coherent spike of constant height independent of the chosen drive frequency. The observation that both the absolute height of these spikes and the shape of the underlying Brownian peak vary systematically with drive frequency (12–30 MHz) therefore constitutes direct evidence of an optomechanical interaction: the driven motion of the hybrid membrane modulates the optical power reaching the photodetector.

When quoting absolute power levels in subsequent chapters, the frontend settings (50 Ω, 1 Vpp range, AC coupling) are always stated. If an absolute displacement calibration is required, the Brownian peak height is first converted from dBm to V_{rms} using the relations above and then scaled by the independently measured optomechanical responsivity of the strip ring resonator.

Chapter 7

MEASUREMENT ANALYSIS

7.1 Device and Measurement Overview

To evaluate the effect of integrating the hBN/graphene heterostructure onto the silicon photonic chip, transmission spectra of Sample 01 were recorded before and after the transfer process using a tunable laser. Sample 01 is used throughout this chapter as a representative device because it exhibits the complete range of optical responses expected following heterostructure integration. The objective of the measurements is to compare the resonance characteristics before and after transfer and investigate how the transferred two-dimensional materials influence the optical response of the ring resonators.

Figure 7.1 shows an optical micrograph of the device after the transfer process. The hBN and graphene flakes are visible on one of the ring resonators located within the central group, while the remaining resonators remain uncovered. Five ring resonators are positioned in the immediate vicinity of the transfer site, whereas the sixth resonator is located further away, as shown in Figure 7.2. This spatial arrangement provides useful context for interpreting the post-transfer optical measurements, since only a subset of the resonators was intentionally modified by the transferred heterostructure.

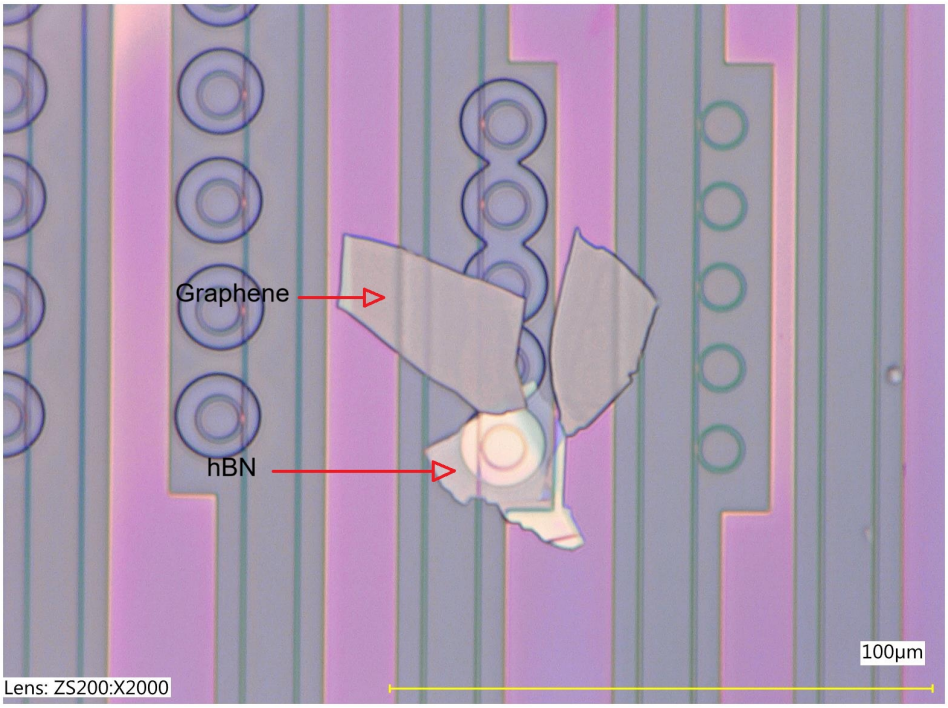


Figure 7.1: Zoomed-in optical micrograph of the photonic chip after transfer of the hBN/graphene heterostructure. The flakes are located on one ring resonator within the central column, while the remaining resonators remain uncovered.

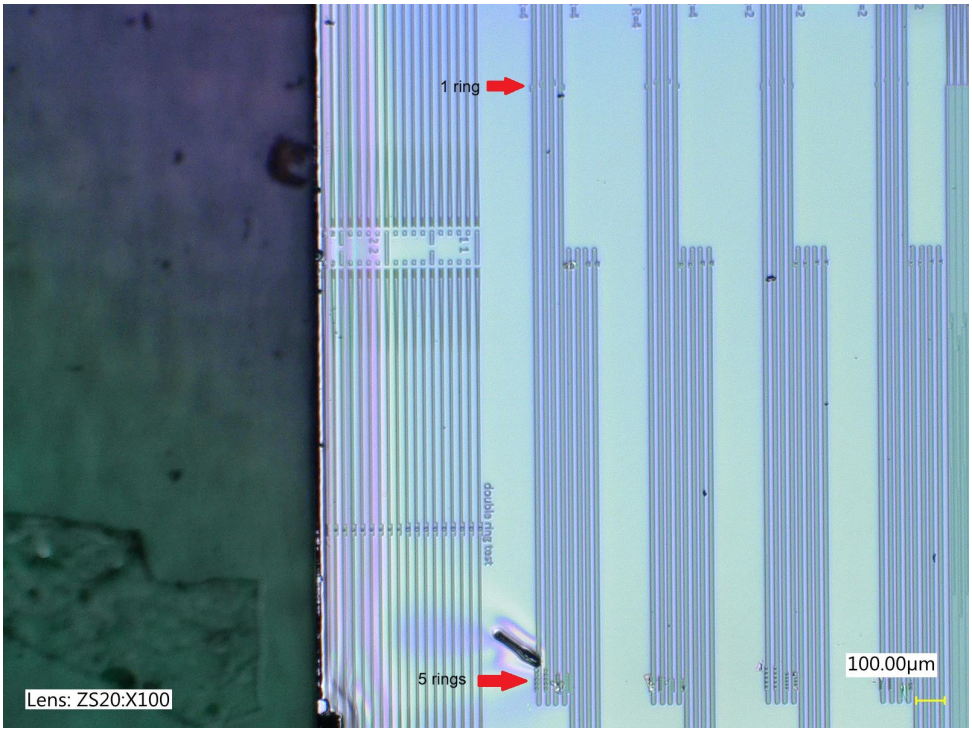


Figure 7.2: Zoomed-out optical micrograph of the photonic chip showing all six ring resonators and their relative positions with respect to the heterostructure transfer site.

7.2 Passive Optical Characterization

7.2.1 Theoretical Background: Resonance Condition and Free Spectral Range

Optical ring resonators support a series of resonant modes that satisfy the resonance condition

$$m\lambda_m = 2\pi R n_{\text{eff}}, \tag{7.1}$$

where m is the azimuthal mode number, R is the ring radius, and n_{eff} is the effective refractive index of the guided optical mode. Resonances occur whenever the optical path length of one round trip equals an integer multiple of the wavelength.

As a consequence, the resonances appear approximately periodically in wavelength. The spacing between two consecutive resonances is referred to as the free spectral range (FSR), which may be approximated by

$$\text{FSR} \approx \frac{\lambda^2}{2\pi R n_{\text{eff}}}, \tag{7.2}$$

for small wavelength intervals where the effective refractive index varies only weakly. Throughout this chapter, the periodicity of the resonance spectrum is exploited to identify the resonance associated with each individual ring resonator.

7.2.2 Pre-Transfer Transmission Spectrum and Ring Identification

The transmission spectrum recorded before heterostructure transfer is shown in Figure 7.3. Six well-defined resonance dips are observed within each free spectral range, and this pattern repeats periodically across the scanned wavelength range, consistent with the resonance condition described above.

To facilitate identification of the individual resonators, the same spectrum is shown in Figure 7.4, where four consecutive free spectral ranges (FSR 1–4) are indicated and the six resonance dips within each FSR are labelled according to their corresponding ring (R1–R6).

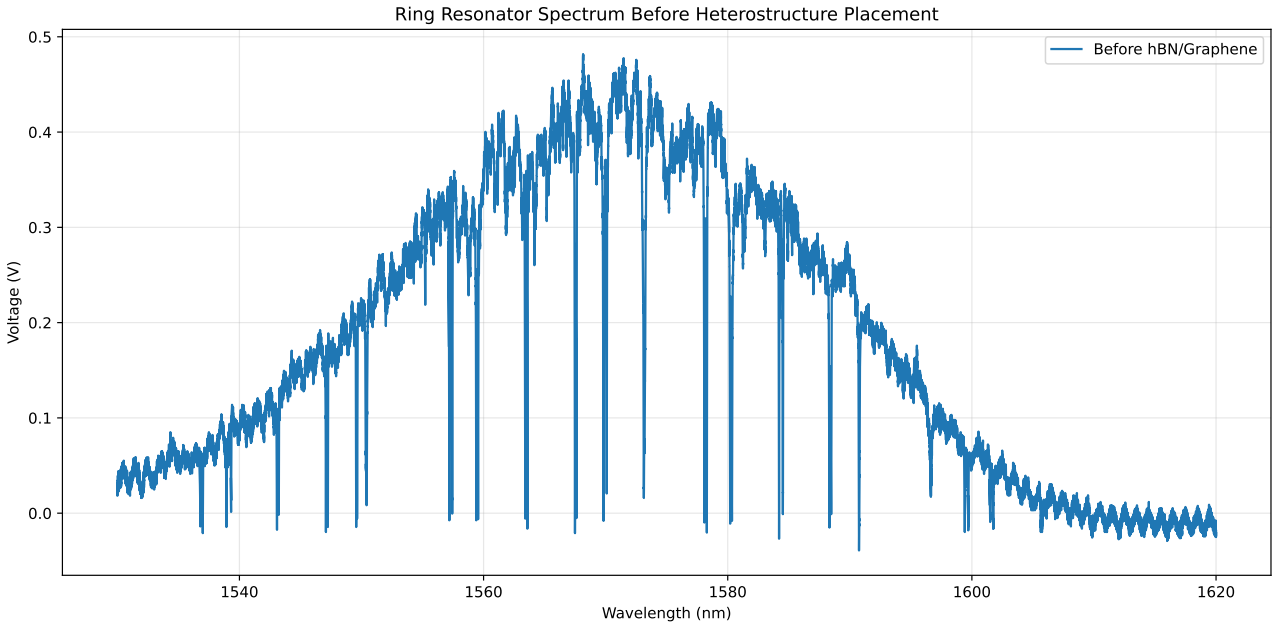


Figure 7.3: Raw transmission spectrum of the six ring resonators before hBN/graphene heterostructure transfer. The periodic repetition of the resonance features across successive free spectral ranges is clearly visible.

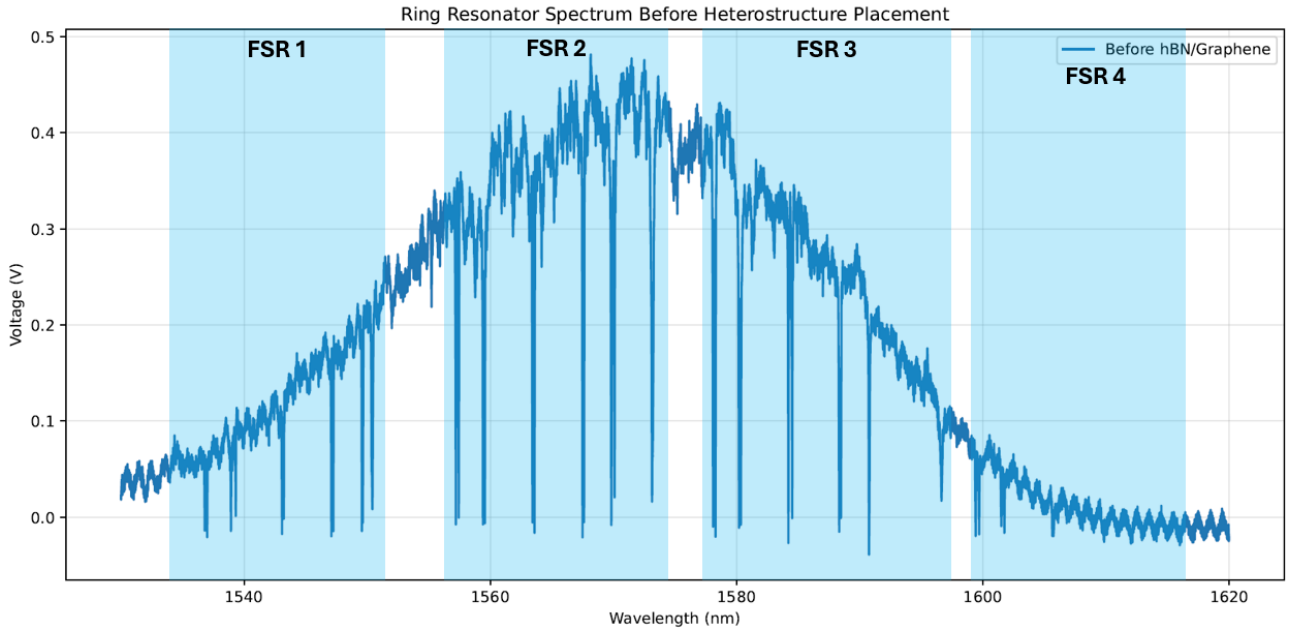


Figure 7.4: Transmission spectrum before heterostructure transfer. Four consecutive free spectral ranges are indicated, and the six resonance dips within each FSR are labelled according to their corresponding ring resonator. The intentional radius variation produces a systematic wavelength offset between neighbouring rings, enabling unambiguous resonance identification.

During device design, the radii of the six ring resonators were intentionally varied by small nominally equal increments. Since the resonance wavelength scales approximately with the ring radius ($\Delta\lambda/\lambda \approx \Delta R/R$), this radius stepping produces a corresponding offset in resonance wavelength between neighbouring rings. Consequently, each ring exhibits a distinct resonance position within every free spectral range, allowing the resonance dips to be consistently identified throughout the measured wavelength range.

The measured transmission spectrum exhibits six distinct resonances within each free spectral range (FSR). These resonances are labelled R1–R6 in order of increasing wavelength and are listed in Table 7.1 for three

consecutive FSRs.

Table 7.1: Resonance wavelengths extracted from the pre-transfer transmission spectrum together with the local inter-resonance spacings and the apparent FSR of each mode family.

Resonance	Wavelength (nm)	$(N+1)-N$ (nm)	Apparent FSR (nm)
FSR 1			
R1	1536.80	–	–
R2	1538.93	2.13	–
R3	1543.08	4.15	–
R4	1547.09	4.01	–
R5	1549.57	2.48	–
R6	1550.36	0.79	–
FSR 2			
R1	1557.20	6.84	20.40
R2	1559.40	2.20	20.47
R3	1563.42	4.02	20.34
R4	1567.49	4.07	20.40
R5	1569.83	2.34	20.26
R6	1573.13	3.30	22.77
FSR 3			
R1	1578.09	4.96	20.89
R2	1580.20	2.11	20.80
R3	1584.20	4.00	20.78
R4	1588.33	4.13	20.84
R5	1590.75	2.42	20.92
R6	1596.63	5.88	23.50

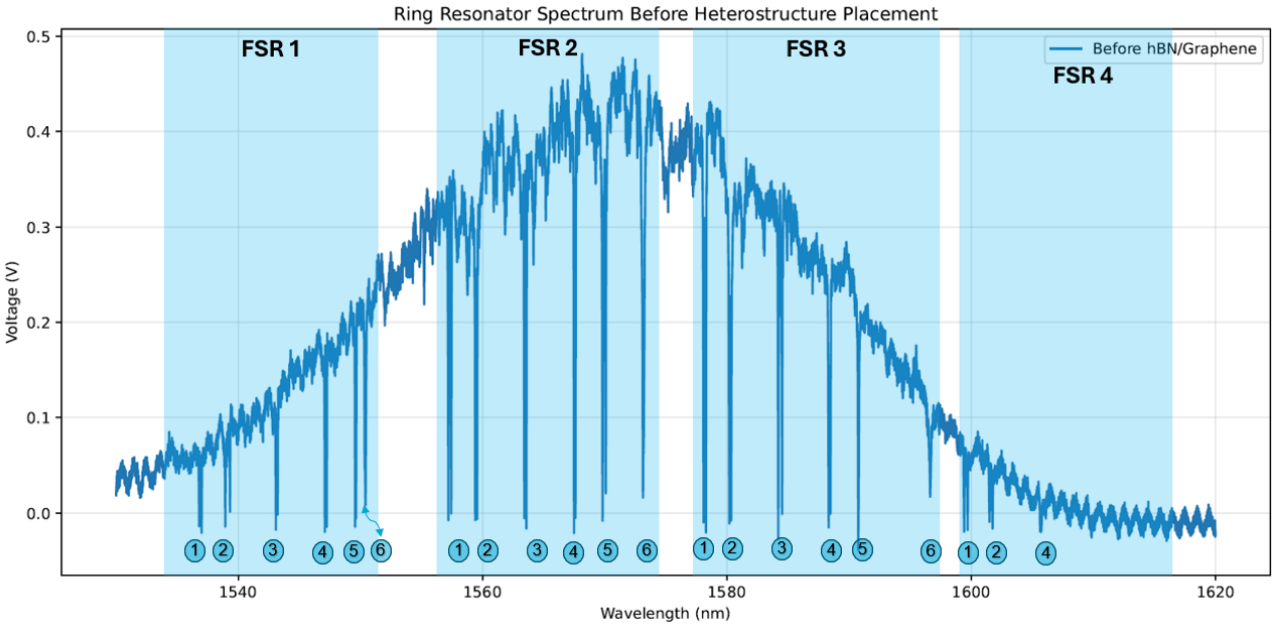


Figure 7.5: Pre-transfer transmission spectrum of the six-ring device with individual resonances labelled R1–R6 within each free spectral range. The progressive drift of Resonance 6 relative to the other five modes is clearly visible.

Inspection of the local spacings already reveals that the relative position of Resonance 6 is not constant across successive free spectral ranges. While the mutual separations among R1–R5 remain nearly invariant (apart from the small, systematic increase expected from the weak wavelength dependence of the group index), the distance between R5 and R6 increases markedly from 0.79 nm in FSR 1 to 3.30 nm in FSR 2 and 5.88 nm in FSR 3. This

progressive drift is the spectroscopic signature of a resonator whose free spectral range differs from that of the other five rings.

Because

$$\mathrm{FSR}(\lambda) \approx \frac{\lambda^2}{n_g(\lambda)\, 2\pi R}, \tag{7.3}$$

a ring of larger radius possesses a systematically smaller FSR. The discrete set of resonances belonging to each ring therefore constitutes a comb with its own tooth spacing. When two combs of unequal spacing are observed over an extended wavelength range, their relative alignment changes continuously: the comb belonging to the larger ring "walks" relative to the combs of the smaller rings. The observed increase in the R5–R6 separation is precisely this relative walk.

In the present device the six rings were designed with a small, intentional radius increment so that their resonances interleave without spectral overlap. One of the rings—commonly referred to as the reference ring—is given a deliberately larger radius offset. The resulting larger detuning guarantees that a clean, unperturbed resonance remains identifiable even after fabrication tolerances or environmental drifts, and it provides a local wavelength marker that is unaffected by the analyte or by the two-dimensional material. Resonance 6 exhibits exactly the spectroscopic behaviour expected of this reference ring: a distinctly different FSR and a correspondingly pronounced walk relative to the sensor rings.

7.2.3 Comparison of the Transmission Spectra Before and After Transfer

To investigate the optical response of the transferred heterostructure, the transmission spectra recorded before and after transfer were first compared directly. Figure 7.6 presents the measured spectra over the same wavelength range, allowing the resonance behaviour of each ring resonator to be examined before and after integration of the hBN/graphene heterostructure.

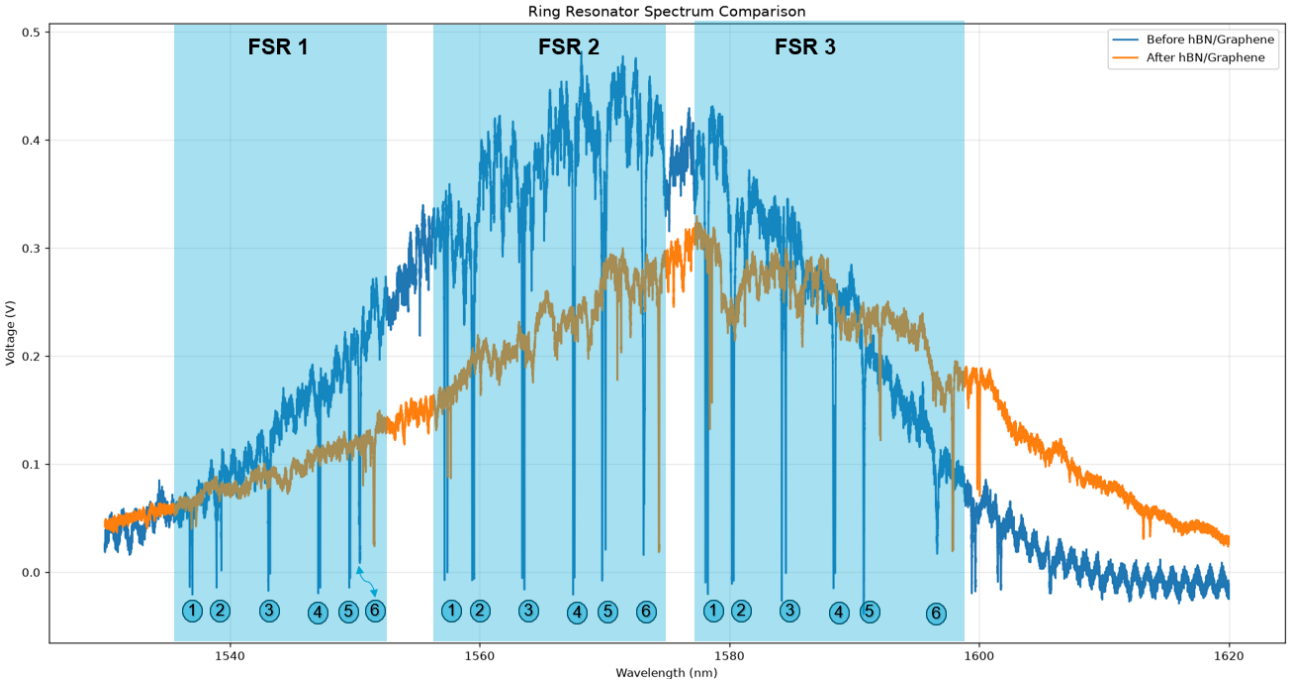


Figure 7.6: Measured transmission spectra of Sample 01 before (blue) and after (red) heterostructure transfer. The resonance positions corresponding to each ring are indicated using the assignments established in Section 7.1.

Several notable changes are immediately apparent following the transfer process. Prior to transfer, six well-defined resonance dips are observed within each free spectral range, corresponding to the six ring resonators on the chip. After transfer, only four resonances remain visible within the measured wavelength range. Two resonances disappear completely, while two remaining resonance exhibits a noticeably shallower transmission dip compared to the pre-transfer spectrum.

The disappearance of the R2 and R4 resonances is consistent with the presence of graphene on these resonators. Graphene exhibits appreciable optical absorption at telecommunications wavelengths, increasing the round-trip

loss within the cavity and suppressing the resonant interference responsible for the transmission dip. Consequently, the resonance contrast is reduced below the detection limit, resulting in the complete disappearance of these resonances from the measured spectrum. In contrast, Resonances R3 and R5 remain visible but exhibit a markedly reduced transmission dip, consistent with partial optical absorption introduced by graphene coverage that increases the round-trip loss while still permitting a detectable resonance.

A second, equally important observation concerns Resonance 6. In contrast to the other five resonances, the transmission dip associated with R6 shows essentially no change in depth or lineshape after the transfer. This invariance indicates that the corresponding ring was not covered by the hBN/graphene heterostructure. The ring in question is the reference resonator, which is deliberately placed at a substantial lateral distance from the five closely spaced sensor rings. Because of this spatial separation, the two-dimensional material stack does not overlap it during the deterministic transfer.

Designers routinely incorporate such a reference ring for several reasons. First, it provides a local wavelength marker whose resonance position is independent of any analyte or of the presence of the two-dimensional material. Second, it serves as an on-chip thermal reference: any global temperature drift of the chip produces a common-mode shift of all resonances, which can be subtracted by monitoring the reference ring. Third, the intentional radius offset that gives the reference ring a distinctly different free spectral range guarantees that its resonances remain spectroscopically distinguishable even after fabrication variations or environmental drifts.

Because Resonance 6 is demonstrably unaffected by the hBN/graphene transfer, it constitutes a reliable spectral anchor. The entire post-transfer spectrum can therefore be rigidly shifted by the measured displacement of this resonance,

$$\Delta\lambda = \lambda_{\mathrm{R6,\,after}} - \lambda_{\mathrm{R6,\,before}} = 1574.36\,\mathrm{nm} - 1573.13\,\mathrm{nm} \approx 1.23\,\mathrm{nm}, \tag{7.4}$$

so that the reference features of the two data sets coincide. Once the spectra are aligned in this manner, the differential shifts of the remaining resonances become directly comparable, allowing unambiguous identification of the ring that interacted with the heterostructure and quantitative extraction of the induced wavelength shift. After applying the rigid wavelength shift of $\Delta\lambda = 1.23\,\mathrm{nm}$ derived from Resonance 6, the two spectra can be compared on a common wavelength axis. The resulting aligned traces are shown in Figure 7.7.

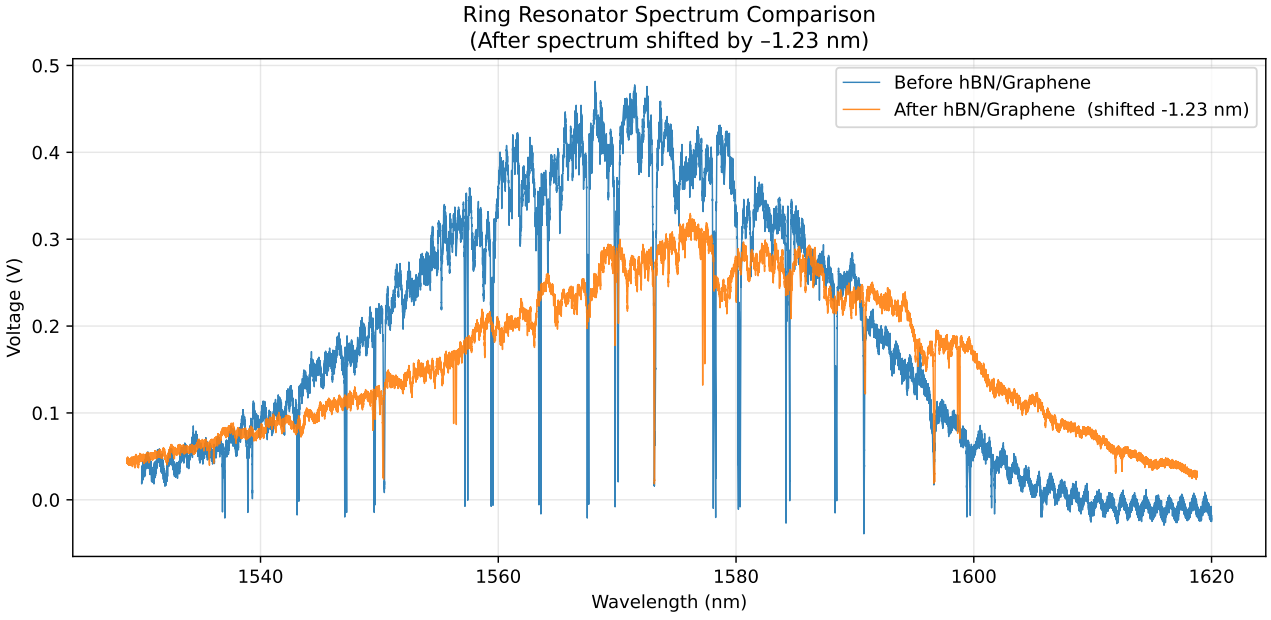


Figure 7.7: Transmission spectra before (blue) and after (orange) heterostructure transfer, after rigid alignment of the reference resonance (R6) by $-1.23\,\mathrm{nm}$. All resonances now overlap except for one distinct feature belonging to the ring that interacted with the hBN/graphene stack.

After applying the rigid wavelength shift of $\Delta\lambda = -1.23\,\mathrm{nm}$ derived from the unaffected reference resonance R6, the two spectra can be compared on a common wavelength axis (Figure 7.7). With the reference features superimposed, the residual spectral differences become immediately apparent: **all resonances superpose to within the measurement precision except those belonging to the R1 family**.

This unique displacement of R1 unambiguously identifies the ring that interacts with the hBN/graphene heterostructure.

A naive comparison of the aligned after-transfer feature near 1577.2 nm with the original R1 of FSR 3 (1578.09 nm) would suggest a small differential blue-shift of approximately 0.9 nm. Such a blue-shift is physically unexpected: placement of multilayer hBN ($n \approx 2.13$ at 1550 nm) on a silicon waveguide produces dielectric loading of the guided mode and must result in a *red*-shift. The same red-shift is consistently reported throughout the literature on hBN-integrated silicon and silicon-nitride ring resonators.

The only consistent interpretation is therefore that the resonance observed near 1577.2 nm after alignment is not a slightly blue-shifted R1 of FSR 3, but the original R1 of FSR 2 that has undergone a red-shift of one full free spectral range. The measured positions of the R1 family before and after transfer are summarised in Table 7.2.

Table 7.2: Measured wavelengths of Resonance R1 in three consecutive free spectral ranges before and after heterostructure transfer. The large red-shift of approximately one FSR is evident.

	FSR 1 (nm)	FSR 2 (nm)	FSR 3 (nm)
Before transfer	1536.80	1557.20	1578.09
After transfer (raw)	1557.475	1578.43	1599.87
True shift $\Delta\lambda_{R1}$		+21.23	

Taking the clearest corresponding pair (original FSR 2 R1 at 1557.20 nm and the feature that appears at 1578.43 nm after transfer) yields

$$\Delta\lambda_{R1} = 1578.43\,\text{nm} - 1557.20\,\text{nm} = +21.23\,\text{nm}. \tag{7.5}$$

This large positive shift is the direct spectroscopic signature of the strong increase in effective refractive index induced by the relatively thick hBN membrane.

In addition to the centre-wavelength shift, the lineshape of Resonance R1 was analysed quantitatively. A Lorentzian function of the form [68]

$$T(\lambda) = T_0 - \frac{A\,(\gamma/2)^2}{(\lambda - \lambda_0)^2 + (\gamma/2)^2} \tag{7.6}$$

was fitted to the measured transmission dips of the identified resonance (before transfer at 1557.20 nm and after transfer at 1578.43 nm). Here T_0 is the off-resonance baseline, A is the dip depth, λ_0 is the resonance wavelength and γ is the full width at half-maximum (FWHM). The resulting fit parameters are summarised in Table 7.3 and the corresponding experimental data together with the fitted curves are shown in Figure 7.8.

Table 7.3: Lorentzian fit parameters of the correctly identified Resonance R1 before and after heterostructure transfer.

Parameter	Before transfer	After transfer
Centre wavelength λ_0 (nm)	1557.193	1578.421
FWHM γ (nm)	0.0332	0.0211
Loaded quality factor $Q = \lambda_0/\gamma$	4.70×10^4	7.48×10^4
Finesse $\mathcal{F} = \text{FSR}/\gamma$	615	967
Extinction ratio (linear)	∞	2.30
Extinction ratio (dB)	–	3.62

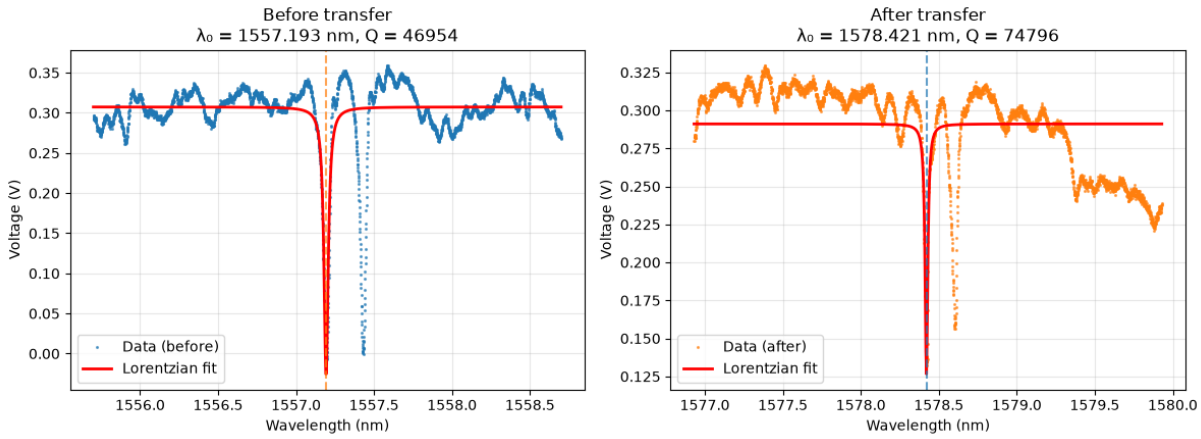


Figure 7.8: Lorentzian fits to the correctly identified Resonance R1 before (blue, centred at 1557.19 nm) and after (orange, centred at 1578.42 nm) transfer of the hBN/graphene heterostructure. The solid red curves are the fitted Lorentzian lineshapes. The resonance remains high-Q after transfer despite the additional optical loss introduced by the partially covering graphene flake.

The loaded quality factor $Q = \lambda_0/\gamma$ quantifies the photon lifetime relative to the optical period: a higher Q implies a steeper resonance slope and therefore a larger transduction gain for any refractive-index (or displacement) perturbation. The corresponding finesse $\mathcal{F} = \mathrm{FSR}/\gamma$ represents the approximate number of cavity round-trips made by a photon before its energy decays to $1/e$; it is the figure of merit that governs the resonant field enhancement. Both quantities increased after transfer (Q from 4.70×10^4 to 7.48×10^4, finesse from 615 to 967).

Typical loaded Q values reported for standard (non-ultra-high-Q) SOI ring resonators in the C-band lie in the range 10^4–10^5; values exceeding 10^6 require specialised fabrication (e.g. LOCOS or multimode waveguides) that is not employed here. The measured figures therefore sit comfortably within the expected performance window for devices intended for sensing rather than ultra-narrow-linewidth applications. The simultaneous rise in Q and finesse, despite the introduction of a partially absorbing graphene flake, indicates that the additional round-trip loss remains subordinate to the intrinsic cavity losses under the present coupling conditions.

The extinction ratio, which dropped to 3.62 dB, directly reflects the increase in cavity absorption caused by the graphene. While a deeper extinction would improve the signal-to-noise ratio of the intensity readout, a contrast of a few decibels is still sufficient for locking the laser to the resonance flank and for resolving both Brownian and driven membrane motion, as demonstrated in the subsequent actuation experiments.

From the measured red-shift of $\Delta\lambda = +21.23$ nm and the group index $n_g \approx 2.74$ obtained from the free spectral range and ring radius, the change in effective refractive index is

$$\Delta n_{\mathrm{eff}} = n_g \frac{\Delta\lambda}{\lambda} \approx 0.037. \tag{7.7}$$

This value quantifies the dielectric loading of the guided mode by the multilayer hBN membrane ($n_{\mathrm{hBN}} \approx 2.13$). Thin monolayer or few-layer 2-D materials typically produce Δn_{eff} of order 10^{-3}–10^{-2}; the comparatively large shift observed here is therefore consistent with the substantial thickness of the transferred hBN flake and confirms strong spatial overlap between the optical mode and the suspended membrane—an essential prerequisite for both efficient optomechanical readout and optothermal actuation.

7.2.4 Discussion of the Observed Resonance Shift Direction

The unique displacement of the R1 family after global alignment of the reference resonator R6 constitutes clear spectroscopic evidence that this ring is covered by the transferred hBN/graphene heterostructure.

According to the resonance condition

$$m\lambda_m = 2\pi R\, n_{\mathrm{eff}}, \tag{7.8}$$

any increase in the effective refractive index n_{eff} of the guided mode produces a red-shift of the resonance wavelength. Placement of a multilayer hBN membrane ($n \approx 2.13$ at 1550 nm) above the silicon waveguide is

expected to raise n_{eff} through dielectric loading of the optical mode's evanescent field. Consequently a red-shift relative to the bare resonator was anticipated, and is indeed universally reported in the literature on hBN-integrated silicon and silicon-nitride ring resonators.

A naive comparison of the aligned post-transfer feature near 1577.2 nm with the original R1 of FSR 3 would appear to suggest a small blue-shift. This interpretation is incorrect. The feature observed after transfer is the original R1 of FSR 2 (1557.20 nm) that has undergone a red-shift of one full free spectral range:

$$\Delta\lambda_{\text{R1}} = 1578.43\,\text{nm} - 1557.20\,\text{nm} = +21.23\,\text{nm}. \tag{7.9}$$

The corresponding change in effective index is $\Delta n_{\text{eff}} \approx 0.037$. This magnitude is substantial and consistent with dielectric loading by a relatively thick multilayer hBN flake in intimate contact with the waveguide over a significant fraction of the ring circumference. Thin (monolayer or few-layer) 2D materials typically produce far smaller shifts; the observed value therefore supports strong spatial overlap between the guided optical mode and the suspended membrane.

The quantitative lineshape analysis requires a more cautious interpretation. The reduction in extinction ratio to 3.62 dB is expected: the partially covering graphene flake introduces additional round-trip absorption and moves the resonator further from critical coupling. In contrast, the observed increase in loaded quality factor (from $Q \approx 4.70 \times 10^4$ to $Q \approx 7.48 \times 10^4$) and the corresponding rise in finesse (from 615 to 967) are unexpected. Graphene absorption at 1550 nm is significant ($\sim 2.3\,\%$ per monolayer); even partial coverage should increase cavity loss and broaden the resonance. An increase in loaded Q therefore cannot be explained by a simple reduction in intrinsic loss.

A plausible mechanism is a change in the extrinsic coupling rate. The large shift in effective index and the accompanying modification of the mode profile alter the phase-matching and field overlap between the bus waveguide and the ring. This can move the device relative to the critical- coupling condition and reduce the contribution of coupling loss to the loaded linewidth, even while the intrinsic loss rises. Alternative contributions (small differences in launch polarisation, optical power, or fitting range between the two measurements) cannot be fully excluded with the present data. Loaded Q values in the mid-10^4 range remain typical for standard SOI ring resonators used in sensing applications. The absolute value after transfer is therefore still adequate for flank locking and displacement readout. The increase itself, however, should be regarded as provisional until intrinsic and extrinsic contributions can be separated.

Taken together, the large red-shift establishes successful placement of the heterostructure and strong dielectric loading, while the residual absorption evidenced by the reduced extinction ratio provides the optical loss channel required for optothermal actuation. The optical transducer remains sufficiently high-Q to support the subsequent driven-response experiments, even if the apparent improvement in loaded Q is not fully understood.

Because an increase in loaded quality factor after the addition of an absorbing graphene flake is physically unexpected, the reference resonator R6 was examined as a control. Resonance R6 lies at a substantial lateral distance from the transfer site and is demonstrably unaffected by the hBN/graphene heterostructure; any change observed in its lineshape must therefore arise from differences in the measurement conditions rather than from the transferred material.

Lorentzian fits performed on the same R6 resonance before and after transfer yield the following parameters. Before transfer the centre wavelength is 1573.13 nm with a loaded quality factor $Q \approx 9.26 \times 10^3$. After transfer the resonance appears at 1574.36 nm and the loaded quality factor rises to $Q \approx 2.49 \times 10^4$. This corresponds to a relative increase of approximately 169 %.

The large change in the quality factor of an uncovered reference resonator indicates that the optical measurement conditions were not identical between the two sessions. In particular, the input polarisation was adjusted with manual fibre polarisers, the fibre-to-chip coupling was optimised by exchanging the optical fibres, and the measurements were performed at ambient laboratory temperature. Any of these factors (especially polarisation state and coupling efficiency) can alter the apparent loaded linewidth of a ring resonator.

Consequently, the apparent increase in the loaded Q of Resonance R1 cannot be attributed with confidence to the presence of the heterostructure. Both the sensor ring and the reference ring exhibit higher loaded Q values in the post-transfer spectrum, pointing to a systematic difference in the experimental conditions rather than a physical reduction of cavity loss. The differential red-shift of R1 relative to R6 (+21.23 nm) remains robust, as does the reduction in extinction ratio of R1, which is consistent with additional absorption introduced by the partially covering graphene flake. The optical transducer is still of sufficient quality for the subsequent

optothermal actuation experiments, but a quantitative claim that the intrinsic photon lifetime improved after transfer is not supported by the control measurement.

7.3 Optothermal Actuation and Driven Response

To investigate whether the partially transferred multilayer graphene flake can provide deterministic optothermal actuation of the suspended hBN membrane, intensity-modulated optical drive experiments were performed using the setup described in Section 7.3. The same continuous-wave laser used for Brownian-motion readout was locked to the flank of the photonic resonance and amplitude-modulated at selected frequencies. The modulation produces a periodic variation in the optical power incident on the graphene, providing a potential optothermal driving mechanism for the hybrid graphene/hBN membrane.

The purpose of this measurement is not to assume that every coherent signal observed under modulation originates from mechanical motion. Instead, the measurement is used to determine whether the optically modulated device exhibits a frequency-dependent coherent response in the frequency range of the independently observed thermomechanical resonance. Such a response would provide evidence for a mechanically driven contribution, while the present measurement does not by itself allow the mechanically driven contribution to be separated quantitatively from direct optical or electrical feed-through.

7.3.1 Verification of basic functionality

Before investigating optothermal actuation, the optical readout and mechanical response of the device were verified. The laser was locked to the steep flank of the resonance previously identified as R1 in FSR 3 at a wavelength of 1578.42 nm. A clear and reproducible thermomechanical (Brownian) peak was observed at this operating point, confirming that the suspended hBN membrane produces a measurable optomechanical signal.

Three basic requirements are relevant before interpreting a coherent response under optical modulation:

1. **Optical readout integrity** – The thermomechanical (Brownian) peak of the membrane must be clearly resolved and reproducible. Its observation confirms that the photonic circuit, fibre-to-chip coupling, and photodetection chain are capable of resolving the membrane motion above the measurement noise.
2. **Mechanical suspension and optomechanical transduction** – The observation of the Brownian resonance confirms that the hBN membrane is mechanically suspended and that its out-of-plane motion modulates the optical signal with sufficient sensitivity to be detected.
3. **Potential optical absorption pathway** – The optical characterization discussed in the previous sections shows an additional optical loss after graphene transfer. This loss is consistent with the presence of an additional absorption channel introduced by the graphene and therefore provides the optical pathway required for optothermal excitation. The optical measurements alone, however, do not establish the magnitude of the absorbed power or the resulting thermal force.

With these conditions established, the device was subjected to intensity-modulated optical excitation.

7.3.2 Multi-frequency spectra at 15 mVpp

A systematic set of spectrum-analyser measurements was acquired at drive frequencies of 12 MHz, 13 MHz, 14 MHz, 20 MHz and 30 MHz, all with a fixed modulation amplitude of 15 mVpp. The five spectra are overlaid in Figure 7.9.

The spectra contain two qualitatively different features. First, a broad thermomechanical background is observed in the region of approximately 10–15 MHz, with its maximum near 13 MHz. This feature is the independently observed Brownian response of the membrane and identifies the frequency region of the mechanical resonance. Second, a narrow coherent spectral peak appears at the frequency of each applied optical modulation. These peaks therefore represent a deterministic response at the imposed drive frequency.

The presence of a coherent peak alone does not prove that the membrane is being mechanically driven, since direct optical modulation and residual electrical cross-talk can also produce a coherent signal at the modulation frequency. The frequency dependence of the coherent response is therefore examined in more detail below.

7.3.3 Extraction of absolute and excess spike heights

Two complementary quantities were extracted from each spectrum (Figure 7.10).

- **Absolute height** (blue) quantifies the total measured power at the drive frequency relative to the global noise floor. It therefore contains the coherent response together with the local thermomechanical background and any residual coherent feed-through.

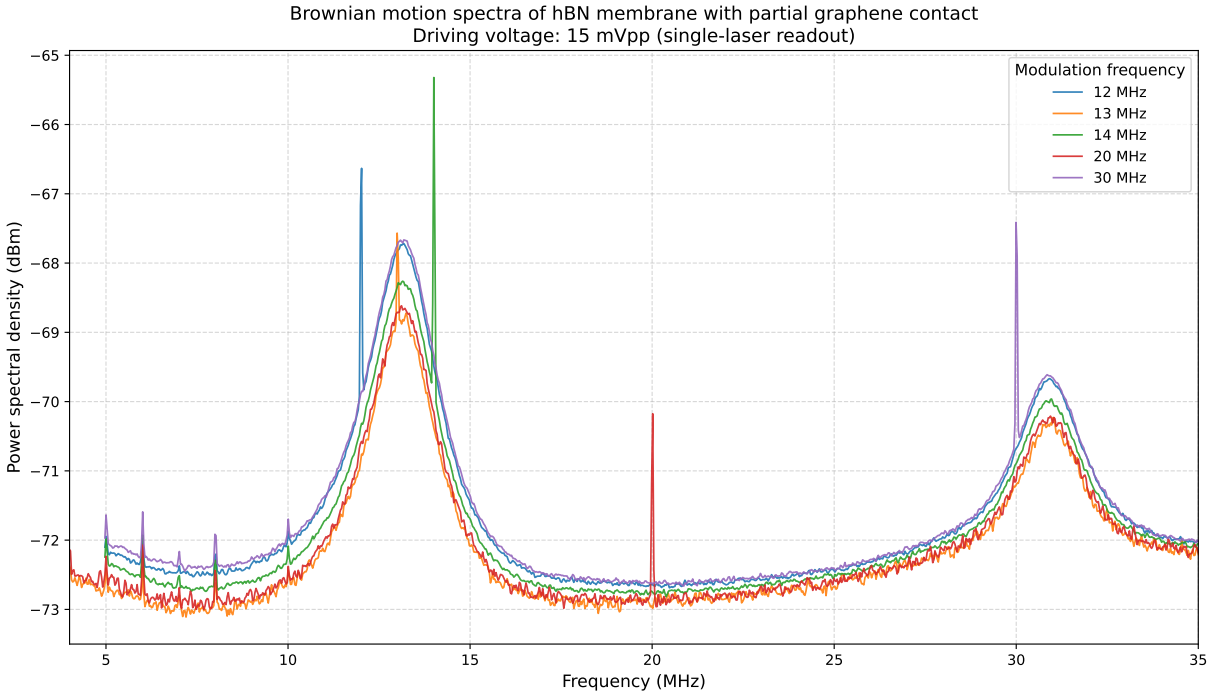


Figure 7.9: Brownian-motion spectra of the hybrid graphene/hBN membrane recorded at five different intensity-modulation frequencies (12, 13, 14, 20 and 30 MHz) with a fixed drive amplitude of 15 mVpp. A broad thermomechanical response extends over approximately 10–15 MHz, while sharp coherent spikes appear at the respective drive frequencies.

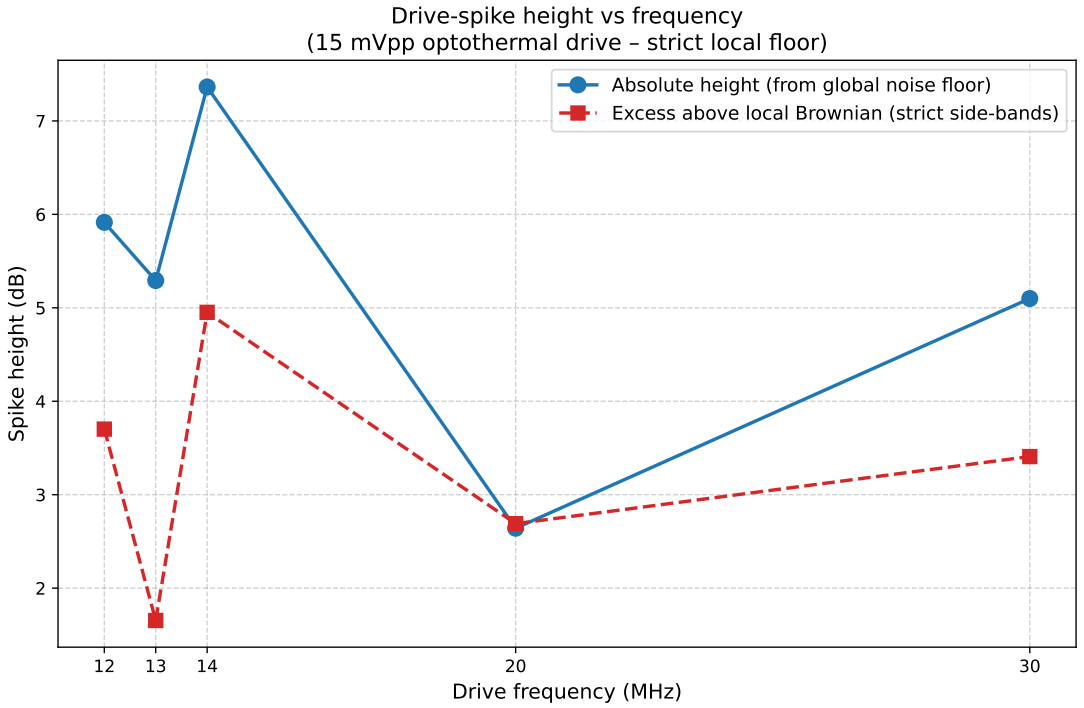


Figure 7.10: Drive-spike height versus frequency for the 15 $\mathrm{mV_{pp}}$ data set. Blue circles: absolute spike height measured from the global noise floor. Red squares: spike height above the local Brownian background.

- **Excess height above the local Brownian background** (red) quantifies how far the coherent spectral peak rises above the Brownian continuum at the same frequency. This removes the frequency-dependent incoherent Brownian background and provides a more appropriate quantity for comparing the coherent response at different drive frequencies.

The numerical values extracted from the five spectra are summarised in Table 7.4. The absolute and excess heights are expressed in dB and are defined relative to the corresponding noise reference.

Table 7.4: Spike-height extraction from the 15 $\mathrm{mV_{pp}}$ spectra using a strict local-floor definition. The absolute height is measured relative to the global noise floor, while the excess height is measured relative to the local Brownian continuum.

Drive freq. (MHz)	Spike freq. (MHz)	Spike tip (dBm)	Global noise floor (dBm)	Abs. height (dB)	Local Brownian floor (dBm)	Excess (dB)
12	12.02	−66.63	−72.55	5.91	−70.33	3.70
13	13.00	−67.57	−72.68	5.29	−69.22	1.65
14	14.00	−65.32	−72.68	7.36	−70.27	4.95
20	20.02	−70.18	−72.82	2.64	−72.87	2.69
30	30.00	−67.41	−72.51	5.10	−72.82	3.41

The excess height exhibits its largest measured value near 14 MHz, reaching 4.95 dB. Importantly, this frequency lies within the broad 10–15 MHz region in which the independently measured thermomechanical response is observed. The maximum at 14 MHz is therefore not interpreted as a separate mechanical resonance; rather, the response is enhanced within the frequency range of the independently identified membrane resonance.

At 20 MHz the excess decreases to approximately 2.7 dB. This value may contain a contribution from residual coherent feed-through, but the present measurements do not provide sufficient information to identify the 20 MHz response as purely feed-through. Similarly, the increase observed at 30 MHz is retained for completeness, but it is not used as evidence for the fundamental mechanical mode because additional structure is visible in the corresponding spectrum and could arise from a higher-order mechanical mode or from measurement artefacts.

The important observation is therefore the enhanced coherent response in the vicinity of the independently measured thermomechanical resonance. This behaviour is consistent with a mechanically driven contribution to the coherent response, although the present measurement does not allow the mechanical contribution to be isolated from direct optical or electrical feed-through.

7.3.4 Amplitude-domain interpretation of the coherent response

The spectrum-analyser traces are power measurements. A physically useful interpretation is obtained by considering the coherent signal in the amplitude domain. At the drive frequency f_d, the detected coherent amplitude can be represented schematically as

$$A_\mathrm{coh}(f_\mathrm{d}) = A_\mathrm{feed}(f_\mathrm{d}) + A_\mathrm{mech}(f_\mathrm{d}), \tag{7.10}$$

where A_feed represents coherent signal components that do not require mechanical motion, while A_mech represents the coherent contribution generated by optothermally driven membrane motion.

The feed-through term can include the fraction of the intentional optical intensity modulation that reaches the detector directly through the optical transmission path, as well as any residual electrical cross-talk. These contributions are phase coherent with the modulation waveform.

The mechanical contribution arises if the modulated optical power absorbed by the graphene produces a periodic temperature variation and the associated thermoelastic stress drives the membrane. The resulting membrane displacement modulates the optical signal and therefore produces a coherent photocurrent component at the same drive frequency. This contribution is also phase coherent with the modulation.

The thermomechanical Brownian motion has different statistical properties. Brownian motion is stochastic and therefore appears as an incoherent background rather than as a deterministic spectral line. Consequently, after accounting for the local Brownian background, the remaining coherent power is associated with the coherent combination of the feed-through and mechanically driven contributions.

In terms of the coherent amplitudes, the measured coherent power can therefore be written as

$$P_{\mathrm{coh}}(f_{\mathrm{d}}) \propto \left|A_{\mathrm{feed}}(f_{\mathrm{d}}) + A_{\mathrm{mech}}(f_{\mathrm{d}})\right|^2 . \tag{7.11}$$

This expression is important for interpreting the present measurements. The excess-height analysis removes the incoherent Brownian background, but it does not separate A_{feed} from A_{mech}. The frequency dependence of the remaining coherent response, particularly its enhancement within the thermomechanical resonance region, is therefore used as evidence for a mechanical contribution rather than as a direct measurement of the mechanical displacement alone.

7.3.5 Quantitative extraction of the coherent amplitude

For each drive frequency, the excess height Δ is the difference in dB between the spectral peak and the local Brownian background. The corresponding ratio between the total power at the spectral peak and the local Brownian background is

$$\frac{P_{\mathrm{total}}}{P_{\mathrm{floor}}} = 10^{\Delta/10}. \tag{7.12}$$

Because the measured peak contains the local Brownian background in addition to the coherent spectral line, the coherent power associated with the narrow peak is obtained by subtracting the local Brownian contribution in linear units:

$$P_{\mathrm{coh}} = P_{\mathrm{floor}} \left(10^{\Delta/10} - 1\right). \tag{7.13}$$

This distinction is important because subtraction must be performed in linear power units rather than directly in dB.

For the 12–14 MHz measurements, the resulting coherent powers are approximately

$$P_{\mathrm{coh}}(12\,\mathrm{MHz}) \approx 124\,\mathrm{pW}, \tag{7.14}$$

$$P_{\mathrm{coh}}(13\,\mathrm{MHz}) \approx 55\,\mathrm{pW}, \tag{7.15}$$

and

$$P_{\mathrm{coh}}(14\,\mathrm{MHz}) \approx 200\,\mathrm{pW}. \tag{7.16}$$

These values quantify the coherent spectral line above the local Brownian background. They should not be interpreted as purely mechanical power, since the coherent signal can contain both feed-through and mechanically driven contributions.

Assuming a $50\,\Omega$ analyser input, the corresponding RMS voltage is

$$V_{\mathrm{rms}} = \sqrt{P_{\mathrm{coh}} R}, \tag{7.17}$$

while the peak voltage amplitude of the equivalent sinusoidal signal is

$$V_{\mathrm{pk}} = \sqrt{2 P_{\mathrm{coh}} R}. \tag{7.18}$$

For the three frequencies closest to the fundamental mechanical resonance, this gives approximately

$$V_{\mathrm{pk}} \approx 112\,\mu\mathrm{V}, \quad 74\,\mu\mathrm{V}, \quad 141\,\mu\mathrm{V} \tag{7.19}$$

for 12, 13 and 14 MHz, respectively.

A convenient dimensionless quantity for comparing the coherent tone with the local Brownian background is the relative coherent amplitude,

$$A_{\mathrm{rel}} = \sqrt{10^{\Delta/10} - 1}. \tag{7.20}$$

For the 12, 13 and 14 MHz measurements, this gives approximately

$$A_{\mathrm{rel}} \approx 1.16, \quad 0.68, \quad 1.46, \tag{7.21}$$

respectively.

This quantity expresses the coherent amplitude of the spectral line relative to the RMS Brownian background within the measurement bandwidth. It is useful for comparing the strength of the coherent response against the local thermomechanical noise, but it should not be interpreted as a calibrated mechanical displacement.

7.3.6 Estimated driven displacement – supplementary quantitative analysis

The coherent voltage amplitudes obtained above remain in the electrical domain. Converting them into a physical membrane displacement requires an absolute calibration of the optical transduction factor. This calibration can be estimated from the thermomechanical noise using the equipartition theorem, provided that the effective mechanical mass, spring constant and measured Brownian voltage spectrum are known.

In thermal equilibrium, the equipartition theorem gives

$$\langle x^2 \rangle = \frac{k_{\mathrm{B}} T}{k_{\mathrm{eff}}}, \tag{7.22}$$

where k_{B} is Boltzmann's constant, T is the absolute temperature, and k_{eff} is the effective spring constant of the mechanical mode.

For a mechanical mode with effective mass m_{eff} and resonance frequency f_0,

$$k_{\mathrm{eff}} = m_{\mathrm{eff}} (2\pi f_0)^2. \tag{7.23}$$

The effective mass depends on the membrane geometry and thickness and therefore introduces an uncertainty in the absolute calibration when the membrane thickness is not known independently.

Displacement and voltage spectral densities

Under the assumption of linear optomechanical transduction, the voltage and displacement spectral densities are related by

$$S_{VV}(f) = \left(\frac{\partial V}{\partial x} \right)^2 S_{xx}(f), \tag{7.24}$$

where $\partial V / \partial x$ is the optical transduction factor.

If the measured frequency interval contains the complete contribution of the mechanical mode and the electronic noise floor has been removed, integration gives

$$\int S_{VV}(f)\, \mathrm{d}f = \left(\frac{\partial V}{\partial x} \right)^2 \frac{k_{\mathrm{B}} T}{k_{\mathrm{eff}}}. \tag{7.25}$$

The transduction factor can therefore be estimated from

$$\frac{\partial V}{\partial x} = \sqrt{\frac{\int S_{VV}(f)\, \mathrm{d}f}{k_{\mathrm{B}} T / k_{\mathrm{eff}}}}. \tag{7.26}$$

In practice, the Brownian spectrum is integrated over the selected measurement window after subtraction of the electronic noise floor and exclusion of the coherent drive spike. Because the present measurement window does not constitute a complete independent calibration of all mechanical parameters, the resulting transduction factor should be regarded as an estimate rather than a device-specific absolute calibration.

The numerical values of the integrated voltage spectral density evaluated for the three spectra nearest the mechanical resonance are summarised in Table 7.5. The corresponding numerical conversion from the raw spectrum-analyser data to the integrated voltage variance is given in Appendix E.

Table 7.5: Integrated thermomechanical voltage spectral density for the spectra nearest the fundamental mechanical resonance. The integration is performed over the selected 8–18 MHz frequency window after removal of the electronic noise floor and exclusion of the coherent drive spike.

Drive frequency (MHz)	$\int_{8\,\mathrm{MHz}}^{18\,\mathrm{MHz}} S_{VV}^{\mathrm{mech}}(f)\,df$ (V^2)
12	2.99×10^{-7}
13	1.82×10^{-7}
14	2.40×10^{-7}

Because the integrated Brownian response varies between the three measurements, the corresponding calibration should be interpreted as an order-of-magnitude estimate. In particular, a rigorous absolute calibration would require a device-specific determination of the membrane thickness and residual mechanical tension, together with a consistent acquisition of the complete mechanical mode under identical measurement conditions.

Conversion of the coherent amplitude

If the optical transduction factor is known, the coherent voltage amplitude can be related to an equivalent displacement amplitude through

$$V_{\mathrm{pk}} = \frac{\partial V}{\partial x} x_{\mathrm{drive}}. \tag{7.27}$$

The corresponding displacement estimate is therefore

$$x_{\mathrm{drive}} = \frac{V_{\mathrm{pk}}}{\partial V/\partial x}. \tag{7.28}$$

In the present work, a device-specific atomic-force-microscopy measurement of the membrane thickness was not available. An independent estimate of the optical transduction factor can nevertheless be obtained using the measured suspended radius $a = 7\,\mu$m and assuming an hBN thickness in the range 5–70 nm. With these assumptions, the estimated transduction factor lies in the approximate range

$$\frac{\partial V}{\partial x} \approx 0.014\text{–}0.053\,\mathrm{V\,nm^{-1}}. \tag{7.29}$$

Applying this range to the corrected coherent voltage amplitudes gives approximate driven displacement amplitudes of

$$x_{\mathrm{drive}} \approx 2.1\text{–}8.0\,\mathrm{pm} \tag{7.30}$$

at 12 MHz,

$$x_{\mathrm{drive}} \approx 1.4\text{–}5.3\,\mathrm{pm} \tag{7.31}$$

at 13 MHz, and

$$x_{\mathrm{drive}} \approx 2.7\text{–}10.1\,\mathrm{pm} \tag{7.32}$$

at 14 MHz.

These values should be regarded as order-of-magnitude estimates rather than definitive measurements of the mechanical displacement. In particular, the coherent voltage contains both the mechanically driven contribution and possible coherent feed-through, while the optical transduction calibration depends on uncertain device parameters.

7.3.7 Interpretation and limitations

The measurements provide several pieces of evidence relevant to the proposed optothermal actuation mechanism.

First, the Brownian spectrum independently establishes a broad thermomechanical resonance of the suspended hBN membrane in the approximately 10–15 MHz frequency range, with a maximum near 13 MHz. This confirms that the membrane possesses a mechanically active mode that can be detected through the integrated photonic readout.

Second, when the laser intensity is modulated, a narrow coherent spectral peak appears at the imposed modulation frequency. This demonstrates that the optical modulation produces a deterministic coherent response in the detected signal.

Third, the magnitude of this coherent response depends on the modulation frequency. The largest measured excess above the local Brownian background occurs at 14 MHz, which lies within the frequency range of the independently observed thermomechanical resonance. The proximity of the strongest coherent response to this mechanical resonance region is consistent with a mechanically driven contribution to the measured signal.

The present measurement does not, however, allow the coherent signal to be uniquely decomposed into its feed-through and mechanically driven components. In general,

$$A_{\mathrm{coh}} = A_{\mathrm{feed}} + A_{\mathrm{mech}}, \tag{7.33}$$

so that

$$P_{\mathrm{coh}} \propto \left|A_{\mathrm{feed}} + A_{\mathrm{mech}}\right|^2 . \tag{7.34}$$

The excess-height analysis removes the incoherent Brownian background, but it does not remove or independently quantify the coherent feed-through. Consequently, the measured 4.95 dB maximum at 14 MHz should not be interpreted as a purely mechanical response.

The result should therefore be regarded as a proof-of-concept demonstration providing evidence consistent with optothermal actuation of the graphene/hBN platform, rather than as a fully isolated quantitative measurement of mechanical actuation efficiency.

The estimated driven displacements are in the picometre range and are substantially smaller than the theoretical lower bound of approximately 0.1 nm obtained from the idealised bimorph model. This discrepancy may arise from several factors, including partial graphene–hBN contact, residual membrane tension, thermal low-pass filtering at the modulation frequencies, limited optical absorption in the graphene flake, and uncertainties in the absolute displacement calibration.

A more definitive demonstration and quantitative characterisation of the actuation mechanism would require an independent control experiment and a phase-sensitive measurement. In particular, a membrane without graphene operated under otherwise identical optical modulation conditions would help distinguish direct thermo-optic or optical feed-through effects from graphene-mediated mechanical actuation. A phase-sensitive frequency-response measurement would additionally provide amplitude and phase information and allow the mechanical contribution to be separated more reliably from the coherent background.

Overall, the measurements demonstrate that the graphene/hBN platform exhibits a coherent optically driven response whose strongest measured contribution occurs within the independently identified thermomechanical resonance region. This behaviour provides evidence consistent with the proposed optothermal actuation mechanism, while the quantitative separation of mechanical actuation from coherent feed-through remains an important direction for future work.

Chapter 8

DISCUSSION

The experimental results of Chapter 7 demonstrate that a partially transferred multilayer graphene flake can generate a detectable, frequency-dependent mechanical response in a suspended hBN membrane that is simultaneously read out by an integrated silicon-photonic ring resonator at 1550 nm. This chapter provides a higher-level interpretation of those findings, situates them with respect to the theoretical framework of Chapter 5, and states the residual limitations.

8.1 Synthesis of Optical and Mechanical Results

The passive optical characterisation establishes that the dry-transfer process successfully integrates the graphene/hBN heterostructure with a functional photonic circuit. The sensor ring experiences a large red-shift consistent with strong dielectric loading by the multilayer hBN, while the partial graphene coverage introduces a controlled amount of optical absorption. A usable high-Q resonance is retained, enabling sensitive flank locking for displacement readout.

The intensity-modulated drive experiments then show a coherent response at the imposed modulation frequency. The response is strongest within the frequency range of the independently observed thermomechanical resonance, providing evidence consistent with a mechanically mediated contribution to the measured signal. Because the coherent signal may contain both mechanically driven response and direct optical or electrical feed-through, the mechanical contribution cannot be isolated quantitatively from the present measurements. The optical and mechanical observations are therefore mutually consistent at a qualitative level: the heterostructure strongly perturbs the photonic mode while the modulation experiment provides evidence for optothermal actuation of the hybrid graphene/hBN platform.

8.2 Relation to the Theoretical Framework

Chapter 5 identified three possible routes from absorbed optical power to out-of-plane motion. Direct thermal loading of a homogeneous hBN drum is expected to produce primarily parametric tension tuning, while a pure mechanical stress-transfer model does not fully account for the concurrent thermal expansion of the hBN. The observed coherent response within the independently identified mechanical-resonance region is therefore consistent with the third mechanism: coupled bimorph actuation arising from differential thermal expansion of the graphene and hBN layers. However, the present measurements do not independently distinguish this mechanism from all other possible thermally mediated pathways, so the bimorph interpretation should be regarded as the most plausible mechanism within the theoretical framework rather than as uniquely demonstrated.

The absolute efficiency, however, is substantially lower than predicted. The equivalent coherent displacement estimates are in the picometre range and are substantially smaller than the theoretical lower bound of 0.1nm predicted by the idealised bimorph model. Because the coherent signal may contain direct optical or electrical feed-through and because the displacement calibration depends on uncertain device parameters, this discrepancy should not be interpreted as a direct quantitative measure of the mechanical actuation efficiency.

8.3 Limitations

The data set is limited to a single successful device. Systematic variation of graphene thickness, contact-area fraction and air-gap height was not possible, so the parametric trends predicted in Chapter 5 can be confirmed only qualitatively. In addition, the absolute displacement scale relies on an estimate of the optical transduction factor derived from the measured thermomechanical noise and the known lateral dimensions of the membrane,

rather than a device-specific AFM thickness calibration. The reported picometre-range values should therefore be regarded as order-of-magnitude estimates. Finally, changes in optical measurement conditions between the pre- and post-transfer spectra preclude any quantitative claim about an improvement in photon lifetime caused by the heterostructure.

A further limitation concerns the interpretation of the coherent driven response. The spectrum-analyser measurement does not provide phase information and therefore cannot separate the mechanically driven contribution from coherent optical or electrical feed-through. The measured excess above the Brownian background should consequently be interpreted as the total coherent response rather than as a direct measurement of mechanical motion.

8.4 Assessment of competing mechanisms

A rigorous interpretation of the observed coherent response requires explicit examination of alternative mechanisms that could produce frequency-dependent spectral features without genuine mechanical motion of the membrane. The principal candidates are considered below, together with the experimental observations that constrain each interpretation.

Electrical and optical feed-through

Residual electrical coupling of the AWG signal into the detection chain, or residual optical intensity modulation transmitted through the ring, would both produce a coherent tone at the drive frequency. Such feed-through may itself exhibit a frequency-dependent transfer function; therefore, its contribution cannot be assumed to be perfectly constant across the measurement band. Nevertheless, the observed response exhibits a pronounced enhancement near 14 MHz (Figure 7.11 and Table 7.4), coinciding with the independently observed thermomechanical resonance of the membrane. This resonance-centred enhancement indicates that a frequency-selective contribution is present. The data do not, however, allow this contribution to be separated quantitatively from any frequency-dependent feed-through.

Thus, electrical or optical feed-through may contribute to the measured coherent signal, but feed-through alone does not provide a sufficient explanation for the observed resonance-like enhancement near the membrane's mechanical resonance.

Photothermal modulation of the ring resonance

Absorption in the silicon waveguide or surrounding material could shift the optical resonance through the thermo-optic effect and thereby generate an intensity modulation without mechanical membrane motion. This mechanism cannot be excluded with complete certainty from the present data set. Nevertheless, two observations make a purely non-resonant thermo-optic origin unlikely.

First, the thermal response of a silicon photonic waveguide or ring is a low-pass filter whose time constant typically lies in the microsecond range, corresponding to a cut-off frequency of tens to a few hundred kilohertz. At the drive frequencies used here (12–30 MHz) one is therefore deep in the high-frequency roll-off. Thermo-optic modulation of the silicon waveguide or ring would introduce a thermal low-pass response. Such a mechanism would therefore be expected to become increasingly attenuated at sufficiently high modulation frequencies rather than producing a pronounced resonance-like enhancement around 14,MHz.

Second, the passive measurements independently resolve a clear thermomechanical (Brownian) peak of the suspended membrane at approximately the same frequency as the dominant coherent enhancement. The coincidence between the independently identified mechanical resonance and the frequency of the strongest driven response is difficult to explain by a purely photonic thermal effect.

A residual ambiguity nevertheless remains, because the present spectrum-analyser data provide only magnitude information. A genuine mechanical resonance is expected to exhibit a characteristic phase shift across the resonance, whereas a non-resonant thermo-optic modulation would not. Without a phase-sensitive measurement, this additional discriminant is unavailable. A future phase-sensitive measurement would provide amplitude and phase information across the resonance and would allow the mechanical contribution to be separated more reliably from coherent feed-through.

Global thermal effects and detector response

Global heating of the chip or fibre interface occurs on substantially longer thermal time scales than the 12–30 MHz modulation period and is therefore not expected to generate a strong coherent response in this frequency range. The analogue frontend of the spectrum analyser is specified to 200 MHz and operates within its linear regime over the measurement window. Furthermore, the electronic noise floor remains essentially flat across the

measured band. These observations make detector or amplifier roll-off an unlikely explanation for the observed resonance-centred frequency dependence.

Global thermal effects may therefore contribute to slow changes in the optical operating point, but they are not expected to generate the observed coherent response at the applied MHz modulation frequencies.

Higher-order mechanical modes

The modest recovery of excess height at 30 MHz is not uniquely assigned to a higher-order mechanical mode, since the available frequency sampling is insufficient to distinguish such a mode from residual frequency-dependent measurement-chain effects. The 30 MHz point is therefore retained as part of the measured response but is not interpreted as definitive evidence of a higher-order mechanical resonance.

In contrast, the dominant enhancement near 14 MHz remains consistent with the fundamental mechanical resonance independently identified from the thermomechanical spectrum. The correspondence between the passive mechanical resonance and the frequency of the strongest coherent response is therefore the principal frequency-domain evidence for mechanically mediated actuation.

Summary of the mechanical interpretation

TTaken together, the frequency dependence of the coherent response, its enhancement near the independently identified mechanical resonance, and the independent observation of the membrane's thermomechanical response provide evidence consistent with optothermally driven mechanical motion.

Electrical feed-through, global thermal effects, and detector response were considered as alternative explanations. While these effects may contribute to the measured coherent signal, none provides an obvious explanation for the pronounced enhancement within the independently identified mechanical-resonance region. Feed-through may contribute to the measured coherent signal, but the pronounced enhancement near the independently identified mechanical resonance indicates an additional frequency-selective contribution. The coincidence between the passive mechanical resonance and the driven coherent response is therefore consistent with excitation of the membrane's mechanical mode.

The principal residual ambiguity is photothermal modulation of the optical resonance itself. This mechanism cannot be excluded definitively using the present data set and would require a membrane-free control device measured under otherwise identical optical modulation conditions. Such a control would allow purely photonic thermal effects to be separated directly from mechanically mediated optothermal actuation.

Importantly, the primary objective of this work is to demonstrate the feasibility of optothermal actuation rather than to establish a device-specific absolute displacement calibration. The coherent, resonance-centred response therefore constitutes the primary experimental result. The displacement calculation presented separately provides an additional quantitative estimate of the magnitude of the driven motion, but is not required to establish the actuation itself.

Future experimental validation

The dual-laser configuration attempted in Section 6.4.2 was abandoned because of photodiode saturation under the combined optical power. A refined dual-laser architecture with improved optical isolation, independent power control, and appropriately matched photodiode dynamic range would provide a valuable follow-up experiment.

In particular, a membrane-free reference ring measured under otherwise identical optical modulation conditions would provide a direct test of photothermal modulation of the optical resonance. Comparison of the membrane-containing and membrane-free devices would allow purely photonic contributions to be separated more conclusively from mechanically mediated optothermal actuation.

A further improvement would be a denser frequency sweep around the approximately 14 MHz mechanical resonance, ideally with simultaneous phase-sensitive detection. Such a measurement would allow the mechanical transfer function to be resolved more clearly and would provide an additional means of distinguishing mechanical resonance from frequency-dependent feed-through.

Finally, a device-specific optical and displacement calibration would enable the optothermal response to be quantified in terms of absorbed optical power, force, and displacement amplitude. The displacement estimate presented in this thesis should therefore be regarded as a supplementary quantitative analysis, while the primary experimental conclusion remains the demonstration of optothermal actuation.

8.5 Answer to the Research Question

The central research question was whether a partially contacted multilayer graphene flake can provide optothermal actuation of a suspended hBN membrane integrated with a silicon-photonic waveguide at 1550,nm. The measurements provide evidence consistent with an affirmative answer. The passive measurements demonstrate successful integration of the graphene/hBN heterostructure with the photonic circuit and independently reveal the thermomechanical response of the suspended membrane. Under intensity-modulated optical excitation, a coherent response appears at the imposed modulation frequency, with its strongest measured enhancement occurring within the frequency range of the independently identified mechanical resonance. This behaviour is consistent with a mechanically mediated optothermal response, although the present measurements do not allow the mechanical contribution to be separated quantitatively from coherent optical or electrical feed-through. The hybrid graphene/hBN platform therefore provides a proof-of-concept demonstration of optically driven operation, while the absolute actuation efficiency and the detailed contribution of the bimorph mechanism remain subjects for future investigation.

Chapter 9

CONCLUSIONS

This work investigated whether a partially transferred multilayer graphene flake can provide optothermal actuation of a suspended hBN membrane integrated with a silicon-photonic strip ring-resonator readout at 1550 nm. The work extends a previously passive nanomechanical platform, capable of resolving Brownian motion, towards optically driven operation while retaining an electrode-free architecture and compatibility with integrated silicon photonics.

The principal scientific contributions may be summarised as follows:

- **Successful integration of the graphene/hBN heterostructure with the photonic platform.** A multilayer graphene/hBN heterostructure was successfully transferred onto a functional silicon-photonic ring resonator. The integration produced a large differential red-shift of the sensor resonance, $\Delta\lambda = +21.23\,\mathrm{nm}$, corresponding to $\Delta n_{\mathrm{eff}} \approx 0.037$ relative to an uncovered reference ring. This confirms strong optical loading by the transferred heterostructure while preserving a measurable optical transducer for the suspended membrane.
- **Independent observation of the membrane's thermomechanical response.** Brownian-motion measurements revealed a broad thermomechanical response in the approximately 10–15 MHz frequency range, with a maximum near 13 MHz. This establishes the mechanical resonance region of the suspended hBN membrane independently of the subsequent driven measurements.
- **Observation of a coherent optically driven response.** Under intensity-modulated optical excitation, narrow coherent spectral peaks were observed at the imposed modulation frequencies. After accounting for the local thermomechanical background, the coherent response exhibited its largest measured enhancement near 14 MHz, within the frequency range of the independently observed thermomechanical resonance. This frequency-dependent enhancement is consistent with a mechanically mediated contribution to the optically driven response and therefore provides evidence supporting the proposed optothermal actuation mechanism.
- **Quantitative estimation of the coherent response.** The coherent spectral peaks were analysed in the amplitude domain by subtracting the local Brownian contribution in linear power units. The resulting coherent voltage amplitudes were converted into equivalent membrane displacement amplitudes using an estimated optical transduction factor. The resulting values are in the picometre range and should be regarded as order-of-magnitude estimates because the coherent signal may contain both mechanically driven response and direct optical or electrical feed-through, while the absolute transduction calibration depends on uncertain device parameters.
- **Identification of the most plausible actuation mechanism and its limitations.** The theoretical analysis indicates that differential thermal expansion between graphene and hBN provides a plausible bimorph-like mechanism for converting absorbed optical power into out-of-plane membrane motion. Thermal low-pass filtering, partial graphene–hBN contact, residual membrane tension, and limited optical absorption provide plausible explanations for the relatively small observed response. However, the present measurements do not independently isolate the bimorph contribution or determine the absolute actuation efficiency.

Taken together, the results provide a proof-of-concept demonstration that a partially contacted graphene/hBN

membrane integrated with a silicon-photonic resonator can exhibit a coherent optically driven response that is enhanced within the independently identified mechanical-resonance region. The measurements therefore provide evidence consistent with optothermal actuation of the hybrid membrane. Importantly, the coherent response cannot be uniquely separated into mechanically driven and direct optical or electrical contributions using the present spectrum-analyser measurements. The work should consequently be regarded as a demonstration of the feasibility of the proposed optothermal actuation concept rather than as a complete quantitative characterisation of its mechanical efficiency.

The central research question of this thesis was whether a partially transferred multilayer graphene actuator can enable optothermal actuation of a suspended hBN nanomechanical resonator within an integrated silicon-photonic platform. The experimental results support an affirmative answer at the proof-of-concept level. The graphene/hBN integration successfully modifies the optical mode, the suspended membrane exhibits a clear thermomechanical response, and intensity-modulated optical excitation produces a coherent response whose strongest measured enhancement occurs in the mechanical-resonance region. These observations are mutually consistent with the proposed optothermal actuation mechanism.

Several experiments would strengthen and quantitatively validate this interpretation. First, a systematic fabrication campaign varying graphene thickness, graphene–hBN contact area, and device geometry would allow the influence of these parameters on the driven response to be investigated. Second, a graphene-free reference device subjected to the same optical modulation would provide a direct control for purely photonic and thermo-optic contributions. Third, a phase-sensitive frequency-response measurement, for example using a vector network analyser or lock-in-based detection, would provide both amplitude and phase information and would allow the mechanically driven contribution to be separated more reliably from coherent feed-through. Finally, an independent measurement of the membrane thickness and residual tension would substantially improve the absolute displacement calibration.

With these improvements, the platform could be investigated for higher-efficiency optothermal actuation, phase-sensitive optomechanical measurements, and future applications in integrated two-dimensional optomechanical sensing and multiplexed silicon-photonic devices.

References

[1] H. G. Craighead, "Nanoelectromechanical Systems," *Science* **290**, 1532–1535 (2000).

[2] K. L. Ekinci and M. L. Roukes, "Nanoelectromechanical systems," *Review of Scientific Instruments* **76**, 061101 (2005).

[3] M. Aspelmeyer, T. J. Kippenberg, and F. Marquardt, "Cavity optomechanics," *Reviews of Modern Physics* **86**, 1391–1452 (2014).

[4] R. Lifshitz and M. C. Cross, "Nonlinear Dynamics of Nanomechanical and Micromechanical Resonators," in *Reviews of Nonlinear Dynamics and Complexity*, Vol. 1 (Wiley-VCH, 2008).

[5] A. Eichler, J. Moser, J. Chaste, M. Zdrojek, I. Wilson-Rae, and A. Bachtold, "Nonlinear damping in mechanical resonators made from carbon nanotubes and graphene," *Nature Nanotechnology* **6**, 339–342 (2011).

[6] D. Rugar and P. Grütter, "Mechanical parametric amplification and thermomechanical noise squeezing," *Physical Review Letters* **67**, 699–702 (1991).

[7] X. Sun, L. Thylén, L. Wosinski, and S. L. He, "High-sensitivity integrated optical waveguide sensors for biochemical sensing," *Progress in Quantum Electronics* **38**, 1–45 (2015).

[8] D. Van Thourhout and J. Roels, "Optomechanical device actuation through the optical gradient force," *Nature Photonics* **4**, 211–217 (2010).

[9] J. S. Bunch *et al.*, "Electromechanical resonators from graphene sheets," *Science* **315**, 490–493 (2007).

[10] C. Lee, Q. Li, W. Kalb, X.-Z. Liu, H. Berger, R. W. Carpick, and J. Hone, "Frictional characteristics of atomically thin sheets," *Science* **328**, 76–80 (2010).

[11] J. D. Caldwell *et al.*, "Photonics with hexagonal boron nitride," *Nature Reviews Materials* **4**, 552–567 (2019).

[12] J. S. Bunch *et al.*, "Electromechanical resonators from graphene sheets," *Science* **315**, 490–493 (2007).

[13] A. Falin *et al.*, "Mechanical properties of atomically thin boron nitride and the role of defects," *Nat. Commun.* **8**, 15815 (2017).

[14] A. Castellanos-Gomez, "Why all the fuss about 2D semiconductors?" *Nature Photonics* **10**, 202–204 (2015).

[15] N. Morell, A. Reserbat-Plantey, I. Tsioutsios, K. G. Schädler, F. Dubin, F. H. L. Koppens, and A. Bachtold, "High-quality-factor mechanical resonators based on WSe_2 monolayers," *Nano Lett.* **16**, 5102–5108 (2016).

[16] I. E. Rosłoń et al., "Probing nanomotion of single bacteria with graphene drums," *Nat. Nanotechnol.* **17**, 637–642 (2022).

[17] D. Thomson et al., "Roadmap on silicon photonics," *J. Opt.* **18**, 073003 (2016).

[18] M. Smit et al., "An introduction to InP-based generic integration technology," *Semicond. Sci. Technol.* **29**, 083001 (2012).

[19] W. J. Westerveld et al., "Sensitive, small, broadband and scalable optomechanical ultrasound sensor in silicon photonics," *Nat. Photon.* **15**, 341–345 (2021).

[20] C. Y. Chao *et al.*, "High-frequency ultrasound sensors using polymer microring resonators," *IEEE Trans. Ultrason. Ferroelectr. Freq. Control* **54**, 957–965 (2007).

[21] Y. Hazan and A. Rosenthal, "Sensitivity enhancement of silicon-photonics-based ultrasound detection with BCB overcladding," in *CLEO: Science and Innovations* (Optical Society of America, 2019), p. SW3L.3.

[22] R. Shnaiderman *et al.*, "A submicrometre silicon-on-insulator resonator for ultrasound detection," *Nature* **585**, 372–378 (2020).

[23] C. Chen, S. Rosenblatt, K. I. Bolotin, W. Kalb, P. Kim, I. Kymissis, H. L. Stormer, T. F. Heinz, and J. Hone, "Performance of monolayer graphene nanomechanical resonators with electrical readout," *Nat. Nanotechnol.* **4**, 861–867 (2009).

[24] P. Weber *et al.*, "Optomechanics with hexagonal boron nitride nanomechanical resonators," *Appl. Phys. Lett.* **104**, 251911 (2014).

[25] J. Lee et al., "High-frequency nanomechanical resonators from two-dimensional hBN," *Nat. Commun.* **9**, 276 (2018).

[26] A. Castellanos-Gomez, M. Poot, G. A. Steele, H. S. J. van der Zant, N. Agraït, and G. Rubio-Bollinger, "Elastic properties of freely suspended MoS_2 nanosheets," *Adv. Mater.* **24**, 772–775 (2012).

[27] A. Frigg, A. Boes, G. Ren, I. Abdo, D.-Y. Choi, S. Gees, and A. Mitchell, "Low loss CMOS-compatible silicon nitride photonics utilizing reactive sputtered thin films," *Opt. Express* **27**, 37795–37805 (2019).

[28] F. Xu et al., "Complex refractive index tunability of graphene at 1550 nm wavelength," *Appl. Phys. Lett.* **106**, 031109 (2015).

[29] S. Y. Lee et al., "Refractive index dispersion of hexagonal boron nitride in the visible and near-infrared," *Phys. Status Solidi B* **256**, 1800417 (2018).

[30] M. Islam et al., "In-plane and out-of-plane optical properties of monolayer, few-layer, and thin-film MoS_2 from 190 to 1700 nm," *Opt. Mater. Express* **11**, 372–387 (2021).

[31] K. Luke et al., "Broadband mid-infrared frequency comb generation in a Si_3N_4 microresonator," *Opt. Lett.* **40**, 4823–4826 (2015).

[32] P. G. Steeneken, R. J. Dolleman, and F. Alijani, "Dynamics of 2D material membranes," *2D Mater.* **8**, 042001 (2021).

[33] W. Wu, L. Wang, Y. Li, F. Zhang, L. Lin, S. Niu, D. Chenet, X. Zhang, Y. Hao, T. F. Heinz, J. Hone, and Z. L. Wang, "Piezoelectricity of single-atomic-layer MoS_2 for energy conversion and piezotronics," *Nature* **514**, 470–474 (2014).

[34] D. Yoon, Y.-W. Son, and H. Cheong, "Negative thermal expansion coefficient of graphene measured by Raman spectroscopy," *Nano Lett.* **11**, 3227–3231 (2011).

[35] W. Paszkowicz et al., "Thermal expansion of hexagonal boron nitride," DESY Annual Report 2000, DESY, Hamburg.

[36] K. F. Mak, M. Y. Sfeir, Y. Wu, C. H. Lui, J. A. Misewich, and T. F. Heinz, "Measurement of the optical conductivity of graphene," *Phys. Rev. Lett.* **101**, 196405 (2008).

[37] S. E. Zhu et al., "Graphene-based bimorph microactuators," *Nano Lett.* **11**, 977–981 (2011).

[38] T. Georgiou et al., "Electrothermal actuation in van der Waals heterostructures," *Appl. Phys. Lett.* **105**, 093109 (2014).

[39] S. Timoshenko, "Analysis of bi-metal thermostats," *J. Opt. Soc. Am.* **11**, 233–255 (1925).

[40] S. Timoshenko and S. Woinowsky-Krieger, *Theory of Plates and Shells*, 2nd ed. (McGraw-Hill, New York, 1959).

[41] Z. Chen et al., "Thermal contact resistance across nanoscale interfaces of graphene/hexagonal boron nitride heterostructures," *Phys. Rev. Applied* **11**, 044069 (2019).

[42] D. Golla, A. Brasington, B. J. LeRoy, and A. Sandhu, "Ultrafast relaxation of hot phonons in graphene-hBN heterostructures," *APL Mater.* **5**, 056101 (2017).

[43] Q. Bao et al., "Atomic-layer graphene as a saturable absorber for ultrafast pulsed lasers," *Adv. Funct. Mater.* **19**, 3077–3083 (2009).

[44] K. F. Mak et al., "Measurement of the optical conductivity of graphene," *Phys. Rev. Lett.* **101**, 196405 (2008).

[45] R. R. Nair *et al.*, "Fine structure constant defines visual transparency of graphene," *Science* **320**, 1308 (2008).

[46] I. F. Crowe et al., "Determination of the quasi-TE mode (in-plane) graphene linear absorption coefficient via integration with silicon-on-insulator racetrack cavity resonators," *Opt. Express* **22**, 18625–18632 (2014).

[47] H. Li *et al.*, "Optical absorption in graphene integrated on silicon waveguides," *Appl. Phys. Lett.* **101**, 111110 (2012).

[48] C.-Y. Chao *et al.*, "Low-noise wideband ultrasound detection using polymer microring resonators," *Appl. Phys. Lett.* **92**, 193509 (2008).

[49] R. A. Barton *et al.*, "Photothermal self-oscillation and laser cooling of graphene optomechanical systems," *Nano Lett.* **12**, 4681–4686 (2012).

[50] R. J. Dolleman *et al.*, "Optomechanics for thermal characterization of suspended graphene," *Phys. Rev. B* **96**, 165421 (2017).

[51] G. Cassabois et al., "Hexagonal boron nitride is an indirect bandgap semiconductor," *Nat. Photon.* **10**, 262–266 (2016).

[52] X.-Q. Zheng *et al.*, "Hexagonal boron nitride nanomechanical resonators with spatially visualized motion," *Microsystems & Nanoengineering* **3**, 17038 (2017).

[53] X. Liu *et al.*, "Progress of optomechanical micro/nano sensors: a review," *Int. J. Optomechatronics* **15**, 120–159 (2021).

[54] H. Sun *et al.*, "Application perspective of cavity optomechanical system," *Frontiers in Quantum Science and Technology* **1**, 1091691 (2023).

[55] C. Lee *et al.*, "Measurement of the Elastic Properties and Intrinsic Strength of Monolayer Graphene," *Science* **321**, 385–388 (2008).

[56] J. Tao, N. Lutsey, C. Y. Wang, J. Hone, R. B. Kaner, and J. M. Deen, "Black phosphorus nanomechanical resonators," *Nano Lett.* **15**, 6835–6840 (2015).

[57] B. Anasori, M. R. Lukatskaya, and Y. Gogotsi, "2D metal carbides and nitrides (MXenes) for energy storage," *Nat. Rev. Mater.* **2**, 16098 (2017).

[58] K. Kinoshita, R. Moriya, M. Onodera, Y. Wakafuji, S. Masubuchi, K. Watanabe, T. Taniguchi, and T. Machida, "Dry release transfer of graphene and few-layer h-BN by utilizing thermoplasticity of polypropylene carbonate," *npj 2D Mater. Appl.* **3**, 22 (2019).

[59] H. Liu, S. Lodha, H. S. J. van der Zant, P. G. Steeneken, and G. J. Verbiest, "Optomechanical method for characterizing thermal transport across van der Waals interfaces," arXiv:2509.04786 [physics.app-ph] (2025).

[60] R. J. Dolleman, D. Davidovikj, S. J. Cartamil-Bueno, H. S. J. van der Zant, and P. G. Steeneken, "Opto-thermally excited multimode parametric resonance in graphene membranes," *2D Mater.* **5**, 045010 (2018).

[61] Y. Liu et al., "Thermal Conductance of the 2D MoS_2/h-BN and graphene/h-BN Interfaces," *Sci. Rep.* **7**, 43886 (2017).

[62] L. Lindsay and D. A. Broido, "Theory of thermal transport in multilayer graphene and graphite," *Phys. Rev. B* **89**, 155421 (2014).

[63] R. J. Dolleman *et al.*, "Transient thermal characterization of suspended graphene membranes," *Phys. Rev. Materials* **2**, 114008 (2018).

[64] S. Trolier-McKinstry and P. Muralt, "Thin film piezoelectrics for MEMS," *J. Electroceram.* **12**, 7–17 (2004).

[65] S. Beeby et al., *MEMS Mechanical Sensors* (Artech House, 2004).

[66] W. Bogaerts, P. De Heyn, T. Van Vaerenbergh, K. De Vos, S. Kumar Selvaraja, T. Claes, P. Dumon, P. Bienstman, D. Van Thourhout, and R. Baets, "Silicon microring resonators," *Laser Photonics Rev.* **6**, 47–73 (2012).

[67] A. Yariv, "Universal relations for coupling of optical power between microresonators and dielectric waveguides," *Electron. Lett.* **36**, 321–322 (2000).

[68] A. Yariv and P. Yeh, *Photonics: Optical Electronics in Modern Communications*, 6th ed. (Oxford University Press, 2006).

[69] Liquid Instruments, *Impedance measurements with Moku:Lab – Part 1: Resistance*, Application Note (13 January 2023). Available at: https://liquidinstruments.com/application-notes/impedance-measurements-a-guide-to-measuring-impedance-with-mokulabs-frequency-response-analyzer-part-1/.

[70] R. K. Pathria and P. D. Beale, *Statistical Mechanics*, 3rd ed. (Elsevier, 2011).

Appendices

Appendix A: Supporting Calculations for Actuation Force Comparison

The effective spring constant k_{eff} of a clamped circular membrane under small central deflection is given by the linearised tension-plus-bending model:

$$k_{\text{eff}} = 4\pi\sigma_0 h + \frac{16\pi E h^3}{3r^2(1-\nu^2)} \tag{A.1}$$

where σ_0 is the residual tensile stress, h is the membrane thickness, E is Young's modulus, r is the membrane radius ($10\,\mu$m), and ν is Poisson's ratio. The first term dominates for pretensioned 2D materials (graphene, hBN, MoS_2); the second term becomes significant for thicker or stiffer reference membranes such as Si_3N_4.

All material parameters are taken from Table 2.1 and the literature values cited in Section 2.2. The static displacement is then obtained in the small-signal limit as

$$\delta = \frac{F_{\text{es}}}{k_{\text{eff}}} \tag{A.2}$$

Appendix B: Thermal Low-Pass Filtering: DC versus AC Temperature Response

When the actuation laser (Laser 2) is intensity-modulated at a frequency f, the optical power absorbed in the graphene patch can be written as

$$P_{\mathrm{abs}}(t) = P_{\mathrm{DC}}\big(1 + m\cos(2\pi f t)\big), \tag{B.3}$$

where P_{DC} is the time-averaged absorbed power and m is the modulation index ($0 < m \leq 1$).

Only the time-varying (AC) part of the absorbed power can generate a periodic temperature oscillation and therefore a coherent (phase-locked) thermal moment that drives the membrane at frequency f. The steady (DC) heating only produces a static temperature offset.

The temperature dynamics of the graphene/hBN patch are described by the lumped thermal energy balance

$$C\frac{dT}{dt} + G_{\mathrm{eff}}(T - T_0) = P_{\mathrm{abs}}(t), \tag{B.4}$$

where $T(t)$ is the instantaneous temperature of the graphene patch, T_0 is the constant ambient temperature of the surroundings (substrate and air), C is the heat capacity of the patch, and G_{eff} is the effective thermal conductance from the patch to its surroundings.

It is convenient to define the **excess temperature**

$$\theta(t) = T(t) - T_0, \tag{B.5}$$

which represents the temperature rise of the patch above ambient. Substituting this definition yields the simpler form

$$C\frac{d\theta}{dt} + G_{\mathrm{eff}}\theta = P_{\mathrm{abs}}(t), \tag{B.6}$$

or equivalently

$$\tau\frac{d\theta}{dt} + \theta = \frac{P_{\mathrm{abs}}(t)}{G_{\mathrm{eff}}}, \tag{B.7}$$

where we have introduced the **thermal time constant**

$$\tau = \frac{C}{G_{\mathrm{eff}}}. \tag{B.8}$$

Because the driving term $P_{\mathrm{abs}}(t)$ consists of a constant part and a sinusoidal part, we can solve the DC and AC problems separately (the system is linear).

DC solution (steady state) When all quantities are constant, $d\theta/dt = 0$, and we obtain the steady-state temperature rise

$$\Delta T_{\mathrm{DC}} = \frac{P_{\mathrm{DC}}}{G_{\mathrm{eff}}}. \tag{B.9}$$

AC solution (oscillating part) We look for a solution of the form

$$\theta_{\mathrm{AC}}(t) = \mathrm{Re}\Big[\tilde{\theta}\, e^{j2\pi f t}\Big], \tag{B.10}$$

where $\tilde{\theta}$ is a complex amplitude. Substituting into the differential equation and using the complex representation of the cosine gives

$$\tau(j2\pi f)\tilde{\theta} + \tilde{\theta} = \frac{mP_{\mathrm{DC}}}{G_{\mathrm{eff}}}. \tag{B.11}$$

Solving for the complex amplitude yields

$$\tilde{\theta} = \frac{mP_{\mathrm{DC}}/G_{\mathrm{eff}}}{1 + j2\pi f\tau}. \tag{B.12}$$

The physical (real) amplitude of the temperature oscillation is the modulus of this complex number:

$$\Delta T_{\mathrm{AC}}(f) = |\tilde{\theta}| = \frac{m\,P_{\mathrm{DC}}/G_{\mathrm{eff}}}{\sqrt{1 + (2\pi f\tau)^2}} = m \cdot \Delta T_{\mathrm{DC}} \times \frac{1}{\sqrt{1 + (2\pi f\tau)^2}}. \tag{B.13}$$

In the high-frequency limit that applies to our experiment ($f \gg 1/\tau$), we have $2\pi f\tau \gg 1$. The "1" under the square root can be neglected and the expression simplifies to the compact approximation

$$\Delta T_{\mathrm{AC}}(f) \approx \frac{m \cdot \Delta T_{\mathrm{DC}}}{2\pi f\tau} \qquad \text{or} \qquad \text{Attenuation} \approx \frac{1}{2\pi f\tau}. \tag{B.14}$$

For the device parameters relevant to this work ($\tau \approx 0.8$–$3\,\mu$s) the thermal cutoff frequency $1/\tau$ lies between approximately 0.33 MHz and 1.25 MHz. At the mechanical resonance frequencies used in the measurements ($f = 12$–20 MHz) the ratio $f/(1/\tau)$ is between 10 and 60. The high-frequency approximation is therefore extremely well satisfied, and the AC temperature oscillation is attenuated to only **0.3 % − 4 %** of the DC value.

Appendix C: Experimental Methodology

C.1 Photographic Documentation of Device Fabrication and Heterostructure Transfer

This annex provides photographic documentation of the custom apparatus and key steps used in the sequential dry-transfer process of mechanically exfoliated hBN and graphene flakes onto silicon photonic chips, as described in Section 6.1.

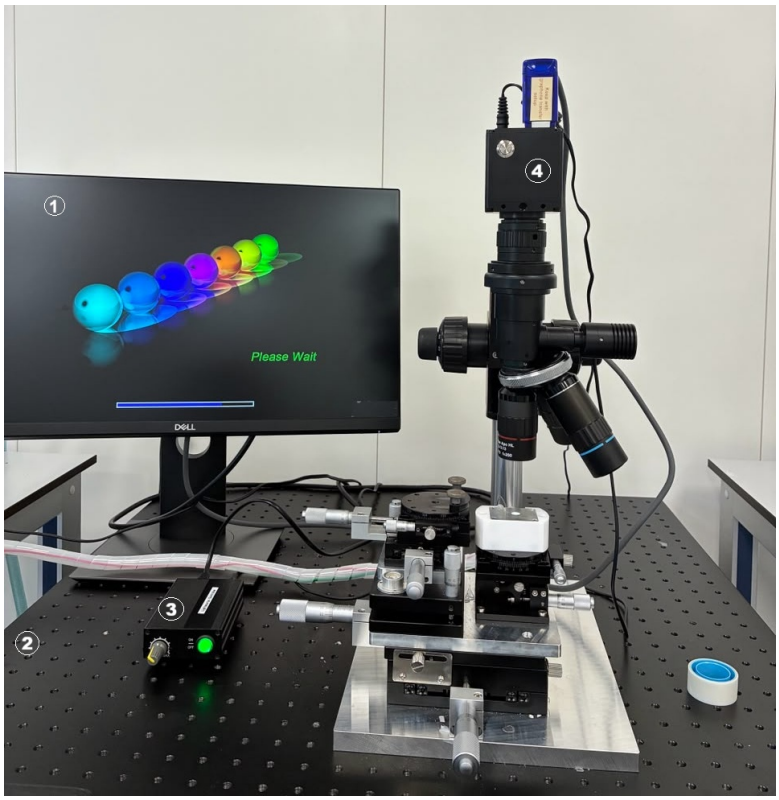


Figure 1: Overview of the custom microscope-based transfer station used for sequential dry transfer of hBN and graphene flakes. The setup consists of a high-resolution optical microscope with manual micromanipulator stages, a dome-shaped PDMS stamp holder, and a temperature-controlled sample stage. (1) Real-time monitor displaying the microscope view, (2) optical breadboard, (3) Microscope LED light source controller, (4) microscope head with integrated camera and illumination. The station enables precise manual alignment and placement of 2D material flakes onto target locations on pre-fabricated photonic chips containing strip ring resonators.

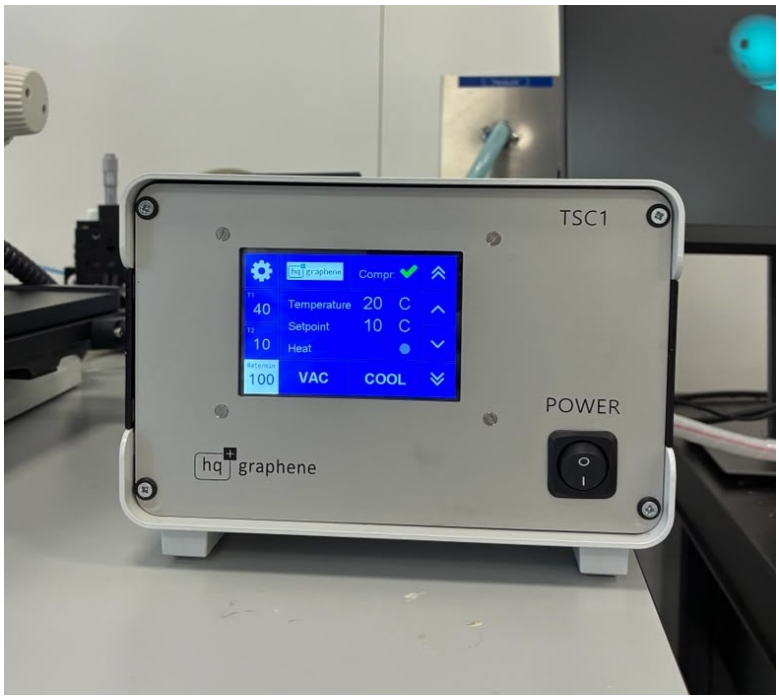
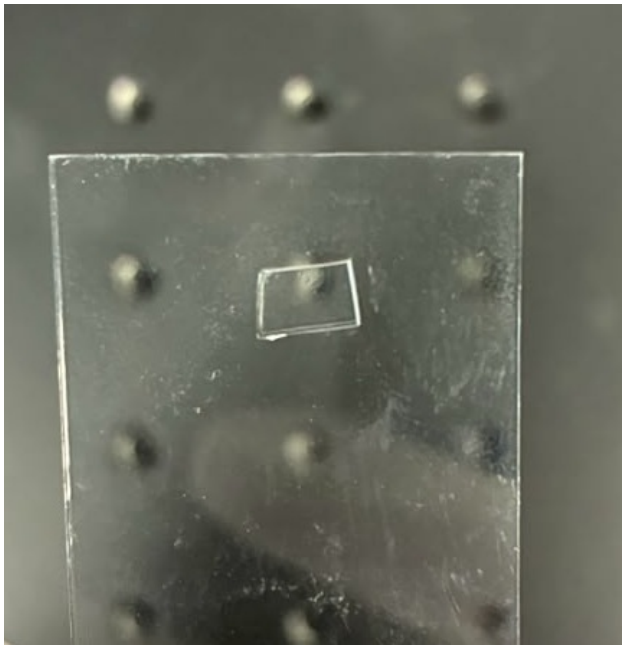


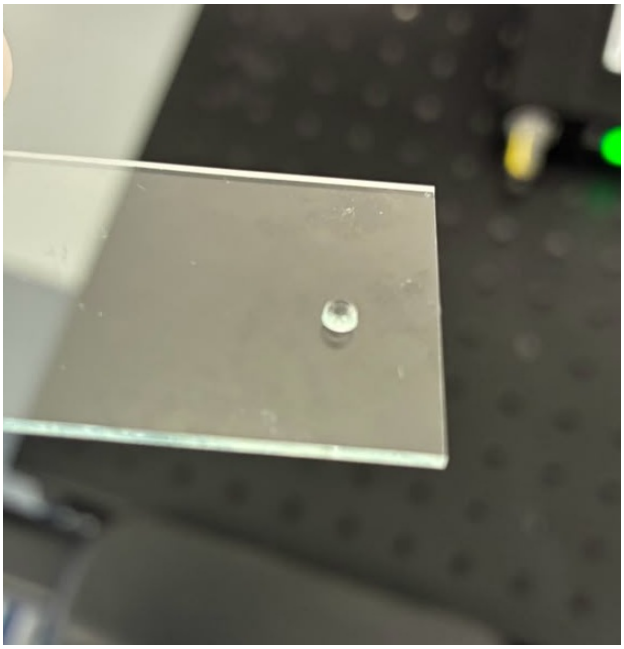
Figure 2: HQ Graphene TSC1 integrated temperature and vacuum controller. This compact touchscreen unit controls both the temperature of the sample stage (heating and active cooling) and the vacuum chuck. Pressing the VAC button activates the vacuum through a small hole in the stage, firmly holding the photonic chip or glass slide in place and preventing movement during the manual alignment and transfer of hBN and graphene flakes. The controller was used to heat the chip to approximately 70 °C during the contact step to improve adhesion and transfer yield.



Figure 3: Mechanically exfoliated Graphene flakes on commercial adhesive tape after the initial exfoliation step. Dark regions correspond to Graphene flakes of varying thickness.



(a) Top view of the square PDMS stamp on a glass slide.



(b) Top view of the dome-shaped PDMS stamp on a glass slide.

Figure 4: PDMS stamps used for the dry-transfer process of hBN and graphene flakes (see Section 6.1). (a) Square PDMS stamp used for initial flake pick-up. (b) Dome-shaped PDMS stamp used for precise transfer onto the photonic chip.

Appendix D: Detailed Photographs and Specifications of the Experimental Optical Setup

The optothermal actuation and cavity-enhanced photonic readout experiments were carried out on the dedicated bench shown in the figures below. Full procedural details, measurement protocols, and parameter variation strategies are given in Chapter 6. The setup enables precise locking of a narrow-linewidth 1550 nm probe laser to the ring-resonator flank while recording the intensity modulation induced by out-of-plane motion of the hybrid graphene/hBN membrane.

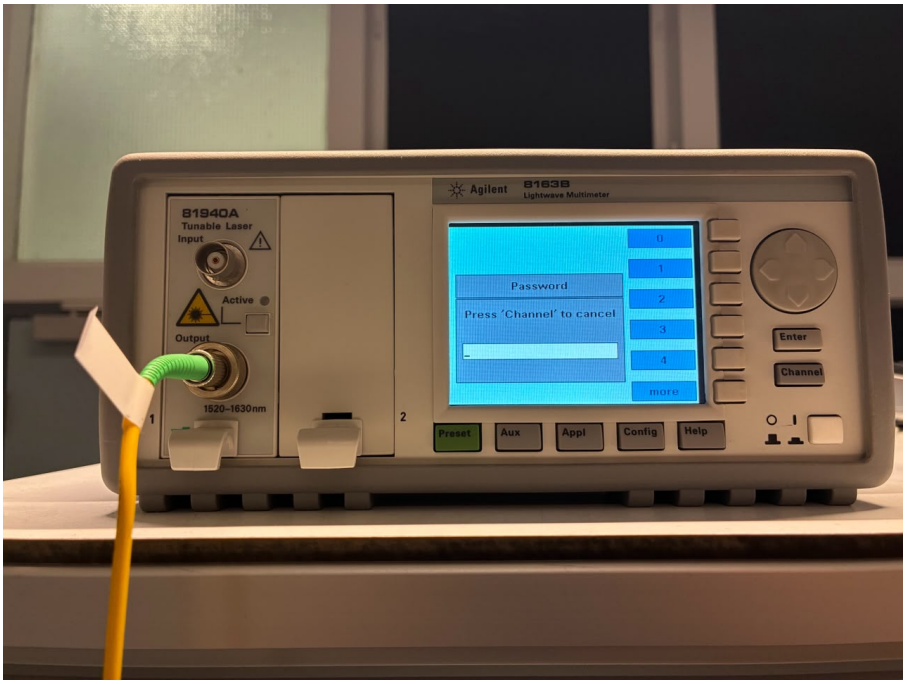


Figure 5: Agilent 8163B Lightwave Multimeter mainframe equipped with 81940A tunable laser module (1520–1630 nm). This instrument supplies the narrow-linewidth, wavelength-tunable probe light used for cavity-enhanced readout of membrane displacement via the strip waveguide ring resonator.

The modular architecture shown above guarantees full compatibility with the electrode-free, contact-free optothermal actuation scheme while delivering the high displacement sensitivity required to resolve picometre- to nanometre-scale motion of the ultrathin hBN membranes.

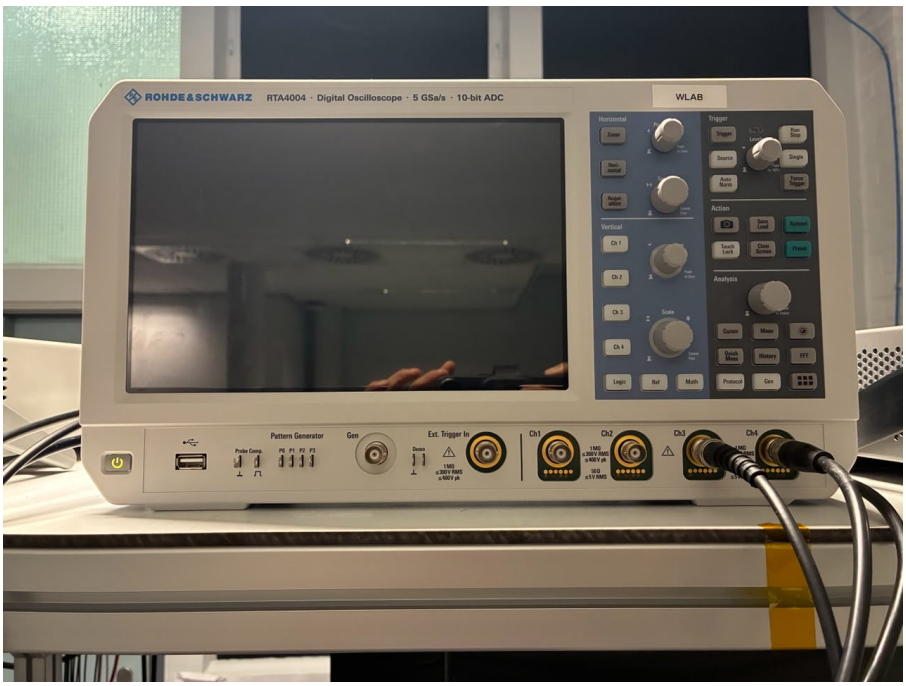


Figure 6: Rohde & Schwarz RTA4004 digital oscilloscope (5 GSa/s, 10-bit ADC) used for time-domain acquisition and real-time FFT analysis of the balanced-photodetector output, enabling extraction of mechanical resonance frequencies and quality factors.



Figure 7: Thorlabs handheld optical power meter (PM100D series) employed for launched-power calibration and real-time monitoring during fibre-to-chip or free-space alignment.

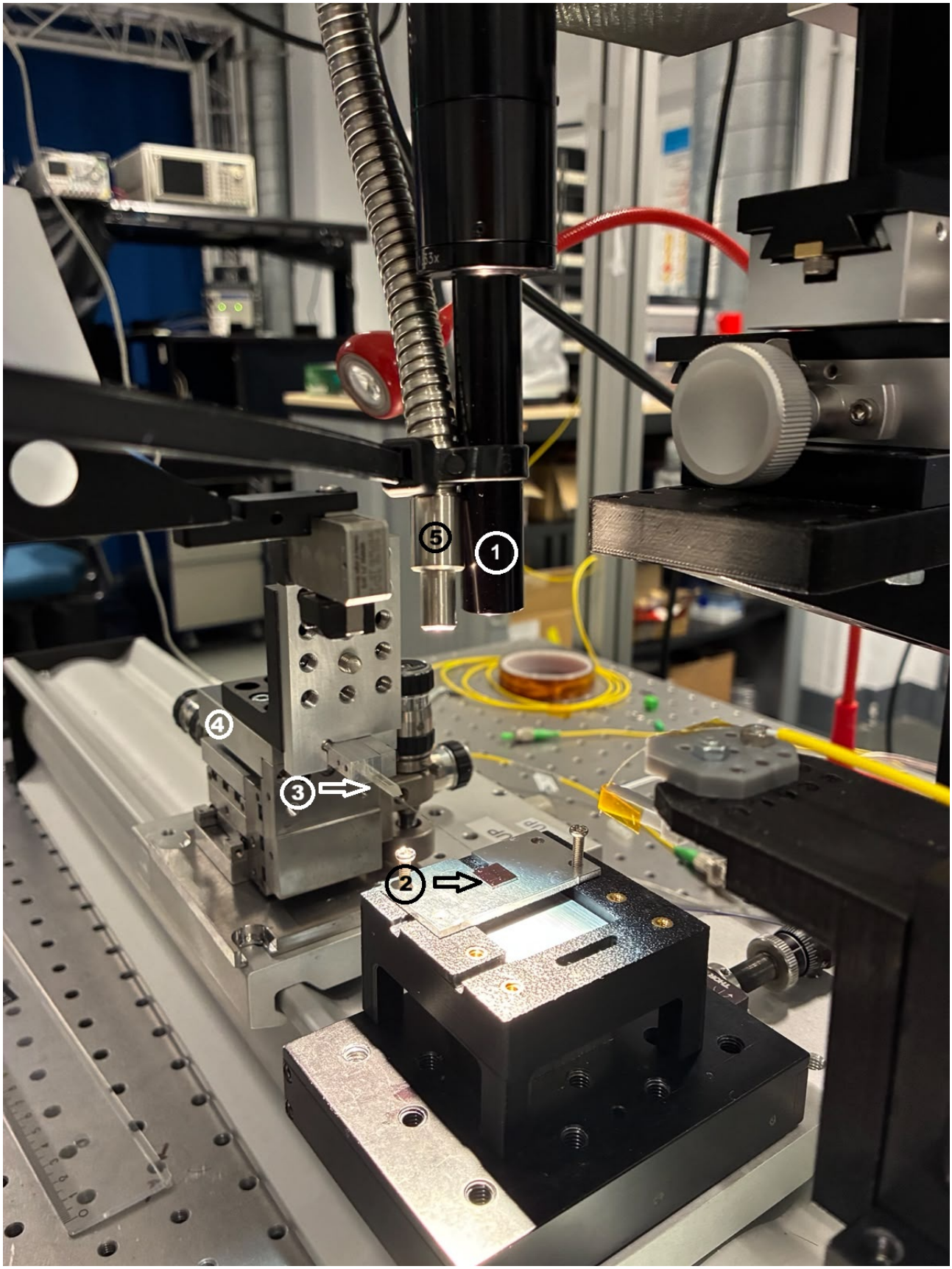


Figure 8: Detailed view of the optomechanical characterisation station on the vibration-isolated optical table. (1) Long-working-distance microscope objective used for real-time imaging and precise alignment of the photonic chip. (2) Silicon photonic chip containing the suspended hybrid graphene/hBN membrane, mounted on a custom holder. (3) Fibre-to-chip coupling fixture and input waveguide alignment mount. (4) Multi-axis manual translation stage assembly for lateral and vertical positioning of the fiber array fixture. (5) light illumination for visualization.

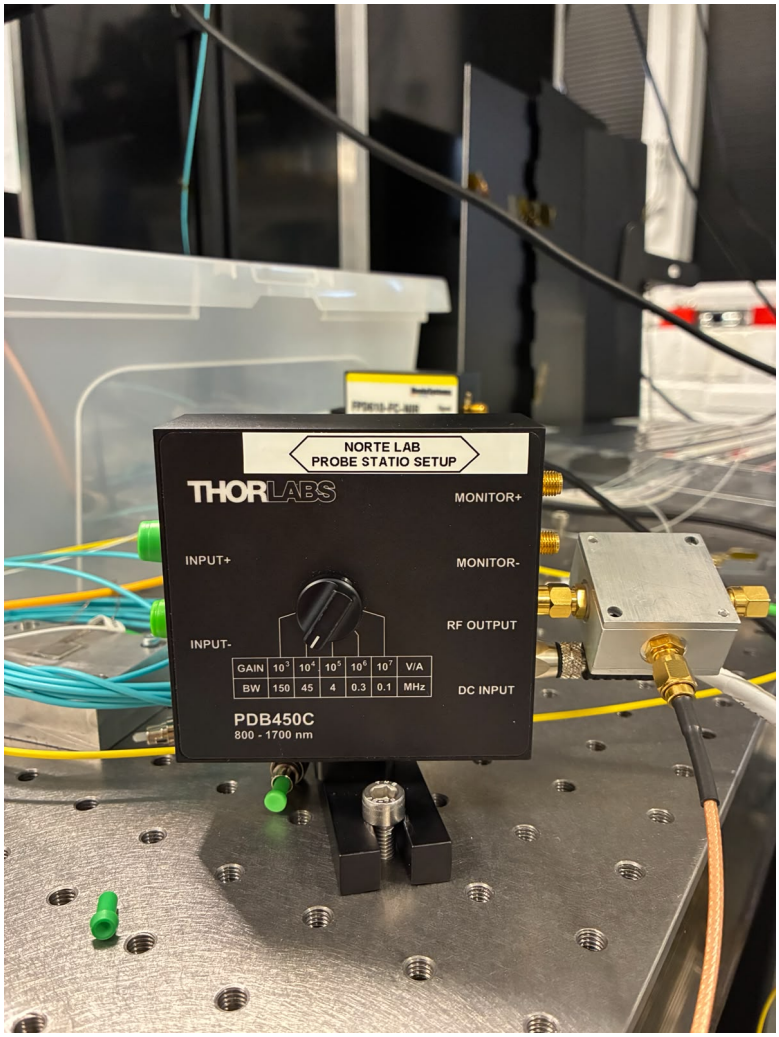


Figure 9: Thorlabs PDB450C balanced photodetector (800–1700 nm) with selectable transimpedance gain. The detector provides high-sensitivity, common-mode-rejected detection of the optomechanically modulated optical signal from the on-chip photonic circuit.

Appendix E: Numerical evaluation of $\int S_{VV}(f)\,\mathrm{d}f$

This appendix documents the conversion of the raw spectrum-analyser traces into the integrated voltage spectral density that appears in the equipartition calibration of Sec.7.3. The procedure is identical for the three frequencies 12 MHz, 13 MHz and 14 MHz; explicit arithmetic is shown for representative points from each data file obtained during the modulation measurement.

Common conversion steps

Every raw data point is reported by the Moku:Lab as a power level in dBm. The linear power in watts is obtained from

$$P = 10^{(\mathrm{dBm}/10)} \times 10^{-3}.$$

Division by the resolution bandwidth RBW = 43.23 kHz yields the power spectral density

$$S_{PP}(f) = \frac{P}{\mathrm{RBW}} \qquad (\mathrm{W\,Hz^{-1}}).$$

Multiplication by the analyser input impedance $R = 50\,\Omega$ converts this quantity into the voltage spectral density

$$S_{VV}(f) = S_{PP}(f) \times R \qquad (\mathrm{V^2\,Hz^{-1}}).$$

The electronic noise floor is estimated as the median of $S_{VV}(f)$ in the quiet interval 20–22 MHz (a region free of both the fundamental mechanical peak and the higher-frequency structure visible above 30 MHz). The thermomechanical spectral density is then defined by point-wise subtraction of this constant floor:

$$S_{VV}^{\mathrm{mech}}(f) = \max\bigl(S_{VV}(f) - S_{VV}^{\mathrm{floor}},\, 0\bigr). \tag{E.15}$$

Any residual negative values that arise from statistical fluctuations about the floor are set to zero so that they do not contribute a negative area.

Additional processing choices

- The coherent drive spike is excluded by masking a ±100 kHz window centred on the nominal drive frequency. This prevents the deterministic tone from contaminating the Brownian integral.
- The numerical integral is evaluated only over the interval 8–18 MHz. This window fully contains the fundamental thermomechanical peak while excluding the elevated continuum that appears at higher frequencies.
- The frequency-bin width of the acquired spectra is $\Delta f \approx 30.5$ kHz. The integral is therefore realised as the discrete sum

$$\int_{8\,\mathrm{MHz}}^{18\,\mathrm{MHz}} S_{VV}^{\mathrm{mech}}(f)\,\mathrm{d}f \;\approx\; \sum_i S_{VV}^{\mathrm{mech}}(f_i)\,\Delta f. \tag{E.16}$$

12 MHz data set

Electronic floor (median 20–22 MHz):

$$S_{VV}^{\mathrm{floor}} = 6.31 \times 10^{-14}\,\mathrm{V^2\,Hz^{-1}}.$$

Example continuum point near the drive frequency (11.99 MHz, outside the excluded spike core), raw value −70.40 dBm:

$$\begin{aligned} P &= 10^{(-70.40)/10} \times 10^{-3} = 9.120 \times 10^{-11}\,\mathrm{W}, \\ S_{VV} &= \frac{9.120 \times 10^{-11}}{4.323 \times 10^{4}} \times 50 = 1.055 \times 10^{-13}\,\mathrm{V^2\,Hz^{-1}}, \\ S_{VV}^{\mathrm{mech}} &= 1.055 \times 10^{-13} - 6.31 \times 10^{-14} = 4.24 \times 10^{-14}\,\mathrm{V^2\,Hz^{-1}}. \end{aligned}$$

After processing the entire spectrum according to Eq. (E.15) and the choices listed above,

$$\int_{8\,\mathrm{MHz}}^{18\,\mathrm{MHz}} S_{VV}^{\mathrm{mech}}(f)\,\mathrm{d}f = 2.99 \times 10^{-7}\,\mathrm{V^2}.$$

13 MHz data set

Electronic floor (median 20–22 MHz):

$$S_{VV}^{\mathrm{floor}} = 5.99 \times 10^{-14}\,\mathrm{V^2\,Hz^{-1}}.$$

Example continuum point near the drive frequency (12.80 MHz, outside the excluded spike core), raw value -69.10 dBm:

$$\begin{aligned} P &= 10^{(-69.10)/10} \times 10^{-3} = 1.230 \times 10^{-10}\,\mathrm{W}, \\ S_{VV} &= \frac{1.230 \times 10^{-10}}{4.323 \times 10^{4}} \times 50 = 1.423 \times 10^{-13}\,\mathrm{V^2\,Hz^{-1}}, \\ S_{VV}^{\mathrm{mech}} &= 1.423 \times 10^{-13} - 5.99 \times 10^{-14} = 8.24 \times 10^{-14}\,\mathrm{V^2\,Hz^{-1}}. \end{aligned}$$

After processing the entire spectrum,

$$\int_{8\,\mathrm{MHz}}^{18\,\mathrm{MHz}} S_{VV}^{\mathrm{mech}}(f)\,\mathrm{d}f = 1.82 \times 10^{-7}\,\mathrm{V^2}.$$

14 MHz data set

Electronic floor (median 20–22 MHz):

$$S_{VV}^{\mathrm{floor}} = 6.17 \times 10^{-14}\,\mathrm{V^2\,Hz^{-1}}.$$

Example continuum point near the drive frequency (13.50 MHz, outside the excluded spike core), raw value -68.67 dBm:

$$\begin{aligned} P &= 10^{(-68.67)/10} \times 10^{-3} = 1.358 \times 10^{-10}\,\mathrm{W}, \\ S_{VV} &= \frac{1.358 \times 10^{-10}}{4.323 \times 10^{4}} \times 50 = 1.571 \times 10^{-13}\,\mathrm{V^2\,Hz^{-1}}, \\ S_{VV}^{\mathrm{mech}} &= 1.571 \times 10^{-13} - 6.17 \times 10^{-14} = 9.54 \times 10^{-14}\,\mathrm{V^2\,Hz^{-1}}. \end{aligned}$$

After processing the entire spectrum,

$$\int_{8\,\mathrm{MHz}}^{18\,\mathrm{MHz}} S_{VV}^{\mathrm{mech}}(f)\,\mathrm{d}f = 2.40 \times 10^{-7}\,\mathrm{V^2}.$$

Summary of the integrals

Drive frequency (MHz)	$\displaystyle\int_{8\,\mathrm{MHz}}^{18\,\mathrm{MHz}} S_{VV}^{\mathrm{mech}}(f)\,\mathrm{d}f$ (V^2)
12	2.99×10^{-7}
13	1.82×10^{-7}
14	2.40×10^{-7}

These three values constitute the left-hand side of the equipartition calibration equation used in the main text.